Continuous Damage Monitoring of CFRP using Fiber Bragg Grating:
In Stitched Laminate Material and Thin Composite Structure with Stiffness Mismatch

（FBG センサーを用いた CFRP のその場損傷検知：縫合複合材と剛性の不整合を有する薄板積層材）

By
Agus Trilaksono
10991571

Submitted to the System Design Faculty in Partial Fulfillment of the Requirements for the Degree of

DOCTORATE OF PHILOSOPHY IN
AEROSPACE ENGINEERING DEPARTMENT AT
THE TOKYO METROPOLITAN UNIVERSITY

Accepted by Supervisor

Professor Naoyuki Watanabe
Aerospace Engineering Department, System Design Faculty
Tokyo Metropolitan University

Ph.D thesis committee:

Professor Naoyuki Watanabe (Chairman)	Tokyo Metropolitan University
Professor Fukuchi Hajime	Tokyo Metropolitan University
Professor Kitazono Koichi	Tokyo Metropolitan University
Professor Kobayashi Satoshi	Tokyo Metropolitan University

The essence of strategy is choosing to perform activities differently than rivals do. - Dr. Michael Porter (1947 -), American Author and Professor

ABSTRACT

This thesis provides a comprehensive understanding of the capability of optical fiber sensor systems, namely fiber Bragg grating sensor (hereafter, 'FBG sensor'), to monitor damage behavior in composite materials and structures under mechanical loading. The FBG sensor is embedded in two types of composite systems: (i) stitched laminate materials, (ii) thin composite structure with stiffness mismatch. The composite systems are subjected to two load cases, i.e. static tension and three-point-bending. The stitched laminate materials, which have through-thickness reinforcement in the form of stitch threads, exhibit a complex failure mechanism. Thin composite structures with stiffness mismatch exhibit secondary bending moment due to the shift of neutral-axis. This neutral-axis shift eventually causes delamination, which is generated by high peel stresses at the edge of a stiffener.

Cohesive zone model and classical lamination theory combined with first ply failure criteria are performed to determine the preferred area for FBG sensor installation before manufacturing. Experiments were conducted to determine load distribution and failure mode within the specimen. Some non-destructive inspection, such as acoustic emission test and ultrasonic C-scan inspection, are conducted. Micro-structure microscopy is performed to observe the damage in detail. And during the static test,

FBG sensor was lit using a broadband light source then the spectrum behavior will retrieve until specimen broken.

In this research, a close understanding between the mechanical behavior as finite element analysis result and experimental results are obtained. FBG sensor has successfully detected, monitored and characterized some kinds of damage caused by both loading cases. Multi-peak occurrence is used to interpret the damage growth when specimen experienced with non-linear strain, while is experienced linear strain then wavelength broader is used. FBG sensor combined with C-scan inspection can predict the damage growth. A spectrum graph of the FBG sensor results can be used to replace a stress-strain mechanical graph for use in composite structural health monitoring. However, the additional riveting process can potentially introduce delamination near the holes in post manufacturing. It can be seen that the original spectrum changes. Finally, recommendation on how to establish the structural health monitoring is given. This thesis has proven that FBG sensor is an effective tool to detect damage in composite materials and structures. FBG sensor has a great potential to change the conceptual design and the maintenance process of the aircraft.

Keywords: Carbon fiber, Cohesive elements, Secondary bending moment, Stitched Laminate, Structural Health Monitoring.

ACKNOWLEGEMENTS

There are many people I would like to recognize for their help and support with my research. Without them, I would not have been able to accomplish this milestone so quickly with such satisfying results. I would like to thank my supervisor Professor Naoyuki Watanabe; he has always believed in my abilities and provided whatever advice and resources necessary for me to accomplish my goals. The rest of my thesis committee; Professor Fukuchi Hajime, Professor Kitazono Koichi and Professor Kobayashi Satoshi each spent countless hours with me to discuss aspects of my research. While not officially a member of my thesis committee. Dr. Atsushi Kondo provided as much support as anyone else during the past few years, and added much more meaning to my work and working revisions of my various publications. A special thanks goes to Dr. Ayumu Inasawa and Dr. Morooka Satoshi who made my jobs more easily. Dr. Shin-ichi Takeda dan Dr. Hikaru Hoshi for his kindness to teach how to operate SHM and mechanical equipment and let me used JAXA facility.

Next, I would like to acknowledge everyone who provided technical support for this project. Thanks to Dr.Tan and Dr.Arief for their friendship and share their knowledge especially introducing several test equipment in our laboratory.

Many Indonesian fellows contributed to this work by helping and providing

support me with wonderful advice, inspiration and friendship over the years. A special thanks goes to all of my lab members.

Lastly, I need to thank to all my loving family and Indonesian Aerospace members who have always given me their support. I love you all

TABLE OF CONTENTS

ABSTRACT ……3

ACKNOWLEGEMENTS 5

TABLE OF CONTENTS 7

LIST OF FIGURES 12

NOMENCLATURE 23

CHAPTER 1 : INTRODUCTION 26

1.1. BACKGROUND 26

1.1.1. Composite materials in aircraft and the structural issues. 26

1.1.2. Structural health monitoring (SHM) for composite. 30

1.1.3. SHM in composite using fiber Bragg grating (FBG) sensors. 35

1.1.4. Principle and capability of FBG sensor to detect damage in composite. 40

1.2. PREVIOUS RESEARCH. 45

1.3. RESEARCH OBJECTIVES 47

1.4. RESEARCH METHODOLOGY 49

1.5. LAYOUT OF THESIS 53

CHAPTER 2 : DAMAGE DETECTION AND MONITORING OF THIN COMPOSITE STRUCTURE. 56

2.1. OVERVIEW 56

2.2. GENERAL DESIGN CONCEPT 57

2.3. NUMERICAL ANALYSIS 61

2.3.1. Specimen Configuration. 61

2.3.2. Methodology 62

2.3.2.1. FEM Analysis Parameter 62

2.3.2.2. Cohesive Zone Model Laws 63

2.3.3. Three-dimensions and Elements Modelling 67

2.3.4. Numerical Result 73

2.4. SPECIMEN FABRICATION. 91

2.4.1. Pre-impregnated Lay-up Preparation 91

2.4.2. Bonding Process and FBG Sensor Installation 93

2.4.3. Drilling Process 95

2.4.4. Strain Gauge Installation 97

2.5. EXPERIMENTAL PROCEDURE. 98

2.5.1. Tensile test 100

2.5.2. Three-point loading test 102

2.5.3. Bondable strain gauge test 103

2.5.4. Ultrasonic C-scan test 105

2.5.5. Fiber Bragg grating sensor test 108

2.6. RESULTS AND DISCUSSION 108

2.6.1. Experimental verification of numerical analysis. 108

2.6.1.1. Bonded joint model 109

2.6.1.2. Combined joint model 112

2.6.1.3. Ultrasonic C-scan result 115

2.6.2. The perspective of FBG sensor reading 118

2.6.2.1. Post-manufacturing spectrum 118

2.6.2.2. Power spectrum characteristic under tension loading 120

2.6.2.3. Power spectrum characteristic under three-point loading 129

2.6.2.4. Power spectrum characteristic under loading-unloading test 133

2.6.3. Damage quantification. 140

2.7. CONCLUSIONS 143

CHAPTER 3 : DAMAGE DETECTION AND MONITORING OF STITCHED LAMINATE MATERIAL. 146

3.1. OVERVIEW 146

3.2. A STITCHED LAMINATE CONCEPT WITH FBG SENSOR INSTALLED IN. 147

3.3. NUMERICAL ANALYSIS 148

3.3.1. Geometry and Configuration. 148

3.3.2. Methodology 149

3.3.2.1. FEM Analysis Parameter 149

3.3.2.2. Stitching threads modelling approach 152

3.3.3. Laminate Mechanical Response 154

3.3.4. Three dimensional and Elements Modelling 156

3.3.5. Numerical Result 156

3.4. MATERIAL AND SPECIMEN PREPARATION 159

3.4.1. Fabric Preform and VaRTM Preparation 159

3.4.2. FBG Sensor Installation 160

3.5. TESTING AND DAMAGE EVALUATION PROCEDURE 162

3.5.1. Tensile test 162

3.5.2. Ultrasonic C-scan test 164

3.5.3. Acoustic emission test. *165*

3.5.4. Fiber Bragg grating sensor test *166*

3.6. RESULTS AND DISCUSSION 167

3.6.1. Experimental Results. *167*

3.6.1.1. Stitched laminate material. 167

3.6.1.2. Acoustic emission result 168

3.6.1.3. Ultrasonic C-scan result. 171

3.6.2. The perspective of FBG sensor reading *173*

3.6.2.1. Power spectrum characteristic under tension loading. 174

3.6.2.2. Power spectrum characteristic under loading-unloading test 179

3.6.3. Damage quantification. *180*

3.7. CONCLUSIONS 187

CHAPTER 4: CONCLUSIONS. 188

4.1. CONCLUSIONS 188

4.2. RECOMMENDATIONS 191

REFERENCES 193

PUBLICATION LIST 201

LIST OF FIGURES

Figure 1 : Composite application in commercial transport aircraft. 26

Figure 2 : Delamination Onset Causes. 28

Figure 3 : Fiber Bragg grating optics and illustration of the principle. 37

Figure 4 : The principle of power reflection of FBG as strain sensor; (a) No strain, (b) Under tensile strain. 37

Figure 5 : Calculated power reflection. 39

Figure 6 : Construction of FBG sensor. 41

Figure 7 : Design evolution charts before FBG sensor installation. 52

Figure 8 : Specimen for fundamental testing (composite structure with stiffness mismatch) inspired by a skin stringer structure. 58

Figure 9 : The secondary bending phenomena illustration in the composite structure with stiffness mismatch. 60

Figure 10 : Specimen dimensions and configuration with FBG sensor installed inside. 62

Figure 11 : Onset of delamination based on the cohesive zone model theory. 66

Figure 12 : Delamination onset based on Cohesive zone model theory. 67

Figure 13 : Three-dimensional solid modelling. 68

Figure 14 : (a) Conventional shell-to-continuum shell element and (b) continuum

shell-to-conventional solid element. 68

Figure 15 : 3D Element Modelling. 70

Figure 16 : Interaction between parts with tie constraints on the meshes. 71

Figure 17 : Interaction between parts with the merged nodes in the meshes. 71

Figure 18 : Composite lay-up to generate the model section. 72

Figure 19 : Composite shell to generate the model section. 73

Figure 20 : Separation element locations under loading of the bonded joint. 74

Figure 21 : Distribution of maximum principle stress vectors for the bonded joint. 74

Figure 22 : Separation element locations under loading for riveted and bonded joint... 75

Figure 23 : Distribution of maximum principle stress vectors for riveted and bonded joint. 76

Figure 24 : Peeling stress comparison in longitudinal (loading) direction. 77

Figure 25 : Peeling stress comparison in transverse direction..... 77

Figure 26 : Comparison of stress concentrations near the rivet hole. 78

Figure 27 : Comparison of the load transferred to the stiffener..... 79

Figure 28 : Onset of delamination based on cohesive zone model theory in a tensile test. 80

Figure 29 : Onset of delamination based on cohesive zone model theory in

three-point-bending test. 80

Figure 30 (a) (b) : Distribution of principle stress maxima and vector directions under tensile loading for combined joint. 83

Figure 31 : Separation element location during tensile loading for combined joint. 83

Figure 32 (a) (b) : Distribution of principle stress maxima and vector direction for combined joint under three-point loading. 84

Figure 33 : Separation element location during three-point-bending loading for combined joint..... 85

Figure 34 : Stress distribution profile in the longitudinal under tensile loading for combined joint..... 86

Figure 35 : Stress distribution profile in the longitudinal direction of the test under three-point-bending loading for combined joint. 87

Figure 36 : Stress distribution profile in the transverse direction of the test under tensile loading for combined joint. 87

Figure 37 : Stress distribution profile in the transverse direction of the test under three-point-bending loading for combined joint. 88

Figure 38 : Normalized load transfer in the rivet area under tensile loading. 89

Figure 39 : Normalized load transfer in the rivet area under three-point-bending loading.

..... 89

Figure 40 : Autoclave system and curing circle process for impregnated laminate. 93

Figure 41 : Top is a good bond-line and bottom is a bad bond line. 94

Figure 42 : Adhesive gun-mixer system and specimen pre-fit. 95

Figure 43 : Drilling process. 96

Figure 44 : (a) Rivet pre-fit preparation, (b) After rivet squeezing. 97

Figure 45 : Rivet assembles equipment and the compressor system for rivet gun. 97

Figure 46 : Figure 47 : Strain gage bondable process for combining joint and bonded join only specimen. 98

Figure 47 : Tensile test setup. 102

Figure 48 : Flexural test setup. 103

Figure 49 : Wheatstone Bridge Circuit. 105

Figure 50 : The ultrasonic system illustration. 106

Figure 51 : Types of ultrasonic transducer used. 107

Figure 52 : Locations of strain gages and measurements of the bonded joint. 110

Figure 53 : Comparison between finite element analysis and experimental data at area1 for the bonded joint. 110

Figure 54 : Comparison between finite element analysis and experimental data at area2

for the bonded joint. 111

Figure 55 : Comparison between finite element analysis and experimental data at area3 for the bonded joint. 111

Figure 56 : Comparison between finite element analysis and experimental data at area4 for the bonded joint only. 112

Figure 57 : Locations of strain gages and measurements of combined joint. 113

Figure 58 : Comparison between finite element analysis and experimental data at area1 for the combined joint. 113

Figure 59 : Comparison between finite element analysis and experimental data at area2 for the combined joint. 114

Figure 60 : Comparison between finite element analysis and experimental data at area3 for the combined joint. 114

Figure 61 : Comparison between finite element analysis and experimental data at area4 for the combined joint. 115

Figure 62 : Tensile loading interrupt tests in bonded joint only. 116

Figure 63 : Tensile loading interrupt tests in combined joint. 117

Figure 64 : Three point bending loading interrupt tests in bonded joint only. 117

Figure 65 : Three point bending loading interrupt tests in combined joint. 118

Figure 66 : The effect of post-manufacturing processes for FBG sensor installation based on the spectrum reflection reading. 120

Figure 67 : Evolution of spectrum from FBG sensor reading in bonded joint only. 122

Figure 68 : Evolution of spectrum from FBG sensor reading in combined joint. 123

Figure 69 : Spectrum pattern explanation under FBG sensor reading in bonded only. 125

Figure 70 : Spectrum pattern explanation underjoint reading in combined join. 125

Figure 71 (a) (b) : The relationship between normalized intensity and normalized wavelength during loading run in bonded join only structure has a mismatch stiffened at the tensile test. 127

Figure 72 (a) (b) : The relationship between normalized intensity and normalized wavelength during a loading run in combined join. 128

Figure 73 (a) (b) : Comparison normalizing power intensity and wavelength for bonded join only and combined join due to resistance to damage under tension loading. *(a) It indicated the damage start to growth. 129

Figure 74 : Spectrum pattern evolution under FBG sensor reading in combined join in three-point loading. 130

Figure 75 (a) (b) : The correlation between normalized intensity and normalized wavelength to during a loading run to combined join at three point bending. .. 130

Figure 76 (a) and (b) : The relationship between normalized intensity and normalized wavelength during a loading run of bonded join only at three point bending test. 132

Figure 77 (a) and (b) : Curve comparison in normalized intensity and wavelength between two specimen models under three point bending test. *(b)It indicated the damage start to grow. 133

Figure 78 : (a). The load - displacement curve of combined join under tensile test and location of load interrupted during test running. (b) Interrupted 1st at Displacement: 1 mm, Load: 10.6 N and Damage area: 2.7%. (c) Interrupted 2nd at Displacement: 1.5 mm, Load: 14.5 N and Damage area: 3.7%. (d) Interrupted 3rd at Displacement: 2.5 mm, Load: 23.50 N and Damage area: 9.3%..... 135

Figure 79 : (a). The load - displacement curve of bonded join only under tensile test and location of load interrupted during test running. (b) Interrupted 1st at Displacement: 2.5 mm, Load: 25 kN and Damage area: 12%. (c) Interrupted 2nd at Displacement: 4.5 mm, Load: 32.5 kN and Damage area: 60%. (d) Interrupted 3rd at Displacement: 7 mm, Load: 25.3 kN and Damage area: 63%..... 136

Figure 80 : (a). The load - displacement curve of combined join under three point bending test and location of load interrupted during test running. (b) Interrupted

1st at Displacement: 6 mm, Load: 81 N and Damage area: 4.6%. (c) Interrupted 2nd at Displacement: 10 mm, Load: 130 N and Damage area: 7.4%. (d) Interrupted 3rd at Displacement: 14 mm, Load: 170 N and Damage area: 12.9%. 138

Figure 81 : (a). Graphic load - displacement of bonded join only under three point bending test and location of load interrupted during test running. (b) Interrupted 1st at Displacement: 6 mm, Load: 82 N and Damage area: 1.8%. (c) Interrupted 2nd at Displacement: 10 mm, Load: 133 N and Damage area: 2.7%. (d) Interrupted 3rd at Displacement: 14 mm, Load: 176 N and Damage area: 4.6%. 139

Figure 82 : Quantification ratio of spectrum intensity due to damage area of bonded join only and combined joint..... 141

Figure 83 : Quantification ratio of wavelength due to the damage area of combined join in three-point bending loading. 142

Figure 84 : Delamination growth: stress concentrations around rivet holes leading to catastrophic failure in cleavage bearing mode. 143

Figure 85 : The schematic processes of the adopted stitching process by Toyota Industries Corporation with FBG sensor embedded into the laminate. 148

Figure 86 : Specimen model configuration for stitched laminate. All dimensions in mm. 149

Figure 87 : Three dimensional modelling of stitching into the laminate by using rebar model. 151

Figure 88 : Boundary condition of the specimen. 151

Figure 89 : Typical rebar layer in a 20-node isoparametric element. (a) Geometry in the host element, (b) Geometry in the isoparametric domain. 153

Figure 90 : Three-dimensional and elements modelling of stitched laminated material. 156

Figure 91 : Off-axis stress distribution within laminate. 157

Figure 92 : Stress distribution within stitched region. 158

Figure 93 : VaRTM sketch. 160

Figure 94 : FBG placement within stitched laminate material. (a) First ply failure theory result, (b) FBG position illustration within stitching configuration. 161

Figure 95 : The micro-structure photo of FBG sensor installation into the specimen. 162

Figure 96 : Tensile, AE, and Spectrum Analyzer test setups. 163

Figure 97 : Ultrasonic C-scan inspection. 165

Figure 98 : AE graph characteristic. 166

Figure 99 : FBG sensor joining and the losses dB calibration. 167

Figure 100 : Load- strain behavior of stitched laminate material..... 168

Figure 101 : Mechanical behavior versus AE-Hit of stitched laminate material..... 169

Figure 102 : Mechanical behavior versus AE-Energy of stitched laminate material. .. 169

Figure 103 : Mechanical behavior versus AE-Cumulative Energy of stitched laminate material..... 170

Figure 104 : Comparison result between energy and accumulative hit under AE test. 170

Figure 105 : C-scan result specimen2 compared with own original power spectrum.. 172

Figure 106 : C-scan result specimen3 compared with own original power spectrum.. 172

Figure 107 : C-scan result specimen4 compared with own original power spectrum.. 173

Figure 108 : Spectrum shape evolution under FBG sensor reading in stitched laminate. 174

Figure 109 : Spectrum evolution on profiling tensile test. 175

Figure 110 : Highest peak value of the power reflection result in the profiling tensile test compared with the interrupt test..... 176

Figure 111 : Power reflection of the FBG sensor reading compared with the mechanical behavior. 177

Figure 112 : Power reflection of the FBG sensor reading compared with AE test:

accumulative hit characteristic and mechanical behavior. 178

Figure 113 : Power reflection of the FBG sensor reading compared with AE: energy characteristic and mechanical behavior..... 178

Figure 114 : Spectrum evolution in the interrupt load test. 179

Figure 115 : Spectrum evolution in the unloading data..... 180

Figure 116 : (a) Interrupt test1, 20kN..... 182

Figure 117 : (a) and (b) Damage quantification based on the FBG sensor reading and mechanical behavior..... 186

Figure 118 : Damage quantification based on the FBG sensor reading and AE characteristic. 186

NOMENCLATURE

G_{xz}	[GPa]	Out-of-plane Shear Modulus
K	[Nmm*^{1}]	Stress Intensity Factor
K_F	[Nmm^{J}]	Penalty Stiffness of Cohesive Element
Ks	[MPa]	Stiffness of Spring Element
R_y	[m]	Radius of Stitch Yarn
S_{area}	[mm^{1}]	Stitch Thread Cross Sectional Area
S_p	[mm]	Stitching Pitch
S_s	[mm]	Stitching Space
σ_{t1}	[MPa]	Tensile Strength Allowable
σ_{c1}	[MPa]	Compressive Strength Allowable
τ_{12}	[MPa]	Shear Strength Allowable
E_{t1}	[GPa]	Tensile Modulus Allowable
E_{t2}	[GPa]	Compressive Modulus Allowable
G_{12}	[GPa]	Shear Modulus Allowable
SD	[mm^{-2}]	Stitch Density
t	[mm]	Thickness of Specimen
V_{ft}	[%]	Stitch Fibre Volume Fraction

W_t	[Nmm]	Stitch Fibre Strain Energy
x,y,z	-	With Reference to Global Coordinates x, y, z
X_C	[MPa]	Compressive Strength in Fibre Direction
X_T	[MPa]	Tensile Strength in Fibre Direction
Y_C	[MPa]	Compressive Strength Perpendicular to Fibre Direction
Y_T	[MPa]	Tensile Strength Perpendicular to Fibre Direction
δ	[mm]	Displacement
Δ	[mm]	Displacement Jump
Δa	[mm]	Equivalent Displacement Jump
ν_{ij}	-	Poisson Ratio
ρ	[gm^{-3}]	Density
σ_B	[MPa]	Fibre Breaking Strength
σ_{UTL}	[MPa]	Ultimate Compressive Strength
τ	[MPa]	Traction
A_y	[m^2]	Cross Sectional Area of Yarn
b	[mm]	Width of Specimen
d	[gm^{-1}]	Denier
E	[J]	Absorbed Energy

E_f	[GPa]	Youngs Modulus of Stitch Fiber
E_x	[GPa]	Axial Compressive Modulus
E_{xx}	[GPa]	In-plane Longitudinal Modulus
E_{zz}	[GPa]	In-plane Transverse Modulus
F	[N]	Force
F_f^c	-	Hashin Fibre Compression Failure Criterion
F_f^t	-	Hashin Fibre Tension Failure Criterion
F_m^c	-	Hashin Matrix Compression Failure Criterion
F_m^t	-	Hashin Matrix Tension Failure Criterion
G_{IC}	[Nmm^{-1}]	Critical Mode I Strain Energy Release Rate
G_{IIC}	[Nmm^{-1}]	Critical Mode II Strain Energy Release Rate
G_{IIIC}	[Nmm^{-1}]	Critical Mode III Strain Energy Release Rate

CHAPTER 1 : INTRODUCTION

1.1. Background

1.1.1. Composite materials in aircraft and the structural issues.

Composite materials have been used in the aerospace industry over the past three decades for their stiffness-to-weight benefit. Unfortunately, the progress on composites usage was not so promising, even though the trend in transport aircraft size and flight range has been steadily increasing. Figure 1 shows the evolution composite usage at Airbus in spite of the composite usage expectation was all composite wings before the year 2000, all composite fuselage after the year 2000, and the entire airframe around 2010[1].

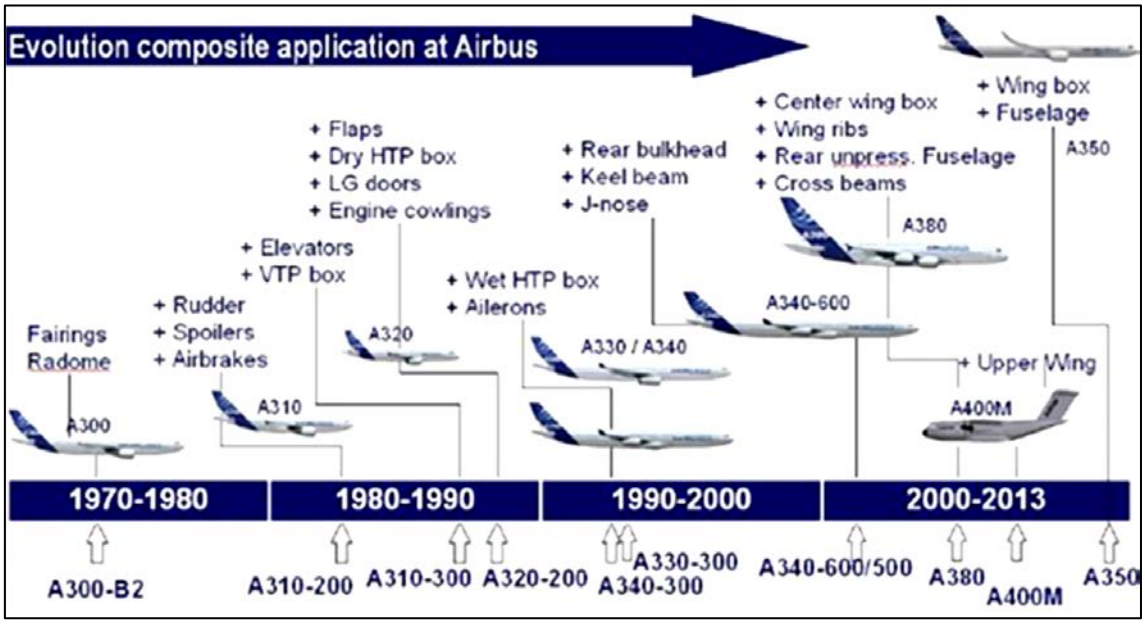

Figure 1 : Composite application in commercial transport aircraft.

There are many factors and issues associated with the insertion of the advanced materials for primary structural applications where structural integrity is the most important factor. Especially for composites, one of the primary concerns is whether or not the material is reliable and durable for the primary structural application. Composite material has high sensitivity to out-of-plane failure resulting from the low interlaminar fracture toughness and have data limitations to describe the complexity of failure mechanism[2].

Figure 2 shows delamination as one of the predominant modes of failure in composite when there is no reinforcement in the thickness direction. And to increase the confidence level to implement composite material into aircraft structure, then need another technology to combine it. One of the suitable new technology to combine is by implementing strain sensor to make auto damage detection and continuous monitor the damage for Composite Structural Health Monitoring (SHM). This technology can increase market acceptance caused can increase safety and reliability the composite structure during operational.

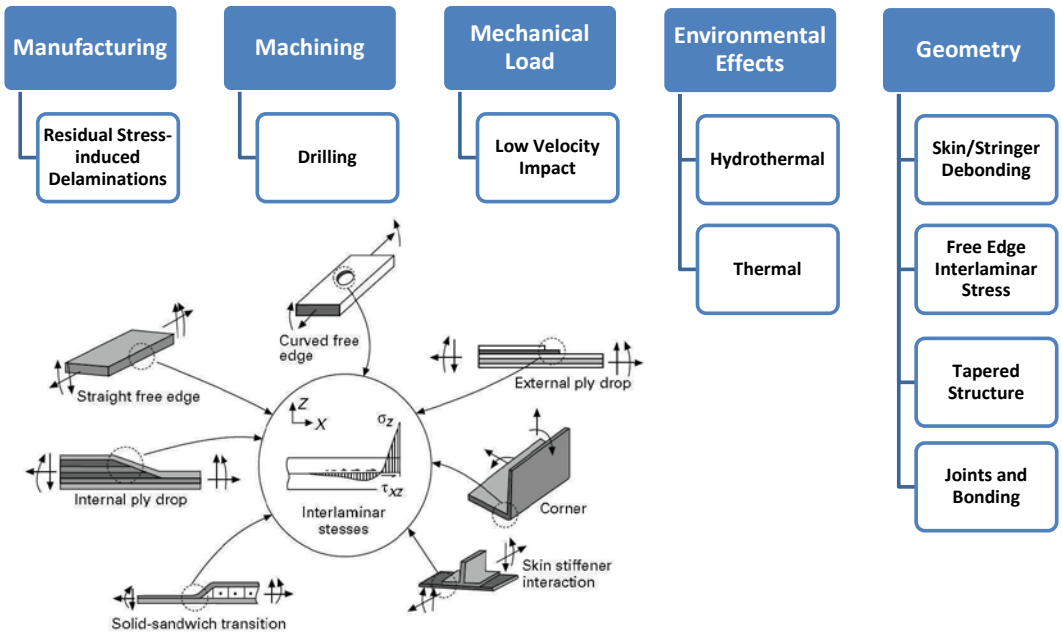

Figure 2 : Delamination Onset Causes.

However, composite materials provide challenges for design, manufacturing, maintenance and repair over metallic parts since they tend to fail by distributing and interacting damage modes. Furthermore, damage detection in composites is more difficult than in metallic structures. And the damage in composite materials often occurs beneath the top surface. Currently successful composite non-destructive inspection (NDI) for small laboratory specimens, such as X-radio graphic detection and C-scan detection, are impractical for in service inspection of integrated structure. Although inspection specifications for in-service composite airframes have published by the FAA[3], however the listed methods such as eddy-current and single-sided ultrasound are expensive, time-consuming and can be unreliable for large parts when applied to

composite structures. It is clear that new reliable approaches for damage detection in composites need to be developed to ensure that the cost of critical structures does not become a limiting factor in their use.

There are several documents issued by the Federal Aviation Administration (FAA) that regulate how the aircraft structure may be designed and inspected[3]. The FAR 25, a airworthiness standards for transport category airplanes, lists the acceptable engineering design criteria for the damage tolerance, which will be discussed further in the SHM motivation section. The Code of Federal Regulations (CFR) Title 14 Part 145 requires that all maintenance be performed using methods prescribed by Advisory Circular (AC) 43.13-IB. The certified techniques include visual inspection, liquid penetrant inspection, magnetic particle inspection, eddy current inspection, ultrasonic inspection, radiography, acoustic emission, and thermography. For each of these methods, a section is written in the AC that specifies the accepted procedure for each of these methods; along with detailed diagrams, checklists and reporting formats. For each certified commercial aircraft, an Aircraft Maintenance Manual (AMM) is created by the manufacturer in conjunction with the FAA CKR Title 14 Part 39 that lists each component to be inspected, the inspection interval, the type of damage to be concerned about, and the suggested methods to be used for the inspection. One example of the airworthiness directive, it

specifies for most composite components in commercial applications, currently only visual inspections are required. The aircraft is designed to be able to survive with any invisible damage, and there is a condition that such damage not grow over the period of two inspection intervals as determined by an instrumented coin tap test. Airbus A3XX as an example, the design service goal is 24,000 flights with general visual inspections every 24 months, and a detailed tear-down inspection for crack and corrosion via ultrasonic and eddy current techniques every 6,000 flights after the first 12,000 flights. While an A3XX under traditional practice would not undergo a thorough inspection in the first half of its expected life.

By using a SHM system, the structures would be constantly monitored without interruption of service and it reduce the aircraft grounded schedule. Its means can increase economic aspects for airliner who operate the aircraft. While in regulation, there is currently no specific provision in any of the published directives for a structural health monitoring system.

1.1.2. Structural health monitoring (SHM) for composite.

Composite Structural Heath Monitoring (SHM) has been defined in the literature[5] as the “acquisition, validation and analysis of technical data facilitate

life-cycle management decisions". More generally, SHM denotes a system with the ability to detect and interpret adverse "changes" in a structure in order to improve reliability and reduce life-cycle costs. The more fundamental challenge in designing a SHM system is knowing what "changes" to look for and how to identify them. The characteristics of damage in a particular structure plays a key role in defining the architecture of the SHM system. The resulting "changes", or damage signature, will dictate the type of sensors that is required. The development of reliable damage detection methods is critical to maintain the integrity of those structures. The following paragraph provides descriptions of various non-destructive inspection techniques that have been developed for the detection of damage in composite materials[6-7].

Visual Inspection Method - Perhaps the most natural form of evaluating composite materials is by visual inspection. Several variants of this method exist at various levels from the use of a static optical or scanning electron microscope to optical examination by eye over the structure. While microscopy can be a useful method to obtain detailed information such as micro-crack counting or delamination area. But it can only be used in the laboratory since a section must be removed from the larger structure. Visual inspection is the simplest and least expensive method. However damage in composite materials often occurs below the surface. While this method can

potentially provide some useful data for damage detection, on a large-scale structure this process would prove inefficient and ineffective.

Radiography Method - X-radiographic techniques depend on recording the difference in x-ray absorption rates through the surface of structure. These methods can be implemented in real-time digitally, or by taking static radiographs, whereas areas of different density are differentiated by the magnitude of x-ray exposure to the media on the opposite side of the surface after a predetermined excitation time. To highlight damaged regions with cracks or delamination, often a liquid penetrant is applied. These techniques are relatively inexpensive and simple to implement and interpret. They require large and costly equipment that is difficult to use in large part without removing them from the structures. The greatest challenge to use x-radiography methods in a structural application are that all require access to both sides of the surface in order to emit and collect the x-ray radiation, which is often not practical.

Strain Gauge Measurement Method - Strain gauge methods are perhaps currently the most common way to monitor the damage in composite materials on in-service structures. A voltage applied across a foil gauge is capable of measuring strain by the change in resistance due to deformation. These devices are relatively small, tight and inexpensive making them simple to implement, and their results are easily interpreted.

They are capable of monitoring local strain to detect time-history overloads and deformation. A disadvantage to this technique is that the results from a single gauge can only cover a small area of the surface accurately. It needs a large quantity of them to monitor an entire structure, yielding a complex system with many wires. In order to avoid this situation the gauges can only be placed in a few select predicted problem areas.

Ultrasonic Scanning Method - Another commonly implemented non destructive inspection technique is ultrasonic testing, most often referred to as A, B and C-scans. These tests are usually conducted with two coupled water-jet heads moving in tandem on either side of the specimen surface, sending ultrasonic waves through the water stream on one side, and collecting the transmitted acoustic waves on the opposite side. An A-scan refers to a single point measurement of density, a B-scan measures these variations along a single line, and a C-scan is a collection of B-scans forming a surface contour plot. The C-scan has been common practice in the aerospace industry since the results widely understood and can be used to scan a large area of structure, typically water is used as a couplant. Newer non-contact techniques have been attempted that use air as a couplant. Beyond the size and cost of the equipment there also is the problem that access is required for both sides of the structure. The parts must often be

disassembled for testing. Single-sided ultrasonic reflective methods are in development to remedy this problem.

Vibration-based Method - Most vibration-based damage detection techniques for composite materials have focused on modal response. Structures can be excited by ambient energy, an external shaker or embedded actuators, and the dynamic response is then recorded. Changes in normal modes can be correlated with loss of stiffness in a structure, and usually response-history tables are used to predict the corresponding location of damage. These methods are implemented easily within the existing infrastructure of a structure at a low cost. The data they produce can be complicated to interpret. This technique holds much potential for non destructive inspection methods within composite materials. Another popular vibration measurement technique in composites is acoustic emission (AE) test. Changes in material properties can be deduced using resonant beam sensors, accelerometers, piezoelectric, or microphones to record energy being released by matrix cracking or fibers fracturing. This method has the advantage to use an array of multiple sensors to triangulate the location of damage by the signal time of flight. Again, the data from this method can be complicated to interpret, but hold much potentially useful information for the detection of damage in composite materials.

Fiber Optic Strain sensor Method - In order to cover more area on a structure for strain measurement; another technique that has evolved is the embedded small-diameter optical fibers, which can be multiplexed to record measurement over large regions. In using this method, pulses of polarized laser light is transmitted along an optical fiber. The gratings are placed in various locations to reflect a portion of the light at a certain wavelength. By recording the time of beam flight, the length of the fiber segment can be easily deduced. If a strain has been applied to the fiber segment, the time of flight would change active areas. Opponents of optical fiber methods claim that mere is a large shear-lag effect due to the cladding, coating and adhesion layers surrounding the optical core that makes it impossible to take accurate measurements. Furthermore, these fibers introduce weak points in a laminate as potential crack and delamination initiation sites. But recent research has resulted that small-diameter of FBG sensor have no much influence in mechanical properties of composite. And now FBG sensor has potential widely used for aircraft structure applications since they can be easily multiplexed over long distance and can cover a wide area of inspection. In addition, it can be used as continues and real time damage detection and monitoring.

1.1.3. SHM in composite using fiber Bragg grating (FBG) sensors.

Fiber Bragg grating sensors have become of particular interest in this thesis due to

their ability to embed into the composite materials and structures. Currently the aerospace industry has one of the highest payoffs since damage can bad to catastrophic (and expensive) failures, and the vehicles involved undergo regular costly inspections. Currently 27% of an average aircraft's life cycle cost both for commercial and military vehicles, is spent on inspection and repair[8].

Figure 3 shows the FBG sensor basic operation which it follows the Fresnel reflection theory. Where light travelling has different refractive indices may both reflect and refract at the interface. While Fig.4 explains how the power reflection of FBG sensor work as strain sensors when each time light in the fiber encounter the FBG sensor's refractive index discontinuities during loading. When a tensile strain stretches the FBG sensor, it will increase the grating period (illustrated in yellow line). Therefore tensile strain also increase $\lambda_{Bragg.}$

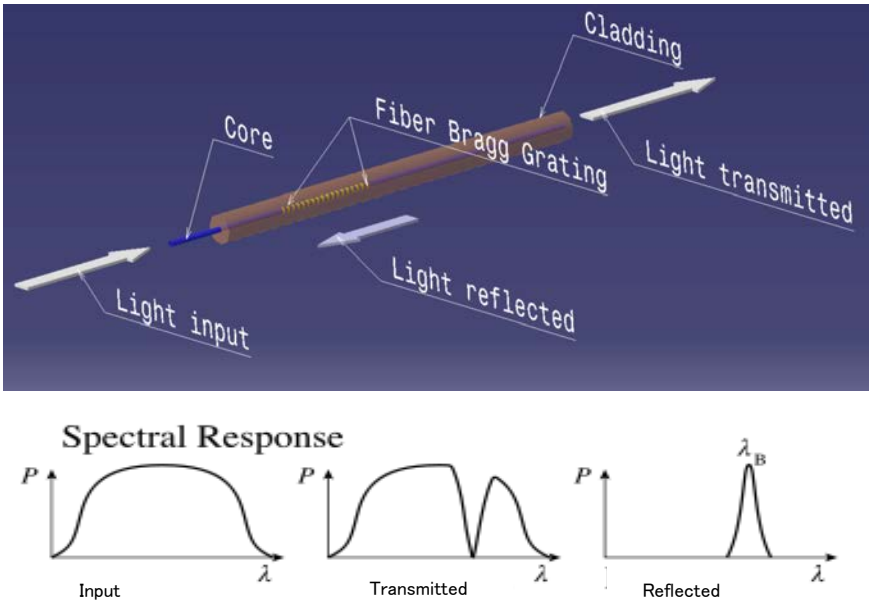

Figure 3 : Fiber Bragg grating optics and illustration of the principle.

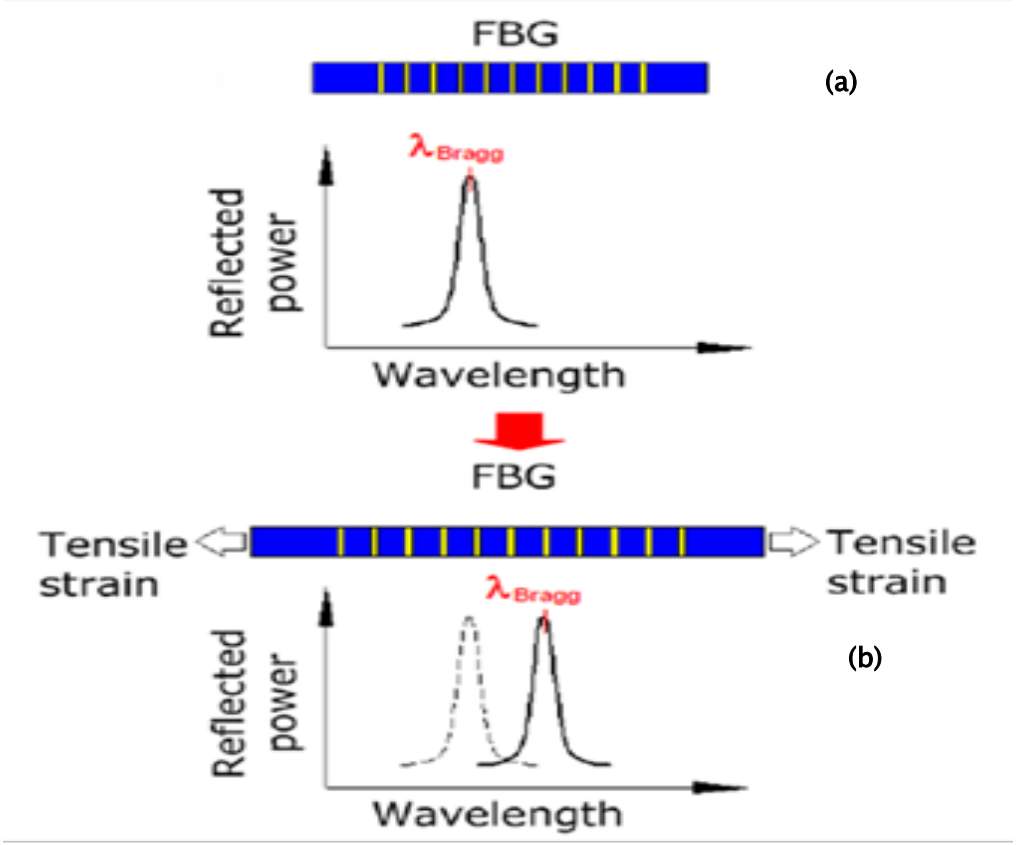

Figure 4 : The principle of power reflection of FBG as strain sensor; (a) No strain, (b) Under tensile strain.

The grating will typically have a sinusoidal refractive index variation over a defined length. The Bragg or reflected wavelength (λ_B) is defined by the relationship,

$$\lambda_B = 2\Pi\Lambda \quad (1)$$

Where Π is the effective refractive index of the grating in the fiber core and Λ is the grating period. When FBG sensors are being strained the wavelength of the reflection peak will be shifted. It is necessary to measure these shifts very precisely for strain measurement.

Formulation above effective for uniform strain, because Π (effective refractive index) and Λ (grating period) also uniform along the entire length of the FBG sensors and keeping the reflection spectrum to its original narrow shape. It also means that if the non - uniform strain induced to FBG sensor, the reflection spectrum will change not as original narrow shape again. This phenomenon will use to detect the damage with monitoring the change of reflection spectrum shape. The normal shape of the reflection spectrum can be determined by the following expression. Figure 5 shows the result of spectrum shape theoretically by using the followed formulation below.

$$Pi = \frac{\lambda 0}{\pi N\, \Delta\lambda i}\ sin\frac{\pi N\, \Delta\lambda i}{\lambda 0} \quad (2)$$

Where,

$$\lambda i = \lambda o + \Delta\lambda i \quad (3)$$

$$\nabla = \frac{\lambda 0}{2\,n} \tag{4}$$

$$N = \frac{Gl}{\nabla} \tag{5}$$

Equation (4) inserted into (5) gives;

$$N = \frac{2\,n\;Gl}{\lambda 0} \tag{6}$$

Where;

n (refraction index) = 1.46

λo (wavelength at center spectrum) = 1550 nm

Gl (grid length) = 15 mm

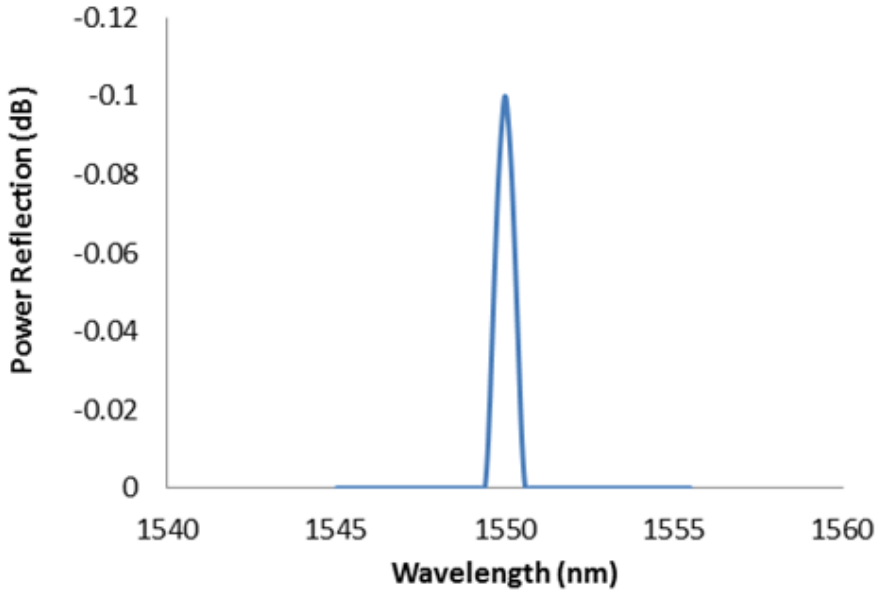

Figure 5 : Calculated power reflection.

1.1.4. Principle and capability of FBG sensor to detect damage in composite

The optical fiber is found at 1969 when first gradient index fibers were manufactured by the cooperation of Nippon Sheet Glass Co and Nippon Electric Co for telecommunication purposes. But the damping was still high about 100 dB/km caused mainly by chemical impurities of the glass. Good progress was reached at 1976 with damping was just less than 1 dB/km and it was available in Japan, USA, and UK[9].

Fiber Bragg gratings are created by "inscribing" system (periodic or aperiodic) variation of refractive index in the core of optical fiber using an intense ultraviolet (UV) source such as a UV laser. Two main processes are used: *interference* and *masking*. Which is best depends on the type of grating to be manufactured. These fibers contain a very small inner core of 4 μm to 9 μm diameter and a cladding of pure glass (SiO_2) of 50μm - 125μm diameter. The core has a higher refraction index caused by germanium doping. The difference between the inner core and cladding in refraction indexes causes the light to propagate only inside the small core. This behavior, then as advantage of fiber optic when the light pass through, which then the changes of the light intensity is used to determine strain and temperature on the composite structure.

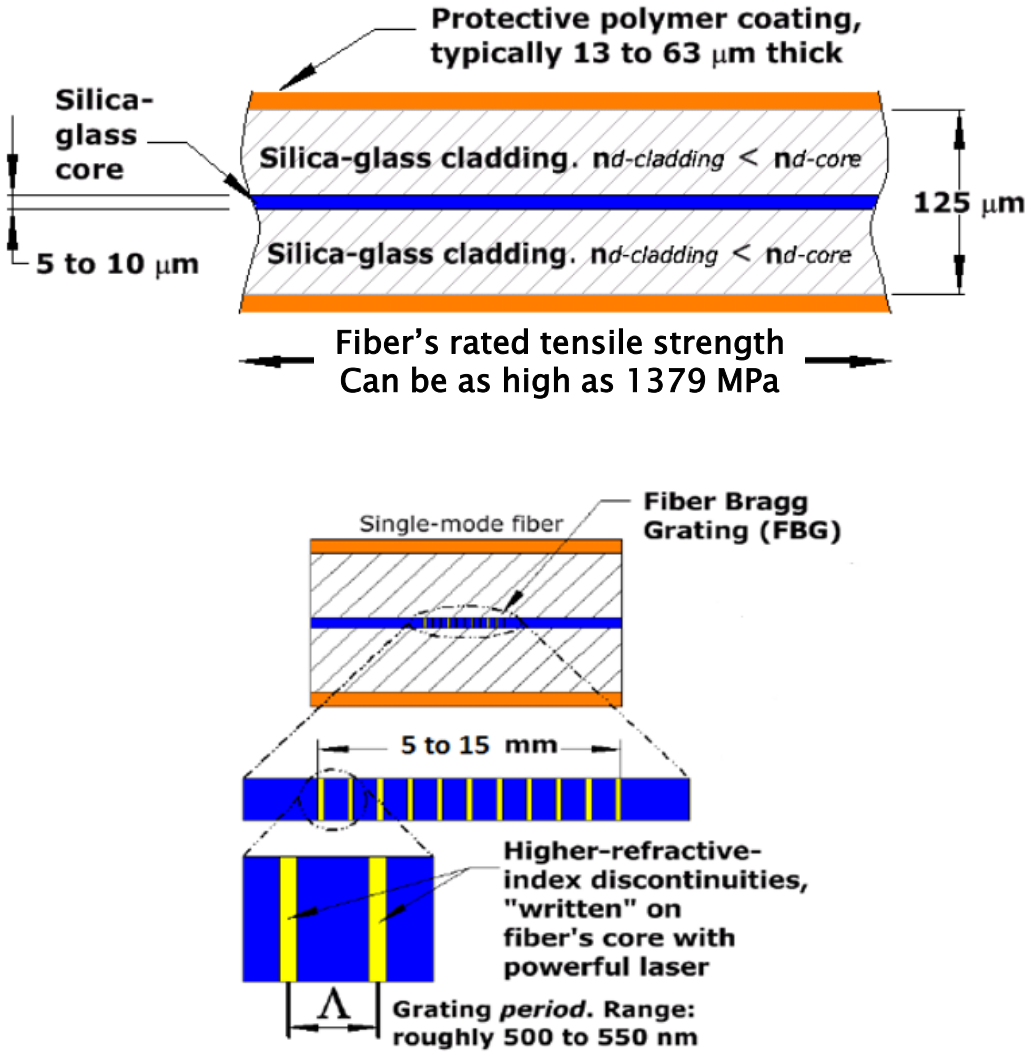

Figure 6 : Construction of FBG sensor.

To measure strain, the sensors must be fixed to the structure and usually by embedding during lay-up in the manufacturing process. Figure 6 shows stretching a FBG sensor cause a change in grating period and resulting a change in reflected wavelength.

To get correlation Bragg or reflected wavelength (λ_B) to mechanical strain and

temperature is defined by the relationship below,

Because there are several refractive indices in the one raw of FBG sensor, then the value of Π is the average refractive index in the grating.

$$\Pi = \frac{(\Pi 3 + \Pi 2)}{2} \quad (7)$$

The bandwidth ($\Delta\lambda$) or wavelength spacing between the first minimum, is given by;

$$\Delta\lambda = \frac{(2\delta\Pi 0 ή)}{\pi} \quad \lambda_B \quad 8)$$

Where $\delta\Pi$ is the variation in the refractive index, for example is Π_3 - Π_2 and ή is the fraction of power in the core.

The peak reflection ($P_B(\lambda_B)$) is given by,

$$P_B(\lambda_B) = \tanh^2 \left[\frac{N ή(V)\delta\Pi 0}{\Pi} \right] \quad (9)$$

Where N is the number of periodic variations. The full equation for the reflected power ($P_B(\lambda)$), is given by;

$$P_B(\lambda_B) = \frac{sinh^2[ή(V)\delta\Pi 0\sqrt{1-\Gamma^2}}{cosh^2\left[ή(V)\delta\Pi 0\sqrt{1-\Gamma^2}\frac{N\nabla}{\lambda}\right]-} \frac{N\nabla/\lambda}{\Gamma^2} \quad (10)$$

Where,

$$\Gamma = \frac{1}{ή(V)\delta\Pi 0} \left[\frac{\lambda}{\lambda B} - 1\right] \quad (11)$$

After discussion about FBG sensors in relation to the wavelength (λ_B) with electrical power $P_B(\lambda_B)$. And now following how the relationship between wavelength

(λ_B) is the mechanical-strain. When FBG sensors are being strained the wavelength of the reflection peak will be shifted. It is necessary to measure these shifts very precisely for strain measurement. And the wavelength of an FBG sensor change with strain and also temperature is according to the equation below;

$$\frac{\Delta\lambda}{\lambda 0} = \text{ƙ}\ \varepsilon + \alpha_r\ \Delta T \qquad (12)$$

Where,

$\Delta\lambda$ = wavelength shift

λ_0 = wavelength at center spectrum

Ƙ = 1 – p

p = photo elastic coefficient, which is p = 0.22

ε = elastic strain

ΔT = temperature change in K

α_r = glass refraction index's coefficient thermal of expansion

and, $\alpha_\delta = \frac{\delta\Pi/\Pi}{\delta T}$ (13)

The expression (ƙ. ε) explains about strain caused by mechanical force (ε_m) and temperature (ε_t). While (α_r. ΔT) explains about the change of the glass refraction index Π caused only by temperature. And the strain is affected by two things, namely mechanical and temperature then,

$$\varepsilon = \varepsilon_m + \varepsilon_t \quad (14)$$

Where,

ε_m = mechanical strain.

ε_t = strain caused by environmental temperature

And $\varepsilon_t = \alpha_c \Delta T$

α_c = composite's coefficient thermal of expansion.

Base on the equation above, will clear the behavior of FBG sensors within the influence of strain and temperature. Inserted the equation (9) and (12) into equation (9), then the equation will be,

$$\frac{\Delta\lambda}{\lambda 0} = (1 - p)(\varepsilon_m + \alpha_c \Delta T) + \frac{\delta\Pi/\Pi}{\delta T} \Delta T \quad (15)$$

In case FBG sensors is installed in the structure/part without mechanical strain happen then it works as a temperature compensation only. Then the formulation FBG sensor become,

$$\frac{\Delta\lambda}{\lambda 0} = K \alpha_c \Delta T + \frac{\delta\Pi/\Pi}{\delta T} \Delta T \quad (16)$$

Then,

$$\Delta T = \frac{1}{K\alpha c + \frac{\delta\Pi/\Pi}{\delta T}} + \frac{\Delta\lambda}{\lambda 0}$$

$$= \frac{1}{K\alpha c + \alpha\delta} + \frac{\Delta\lambda}{\lambda 0} \quad (19)$$

This formulation is for FBG sensor temperature compensation.

1.2. Previous Research.

The increasing application of composite materials but with a complex damage mechanism and has difficulty to inspect encouraged authors to do research in damage detection as a structural health monitoring approach. The problem may be equally design concepts, numerically as planning in FBG sensor placement, experimentally in static test and FBG sensor reading and nondestructive inspection for damage quantifying. Damage detection in a material modification and a structure problem is focused to verify the capability of FBG sensor.

In material modification problem: Arief et al (2011) revealed the effect of Vectran-stitch in laminate in various stitch density subjected to static and fatigue loads in-plane direction[11-12]. Tan et al (2009) examined the effectiveness of Vectran-stitch in mode I interlaminar fracture toughness and low velocity impact[13-14]. Yoshimura et al (2007) showed the effect of high stitch density in a laminate to tensile properties[15]. Mouritz et al (1997) reported the correlation between stitching and tensile performance[16]. Thuis et al (1996) revealed the reducing tensile properties caused by high density stitching. Most researchers showed how complex the failure mechanism of stitched laminate material[17]. Parts of them explained the increasing mechanical properties of laminate after stitching process induced, but others researcher explained contrary especially in in-plane direction. This indicated how the manufacturing process

and stitching material selection were very important. And very rare of them have conducted research in stitched laminate material combining with an embedded FBG sensor in damage detection, especially used patented special stitching machine of Toyota Industries Corporation.

While in structure problem, several researchers have conducted the research such as: M.D.Todd et al (2009) used ultrasonic chaotic excitations to detect damage in composite stiffened (rectangular) panel[18]. Jung-Ryul Lee et al (2008) monitor buckling behavior in composite wing box using FBG sensor[19]. R.Jones et al (2002) used FBG sensor to detect damage in composite sandwich repair in butt-joint[20]. W.K.Chiu et al (2000) used piezoceramics to detect damage in bonded repair application[21]. Most of researchers conducted the research in linear strain mode when FBG sensor spectrum still in original shape during structure loading in composite structural case.

There is lack research that encouraged authors to introduce a research especially to detect global stiffness degradation of stitched laminate material and to detect damage caused by indirect load in a thin composite structure with mismatch stiffened in non-linear strain mode. In the present work's author's attention is focused on damage detection, characterization and quantification by using FBG sensors.

1.3. Research Objectives

This thesis provides a comprehensive understanding of the capability optical fiber sensor systems, namely fiber Bragg grating sensor (hereafter, 'FBG sensor'), to monitor damage behavior in composite materials and structures under mechanical loading.

The FBG sensor is embedded in two types of composite systems: (i) stitched laminate materials, (ii) thin composite structure with stiffness mismatch. These composite systems are subjected to two load cases, i.e. static tension and three-point-bending. The stitched laminate materials, which have through-thickness reinforcement in the form of stitch threads, exhibit a complex failure mechanism. Thin composite structures with stiffness mismatch exhibit secondary bending moment due to the shift of neutral-axis. This neutral-axis shift eventually causes delamination, which is generated by high peel stresses at the edge of a stiffener. Two research areas will be used to prove the capability of an FBG sensor in damage monitoring as follows:

The first area of study is to use an FBG sensor as damage detection tools in thin composite structure with stiffness mismatch. The alignment of the load path and the geometry of the structural elements are important considerations in the design joints. Primary bending is avoided by keeping the loading as close as possible to the neutral-axis. However, secondary bending moments induced by minor eccentricities of the loads occurs in many types of joints (and structures) and can cause serious problems.

The scheme is to automatically and continuously detect and characterize damage using FBG sensor. Bonded joint only and combined (riveted/bonded) joint under tensile and three-point-bending loading are used. Cohesive zone model theory as finite element method is performed to determine the critical area on the specimen for FBG sensor installation before manufacturing. Experiments were conducted to determine the distribution of load under both loading cases to create a secondary bending moment on the specimen. Loading/un-loading test combining with C-scan inspection is also performed to monitor delamination growth and to quantify the delamination growth. This area is used to prove the capability of FBG sensor to detect local stiffness degradation in the composite structure.

A second area of study is to use an FBG sensor to prove its capability to detect global stiffness degradation in stitched laminate material and continuous monitoring during loading run. This material used caused by providing a complexity failure mechanism and as the best method in material modification by inserting fiber reinforcement in through-the-thickness direction to increase the damage resistant. Numerical analysis using classical lamination theory and first ply failure are performed to embed the FBG sensor as close as possible with total laminate failure. The results of a tensile test under loading/un-loading of the stitched laminate material are then

compared with the result of C-scan data to quantify the damage growth. Acoustic emission test is also conducted to enhance data of FBG sensor reading.

1.4. Research Methodology

Research is a structured inquiry that utilizes acceptable scientific methodology to solve problems and create new knowledge that is generally applicable. A scientific methodology proposed here to test hypotheses of SHM by using an FBG sensor. And a good design should ensure that the research is valid, i.e. it is clearly testing the hypotheses and not extraneous variables, and that the research is reliable. Part of the methodology is concerned with how the research is conducted and it encompasses the procedures followed to analyze, experiments and interpret the data gathered. The methodology here followed by the objective as a representative research which it can be difficult to conduct because tests can normally only be conducted on a small sample. This means that it needs to have a very detailed understanding of the types and limitations of research methodologies which it used. So the objective here means; to discover new facts, to verify and test old facts and to develop new scientific tool concepts in SHM. One of the first steps in this methodology here is to design a research flow for establishing the design requirements and objectives (DR&O) as research

direction to ensure that the final step meets the requirements, and to aid in future development.

Figure 7 shows the design evolution chart to make research methodology in composite structural health monitoring. This evolution divided into several steps after DR&O decided. The stepping will explain as follows below:

Design concept: In any theoretical or empirical work in which design is a construct, a clear definition to ensure construction validity. Furthermore, a clear understanding of the meaning of design will facilitate developing measures of design-related constructs. Then important to start this research by determining what design concept will be used to prove the ability of FBG sensor to detect the damage. It is important in this phase to define what materials selection design, what composite construction will be used, and theory following the design selection.

Stress mapping analysis in the model: Numerical analysis starts to use after design concepts have done. The main purposed is to map the stress distribution in entire model and to predict failure behavior in the model. Two theories will be used to predict the mechanical behavior of the materials and composite structures. First is a cohesive zone model theory used to predict mechanical behavior in thin composite structure with

stiffness mismatch and the second is the classical laminate theory with first ply failure used to predict stitched laminate materials failure.

Critical area selection based on loading case: However, FBG sensor has potential weakness which it detects damage just near the grating length. And with the data result produced by stress mapping analysis, we can determine the critical area that becomes a reference for FBG sensor installation in damage detection.

Determination of FBG sensor location within the model: Optimization FBG sensor placement can be determined after the critical area within the model is known. It is important to avoid FBG sensor misreading in damage detection. This step becomes a crucial reference before specimen fabrication.

Preparation for composite parts fabrication: Many techniques available in composite fabrication starting in simple mode by using wet lamination, then goes to pre-impregnated until 3D preform involving non-pressurized or pressurized combining with low or high-temperature. The function and parts mission will determine the fabrication method selection. This research used two methods of fabrication. First is to use 3D preform with a VaRTM method for stitched laminate material and the second is to use high temperature pre-impregnated with secondary bonding in composite structure with stiffness mismatch.

Material/structure ready: After all above are satisfied, the parts/specimens ready to assemble to another structure or ready to go to the test scenario.

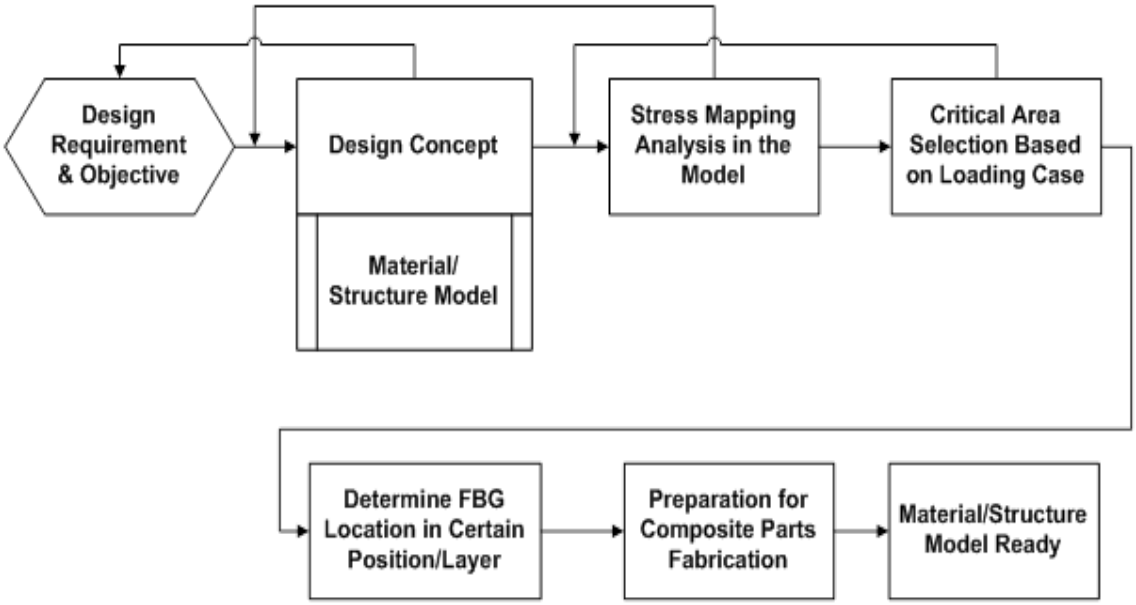

Figure 7 : Design evolution charts before FBG sensor installation.

1.5. Layout of Thesis

The thesis is divided five chapters as follows:

Chapter 1 presents the introduction, which contains the research background and future needs of structural health monitoring (SHM) that is implemented in composite aircraft structure and literature survey on work done by researchers in the field of SHM by using FBG sensors. Some research work regarding with complex mechanism of stitched laminate material and come application of FBG sensor in joining are reviewed. The research methodology is also proposed to identify several key of designs especially in the instilling assessment of FBG sensor into composite materials.

Chapter 2 presents damage detection and monitoring of thin composite structures with stiffness mismatch using FBG sensor under tensile and three-point-bending load. The FBG sensor is used to detect local stiffness degradation of a thin composite with stiffness mismatch. Finite element analysis (FEA) using a cohesive zone model is used to determine the critical area in composites for FBG sensor placement before manufacturing. The actual strain measured from the strain gauges attached on the surface of composites has a close agreement with those obtained by FEA. C-scan inspection is also conducted to observe the delamination growth in composites. The C-scan data combined with those obtained from FBG sensor is considered for the quantification of delamination growth. It is found that FBG sensor

data can be used to detect and characterize delamination caused by secondary bending moment that occurs in a thin composite with stiffness mismatch.

Chapter 3 presents damage detection and monitoring of stitched laminate materials using FBG sensor under tensile loading. The FBG sensor is used to detect global stiffness degradation in the Vectran-stitched laminates with stitch density of 6x6. Classical lamination theory and first-ply failure criterions are adopted to determine the preferred area in stitched specimen for the FBG sensor placement before manufacturing. Real-time monitoring using the FBG sensor system combined with the acoustic emissions test is conducted during a tensile test. Interrupted test combined with C-scan inspection is performed for the determination and quantification of damage growth in stitched laminates. It is found that the FBG sensor can be used to detect, characterize and quantify the global stiffness degradation in stitched laminate materials.

Chapter 4 presents the conclusions and recommendation made from the findings previously discussed in Chapter 1-3. This chapter discusses SHM system, and recommends the design of an effective in-situ damage detection system for composite materials and structures. It is found that the FBG sensor can provide a structural integrity profile in real-time basis during the operation. FBG sensor can also provide more detailed information since it can be embedded within composite materials. SHM is

likely to be an important component in the aircraft design in order to increase the feasibility of the mission and the reduction of their life-cycle costs. All empirical data presented in this thesis has proven that FBG sensor is an effective tool to detect damage in composite materials and structures. FBG sensor has a great potential to change the conceptual design and the maintenance process of the aircraft.

CHAPTER 2 : DAMAGE DETECTION AND MONITORING OF THIN COMPOSITE STRUCTURE.

2.1. Overview

One of the problems associated with loading in a fully composite structure with joints is that the loads are not linear through the neutral axis of the structure but are shifted. This induces secondary bending moment and creates a load in the normal direction, which is typically a critical load because it can create delamination only with a small load. Another problem is that the structure is difficult to inspect using conventional methods because of limited accessibility. The use of embedded FBG sensor technology in the structure as a strain sensor can potentially solve the problem in a thin composite structures that have a stiffness mismatch. The FBG sensor can be used to detect, continuous monitoring and characterize the delamination. Two types of joint proposed to prove the FBG sensor capability in damage detection in a thin composite structure problem. They were bonded joint only and combined (riveted/bonded) joint under tensile and three point bending loading. Finite element analysis using a cohesive zone model theory is performed to determine the critical area for placement of the FBG sensor before manufacturing. Experiments were presented to determine the distribution of load under both loading cases to create a secondary bending moment. Loading-unloading test is also performed to get damage propagation. Damage

quantification is performed based on loading-unloading test result, C-scan result and spectrum reflection result under FBG sensor reading.

2.2. General Design Concept

Figure 8 shows the aircraft structure which it consists essentially an assembly of simple parts connected to form a load transmission path. The parts, which include skins, stiffeners, frames, and spars, form the major components, such as wings, the fuselage, and the empennage. The load path will flow from the skin to other parts via joining. The joints are potentially the weakest points in the airframe structure, and they determine its structural efficiency.

A combined joint in a composite structure is the merging of technology between adhesive bonding (chemical technology) and fasteners (mechanical technology). In bonded joints, it is required that the surface of adherend should be clean and in a controlled environment. The bonded area is sensitive to humidity and temperature. The joints can distribute a load over a large area relatively uniformly compared with a mechanical joint and can eliminate stress concentrations. However, disassembling an adhesive-bonded joint without causing any damage is problematic.

In contrast, mechanical joints (i.e., joints with fasteners) can be disassembled and are not sensitive to surface cleanliness, humidity and temperature. The drilling of

holes in the parts to be joined obviously weakens the joint because it creates stress concentrations. Therefore, mechanical joints require local strengthening such as doublers, metallic interleaving, softening shims or a local overlay layer to improve the fastened joint strength, which can increase the weight of the structure.

Combining both technologies in a combined joint (bonded/riveted) has been considered in terms of structural performance in transfer loading although these assumptions usually pertain to high-performance aerospace joints.

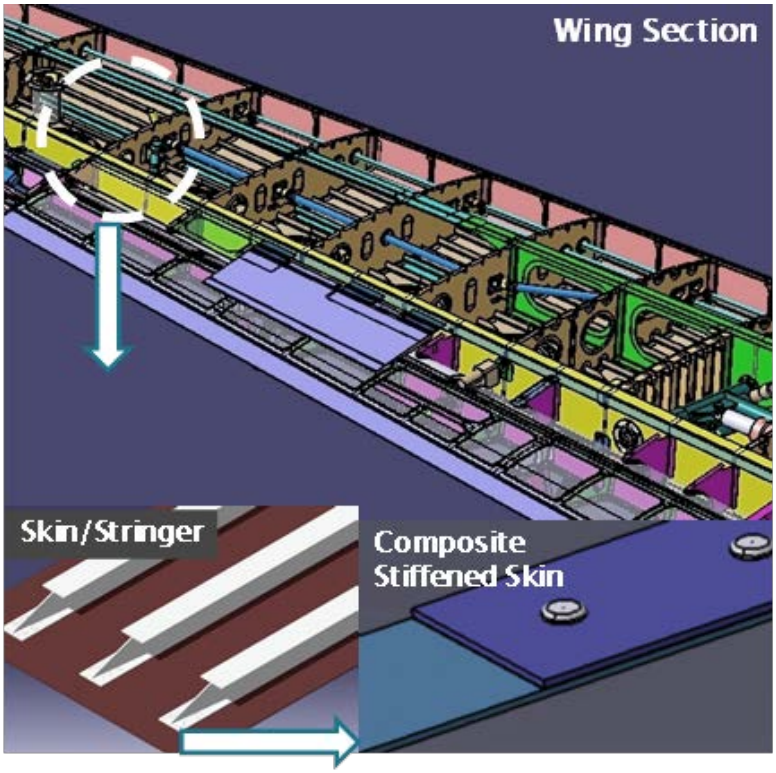

Figure 8 : Specimen for fundamental testing (composite structure with stiffness mismatch) inspired by a skin stringer structure.

The alignment of the load path and the geometry of the structural elements are important considerations in the design of joints. Aircraft structural elements are generally intended to be loaded in either tension/compression or shear modes. Primary bending is avoided by keeping the loading as close as possible to the neutral axis. Figure 9 shows the secondary bending moment induced by minor eccentricities of the loads occurs in many types of joints and can cause serious problems. Because there is less available information on composite materials and structures, especially in failure mechanisms, structural aircraft designs often incorporate over-strengthening. The fear of failure prompts, too-frequent manual inspections of the structure. In the long run, these factors lead to inflated airline operating costs[22-24].

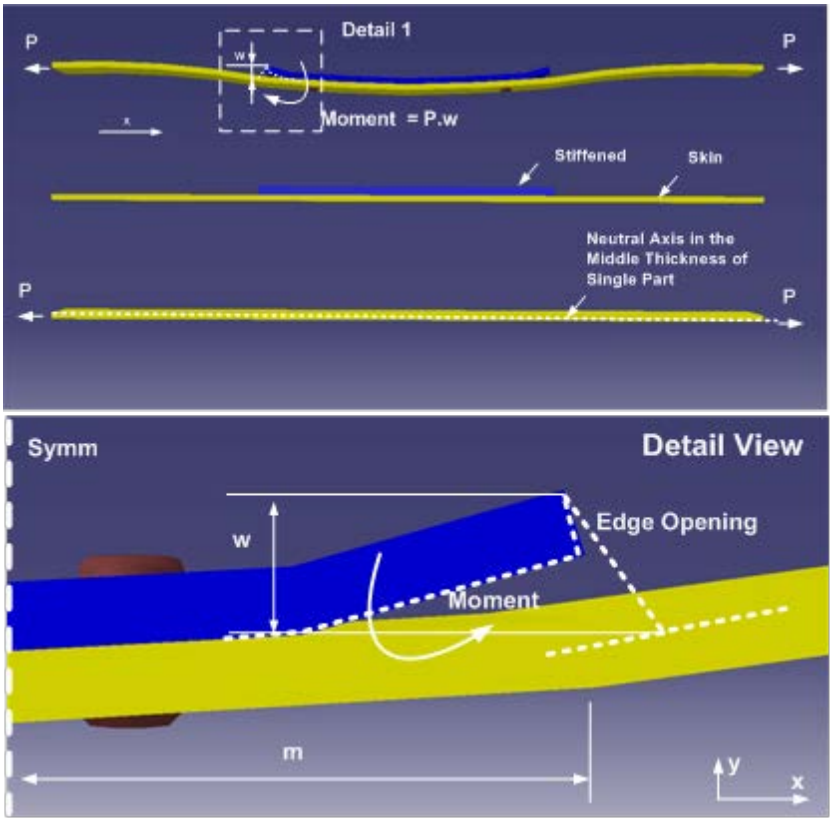

Figure 9 : The secondary bending phenomena illustration in the composite structure with stiffness mismatch.

Structural health monitoring can offer a good solution to this problem and is performed by embedding FBG sensor during the manufacturing process. This component monitors structural degradation due to external forces or environment/temperature. One of the problems in implementing FBG sensor in the composite structure is that it is difficult to guarantee that a failure will occur close enough to an FBG sensor location to allow for strain transfer[25-27].

2.3. Numerical Analysis

2.3.1. Specimen Configuration.

Figure 10 shows a simplified model to perform fundamental tests on failures caused by secondary bending moments and to monitor them using the FBG sensor. Carbon fiber unidirectional impregnated IMS60/#133 (Toho Tenax) was used for laminate. The composite was eight-layer anisotropic $[0,0,45,-45]_s$, and it was fabricated by autoclaving at $\pm 180^0$ C to produce the following mechanical properties: σ_t = 2201 MPa, σ_c = 1037 MPa, τ_t = 207 MPa, E_t = 150 GPa, E_c = 137 GPa, G_{tc} = 10.9 GPa, and ν_{tc} = 0.33. The material was cut with diamond cutting machines into the desired dimensions. The interface between the composite skin and the stiffener was bonded using the room-temperature adhesive DP420 Off-White from 3M with a double-stage bonding method containing the following mechanical properties: τ_s = 20 MPa, τ_n = 17 MPa, τ_t = 207 MPa, and E_t = 2000 MPa. The bonding area was roughened with fine abrasive paper and cleaned with acetone before the bonding process. AN470 AD5 rivets with Φ 3.2 mm were installed into the specimen using a 0.30 MPa pressured rivet gun after adhesive cured.

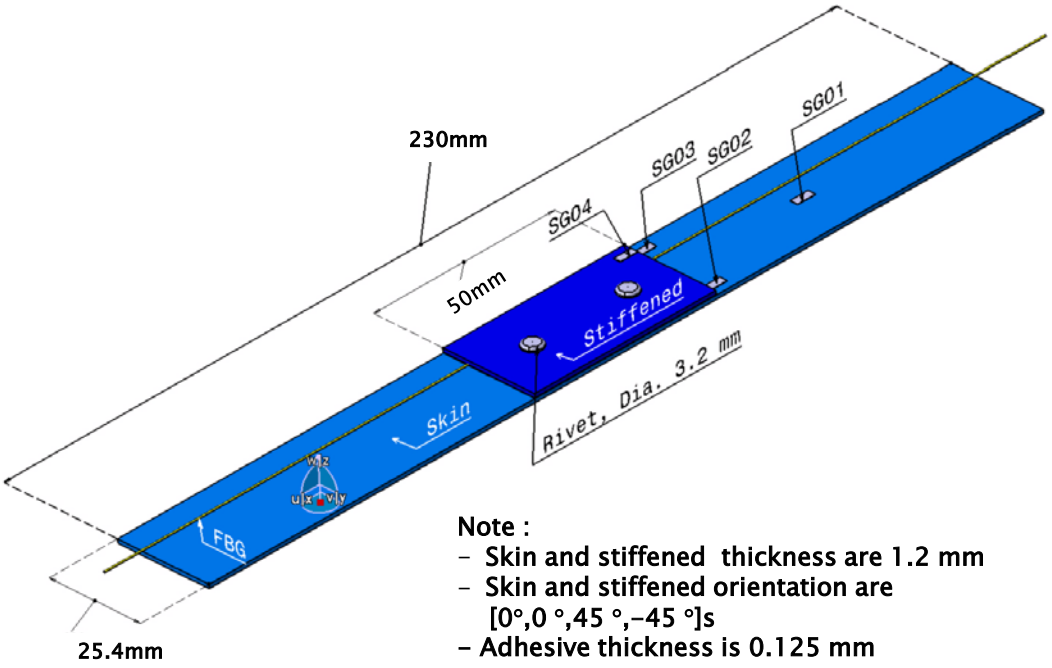

Figure 10 : Specimen dimensions and configuration with FBG sensor installed inside.

2.3.2. Methodology

2.3.2.1. FEM Analysis Parameter

The fates of the edges of the stiffener, the adhesive, and the riveted joint were investigated by using the ABAQUS. The joint configuration used was a combination riveted/bonded method for a a thin composite structure with stiffness mismatch. The rivet geometry was maintained as a constant throughout the analyses. In addition to predictions of the load transfer in the joint, a stress analysis was performed to investigate the peeling effect and to determine the shear stress distributions in the adhesive and the riveted joint. To describe the adhesive cracks that cause delamination,

cohesive elements are used, and this approach has risen in popularity over the years. This interest is principally due to the ease of implementation and the clear virtual picture that is given by an explicit representation of delamination. After the mechanical behavior is investigated, the specimen was fabricated and the FBG sensor was installed in the specimen. The experimental results were used to validate the predicted values from the finite element model. The cohesive zone model theory is a well-known theory used to model the onset of delamination[28-30].

The analyses were performed by inducing a tensile load at one end of the joint, which was only free to move in the longitudinal (x) direction ($u_y u_z = 0$). The opposite end of the joint had clamped boundary conditions. Because it was fixed in the (z) direction, this model was represented as a half-model. In another test using three-point bending conditions, the piece is free to move (roll-support) in the longitudinal (x) and normal (z) directions ($u_y = 0$) with loading on the center back side of the stiffener. The effects of non-linear geometry were included in the analyses to overcome deformation on stiffened area.

2.3.2.2. Cohesive Zone Model Laws

Delamination is one of the main modes of failure in composites when there is no reinforcement in the thickness direction. Prediction of delamination can be

performed using cohesive elements, which combine aspects of strength analysis to predict the onset of damage at the interface and fracture mechanics to predict the propagation of a delamination. Cohesive elements have been found useful to study fracture along the interfaces of contact materials that have the same stiffness or thickness.

A cohesive constitutive law correlates the traction σ to the displacement δ at the interface. Figure 11 shows bilinear softening model, which is chosen here for its simplicity. One characteristic of all softening models is that the cohesive zone can still transfer load after the onset of damage. For pure Mode I, II or III loading, the stiffnesses are gradually reduced to zero after the interfacial normal or shear tractions reach their particular interlaminar tensile or shear strengths. The areas under the traction-displacement curves are the respective modes (I, II or III) of the fracture energy[31-33].

The penalty stiffness *K* is an arbitrarily large number selected such that the presence of undamaged cohesive elements does not introduce substantial compliance to the structure. A cohesive law is assumed to have three fracture modes. It is assumed that direction 3 is normal to the interface and that the interlaminar shear strength δ_{shear} is independent of the shearing direction. Then, the displacements for

damage initiation in each mode are simplified by the equations below:

Mode I : $\delta_3^0 = \frac{\sigma_3^0}{K}$

Mode II : $\delta_2^0 = \frac{\tau_{shear}^0}{K}$

Mode III : $\delta_1^0 = \frac{\tau_{shear}^0}{K}$

The constitutive response of the theory used here is based on the maximum stress criterion and is as follows:

MAX { $\frac{\sigma n}{Nmax}$, $\frac{\sigma t}{Tmax}$, $\frac{\sigma s}{Smax}$ }

The quadratic stress interaction criterion is

$$(\sigma_n) = \begin{cases} \sigma_n \, for \, \sigma_n > 0 \\ 0 \, for \, \sigma_n < 0 \end{cases}$$

$$\left\{ \frac{\sigma_n}{(N_{max})^2} + \frac{\sigma_t}{(T_{max})^2} + \frac{\sigma_s}{(S_{max})^2} \right\} = 1$$

Note:

σ_n = nominal stress in the normal direction

σ_t = nominal stress in the first shear direction

σ_s = nominal stress in the second shear direction

N_{max}, T_{max} and S_{max} = Damage initiation criterion

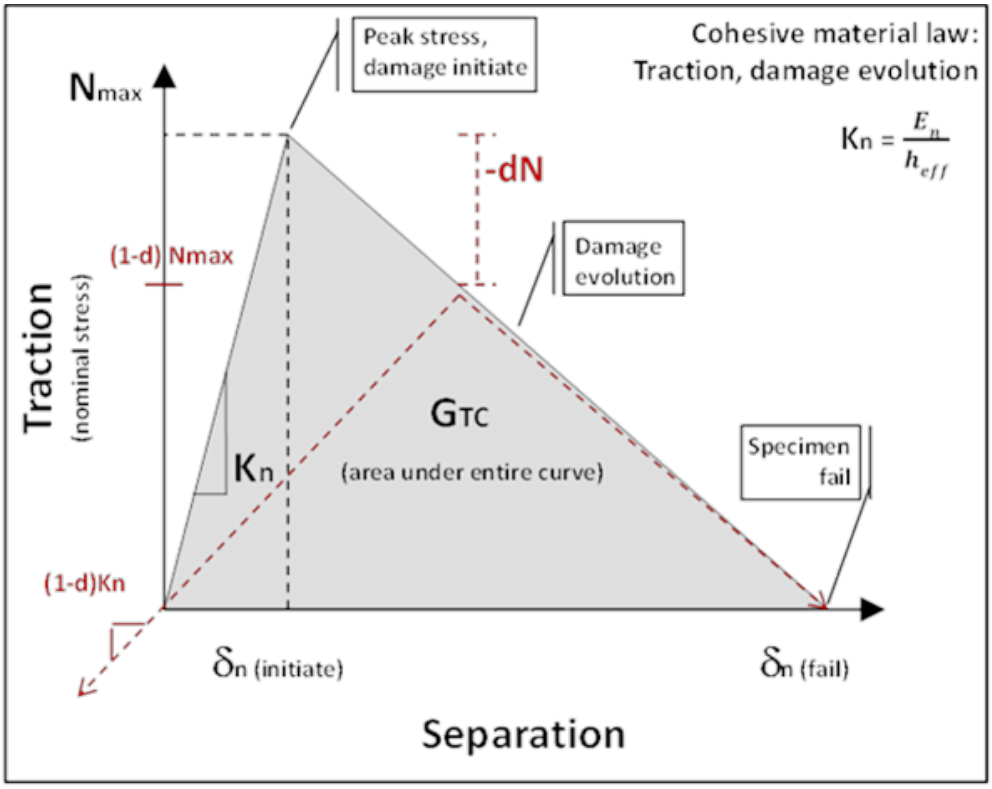

Figure 11 : Onset of delamination based on the cohesive zone model theory.

Note of Fig.11:

K_n = Penalty stiffened

h_{eff}= Geometrical thickness

d = scalar damage variable

d = 0: no damage

d = 1: fully damaged

In Fig.12, it can be verified and proved that delamination onset happens on the stiffener edge, and growth starts at that location because of the stress concentration

created on the edge of the stiffened area. However, no out-of-plane behavior virtually occurs in this model because the element-based cohesive zone model theory is a shell, which is not considered normal directional behavior.

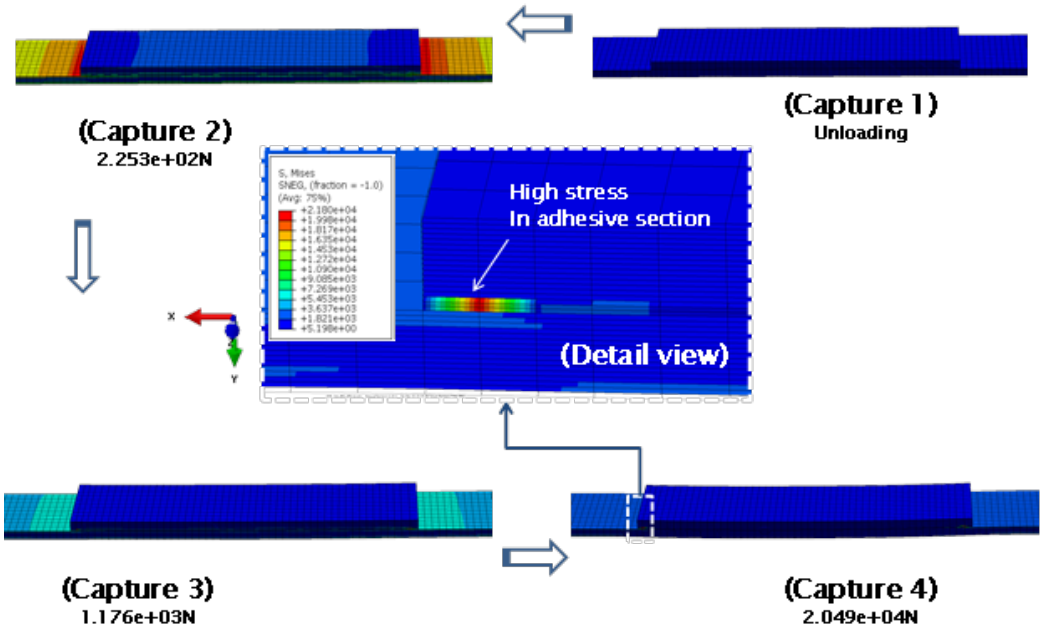

Figure 12 : Delamination onset based on Cohesive zone model theory.

2.3.3. Three-dimensions and Elements Modelling

Figure 13 shows three-dimensional models were built using a partitioned solid model in the thickness direction with a pointed section as the shell-composite for the laminate, a cohesive element for the adhesive and solid-homogeneous element for the rivet. While Fig.14 shows element model differences used as reference to built three dimensional model.

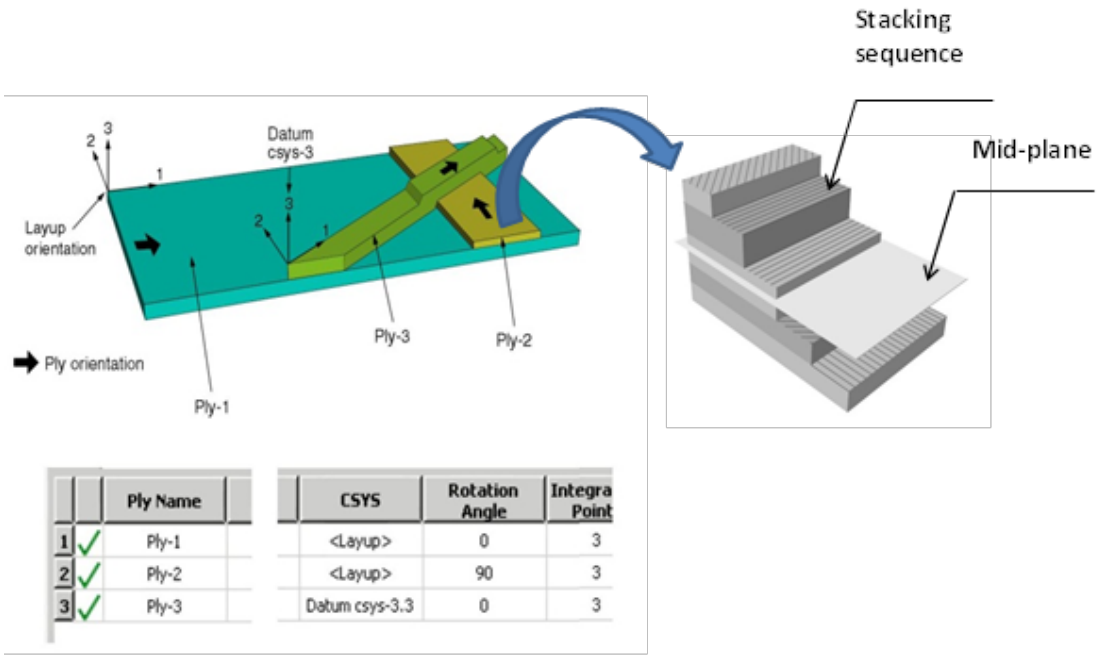

	Ply Name
1	Ply-1
2	Ply-2
3	Ply-3

CSYS	Rotation Angle	Integra Point
<Layup>	0	3
<Layup>	90	3
Datum csys-3.3	0	3

Figure 13 : Three-dimensional solid modelling.

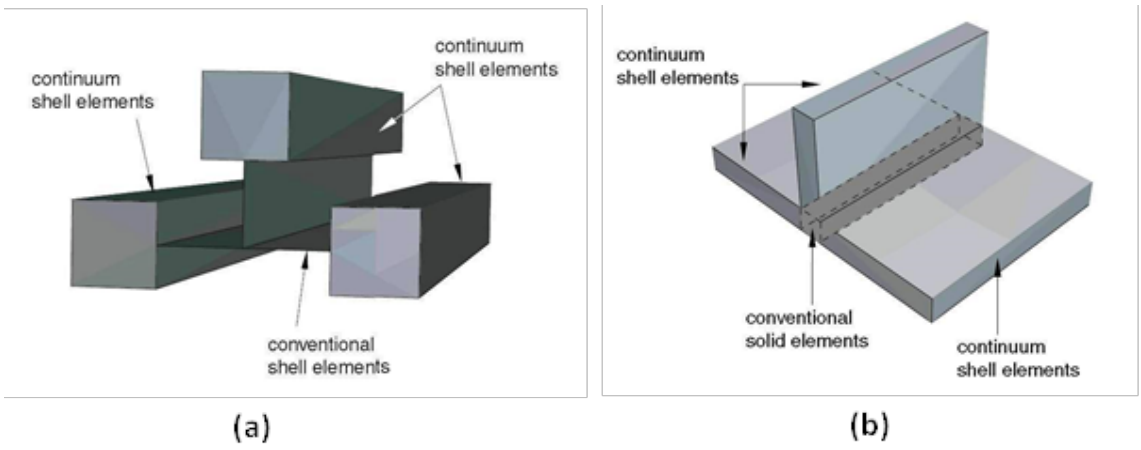

Figure 14 : (a) Conventional shell-to-continuum shell element and

(b) continuum shell-to-conventional solid element.

Figure 15 shows the three dimensional element which it laminate (the skin/stiffener) was modelled using an 8-node quadrilateral in-plane continuum shell

with hourglass control and with multiple elements in the thickness direction, which improved the performance of the elements under bending. The adhesive was modelled using 8-node three-dimensional cohesive elements. The rivet was modelled using an 8-node linear brick with hourglass control. A medial axis transform was used to generate the mesh, and a neat fit was assumed between the rivet and the laminate in all of the simulations. Symmetry was adopted along the length of the joint, and the model was thus reduced to a half-model to reduce the computational time. To accurately determine the mechanical behavior, including the load transfer at the interface of the adhesive and rivet, a three-dimensional model was required wherein the pair contact between the rivet and hole was modelled with a master-slave algorithm that allowed finite sliding of the contact pairing assuming a value of 0.2 for the friction coefficient; the adhesive was modelled using 8-node three-dimensional cohesive elements. To blur the dissimilar surface junction, the nodes used in interaction of the parts were merged, and all degrees of freedom at the node were merged together so that the meshing retains a good shape[33-40].

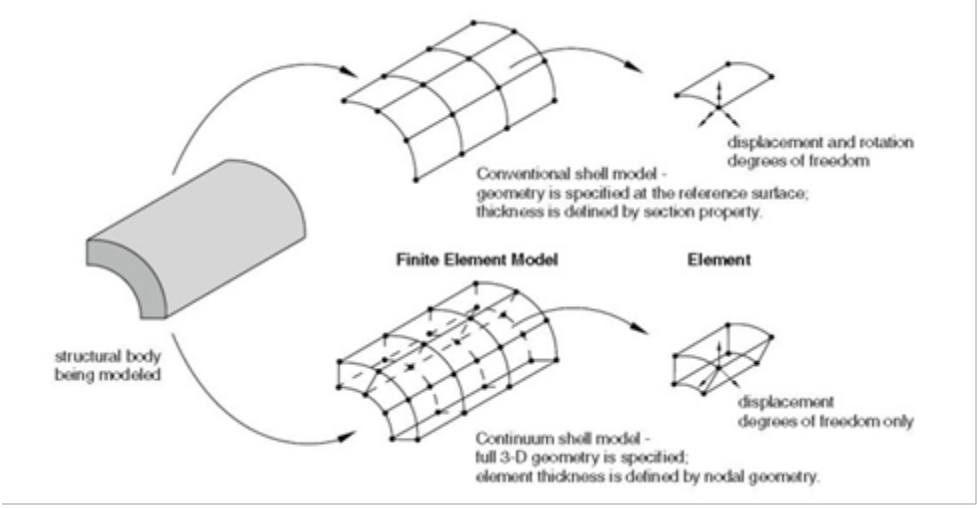

Figure 15 : 3D Element Modelling.

Figure 16 shows the meshes at the tie constraint region for the interaction between the parts, where the meshes created on the surfaces of the regions are dissimilar. The two parts will have no relative motion between them, and the positions of the nodes are not juxtaposed have possibility only displacement degrees of freedom are tied. While Fig.17 shows the meshes for the interactions between the parts when the nodes are merged. With merged nodes, there is no dissimilar surface region, and all the degrees of freedom at a node are merged together and the mesh has a good shape.

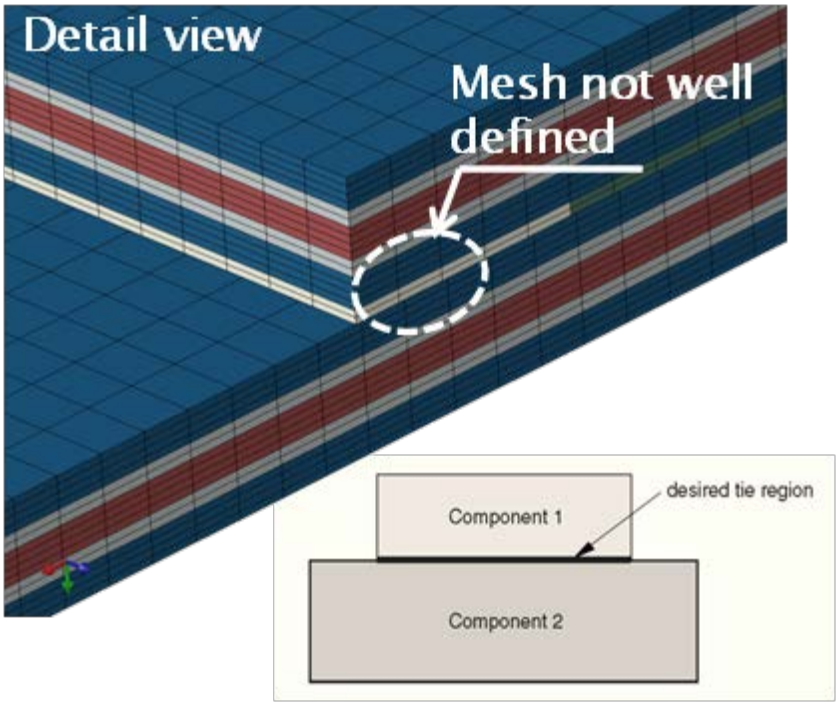

Figure 16 : Interaction between parts with tie constraints on the meshes.

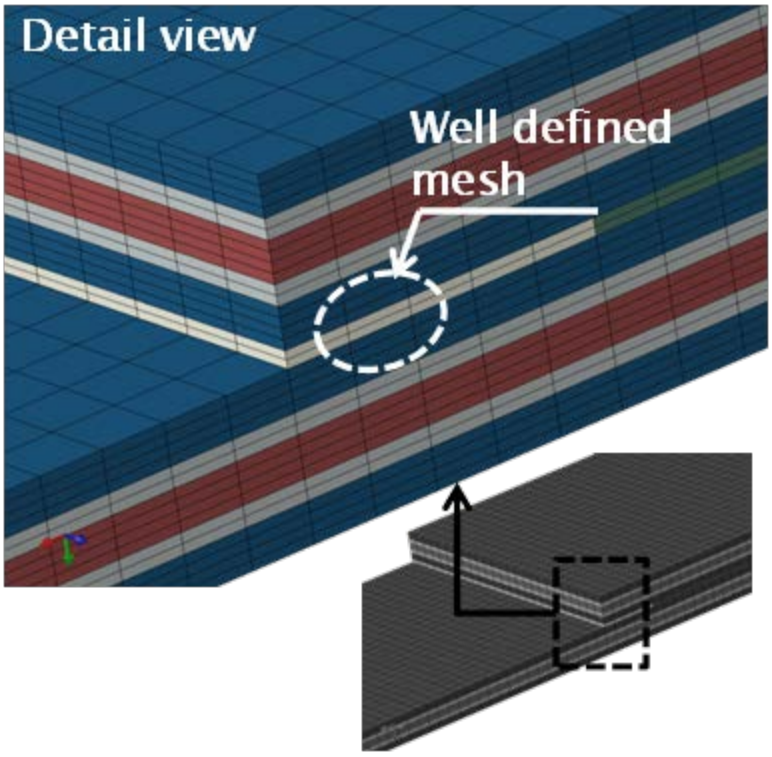

Figure 17 : Interaction between parts with the merged nodes in the meshes.

Figure 18 shows that the stress distribution in the thickness direction was not same in the outer ply and the inner ply. This means that the three dimensional modelling techniques used for analysis may not be accurate. However, Fig.19 shows that by using a composite shell to generate the section for this model, the outer and inner layers have the same values in the stress distribution. Therefore, this technique was chosen for the three dimensional modelling. The finite elements used in this case were the composite shell type to generate the section in each partition with continuum shell elements for the laminate and cohesive elements with maximum stress for damage progression in the adhesive region.

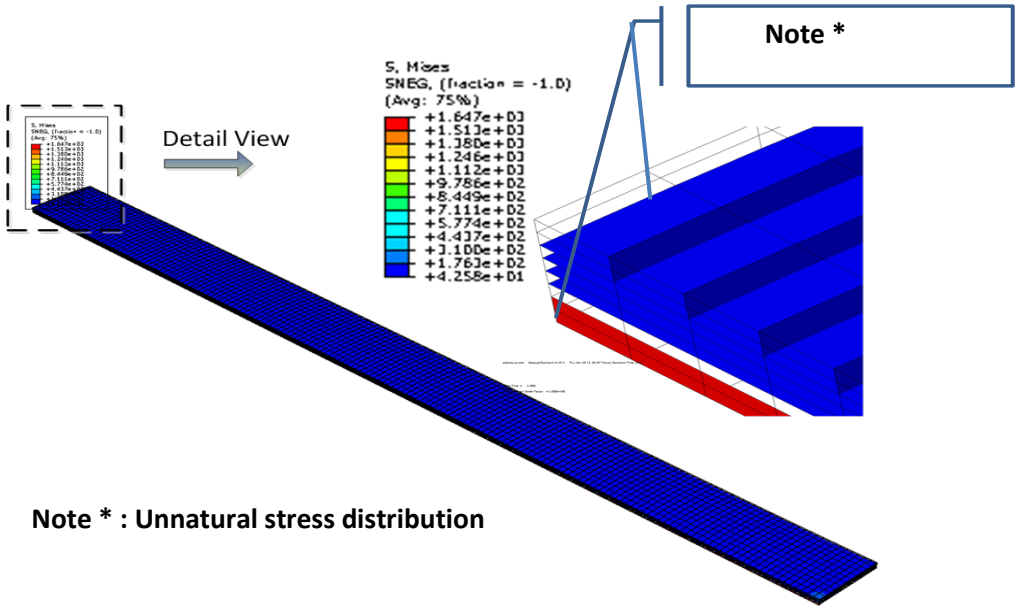

Figure 18 : Composite lay-up to generate the model section.

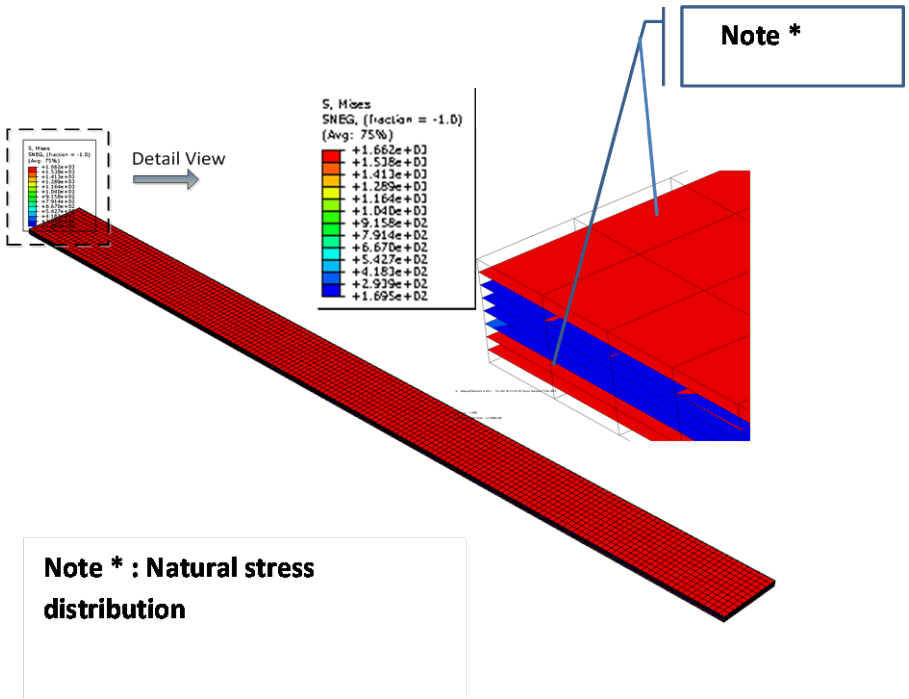

Figure 19 : Composite shell to generate the model section.

2.3.4. Numerical Result

A comparison of stress and loading distributions was made between the combined joint and the bonded joint only in thin composite structure with stiffness mismatch. The effect of adding the rivet in the joint was also demonstrated. Comparisons of the separation elements for the two joints are shown in several figures below.

In the bonded joint, we can observe in Fig.20 that separation occurs only at the edge of the stiffener until the specimen fails as a result of the peeling stress created by the secondary bending moment. This phenomenon is caused by a stress concentration at the edge region of the stiffener due to a stiffness mismatch and a change in the neutral-axis load. Figure 21 shows the existence of the peel stress emerged in the

simulation and can be observed in the maximum principle stress vector. This means that delamination will begin at the edge region of the stiffener and then grow toward the middle of the specimen.

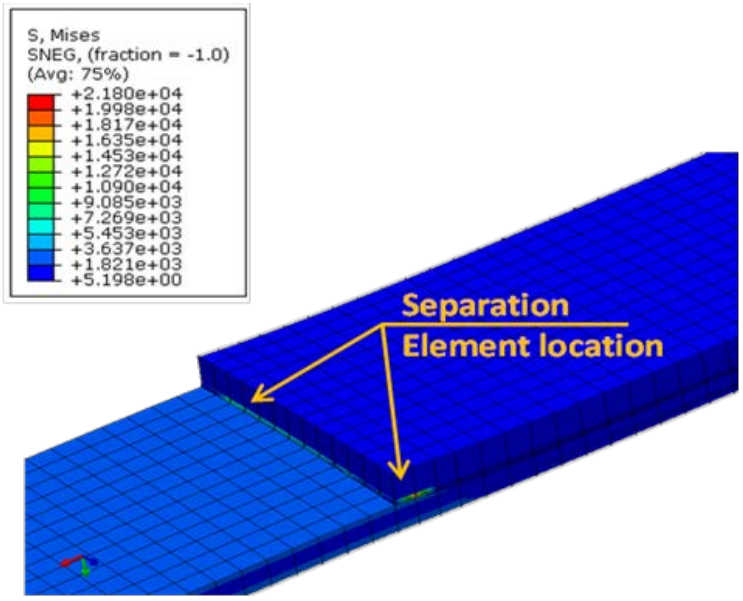

Figure 20 : Separation element locations under loading of the bonded joint.

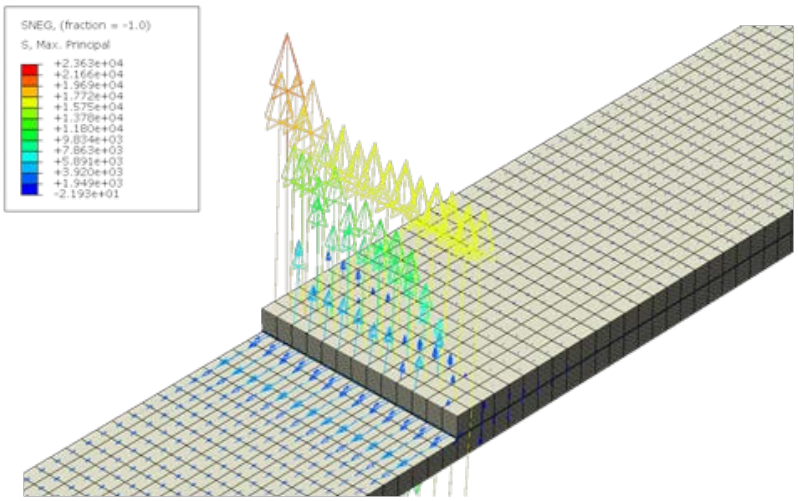

Figure 21 : Distribution of maximum principle stress vectors for the bonded joint.

Figure 22-23 show results of the combined joint, demonstrate a notably different separation pattern from those of the bonded joint: there are stress concentration areas at the edge of the stiffener and in the area around the rivet hole. This finding indicated that the addition of the rivet in this case produces a multi-area stress concentration effect. The stress concentration becomes highly critical, especially in the transverse direction because of its fairly large separation area.

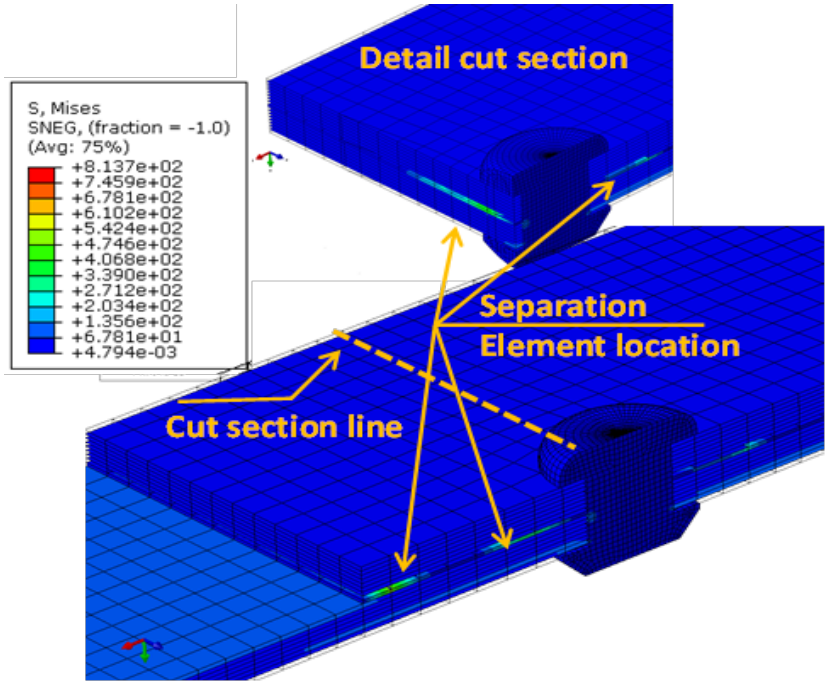

Figure 22 : Separation element locations under loading for riveted and bonded joint.

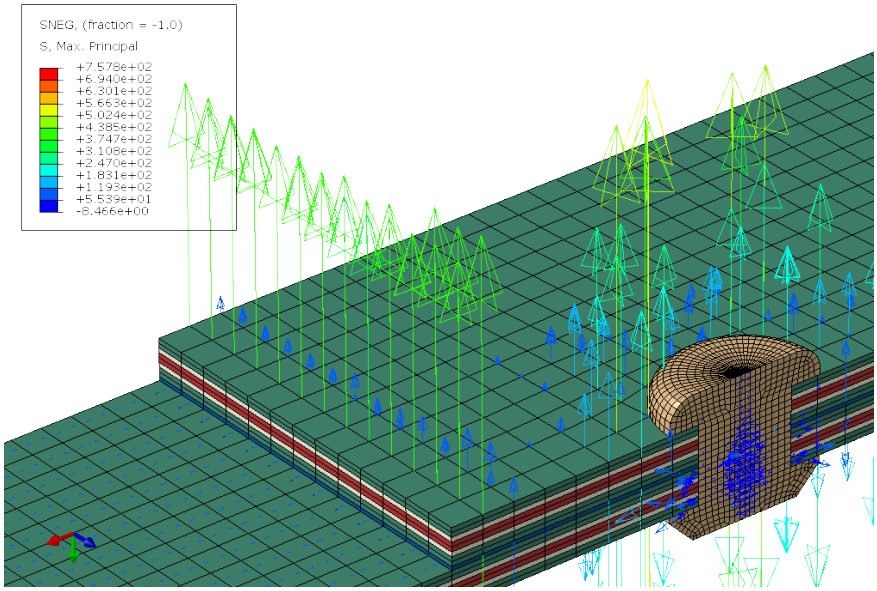

Figure 23 : Distribution of maximum principle stress vectors for riveted and bonded joint.

Figure 24 shows the peeling stress distribution profile in the longitudinal direction. This profile is consistent with the data shown in the previous figure that the combined joint has multiple areas of peeling stress concentration on the edge of the stiffener and the rivet holes, where the local stress concentrations dominate. In the case of the bonded joint, the peeling stress concentration occurs only at the edge of the stiffener as a result of the mismatched stiffness in that area.

Figure 25 shows the peeling stress distribution profile in the transverse direction. The stress concentration profile is different in the transverse direction: It occurs at only one point in the combined joint, around the rivet hole, whereas in the bonded joint the edge of the stiffener is the area with the highest stress.

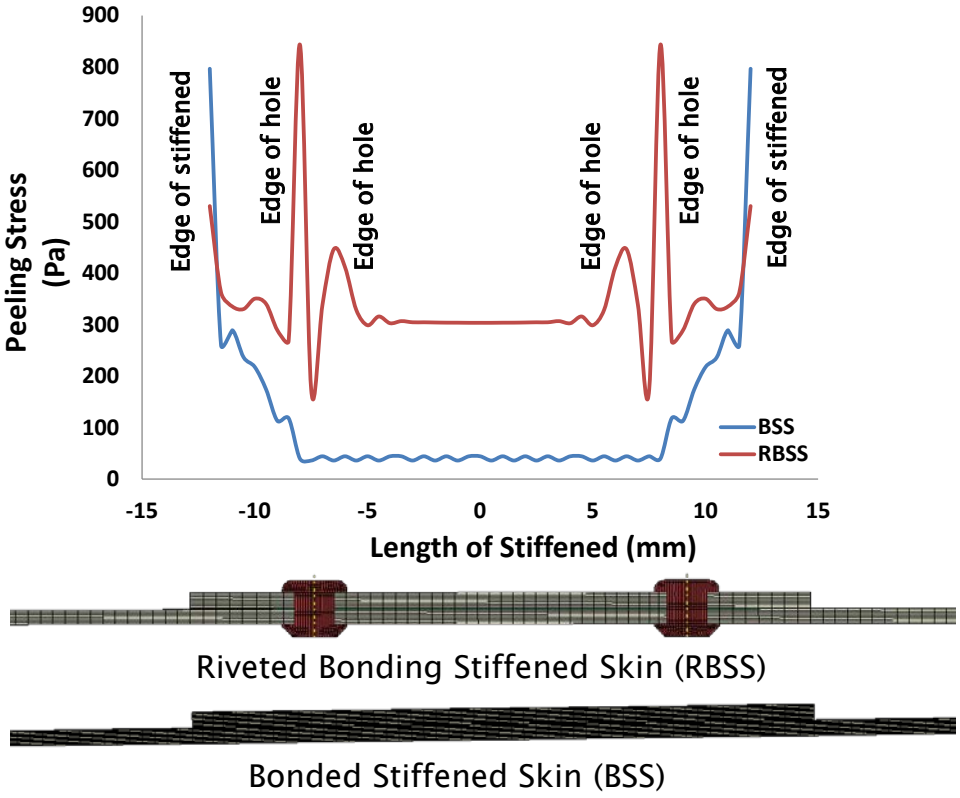

Figure 24 : Peeling stress comparison in longitudinal (loading) direction.

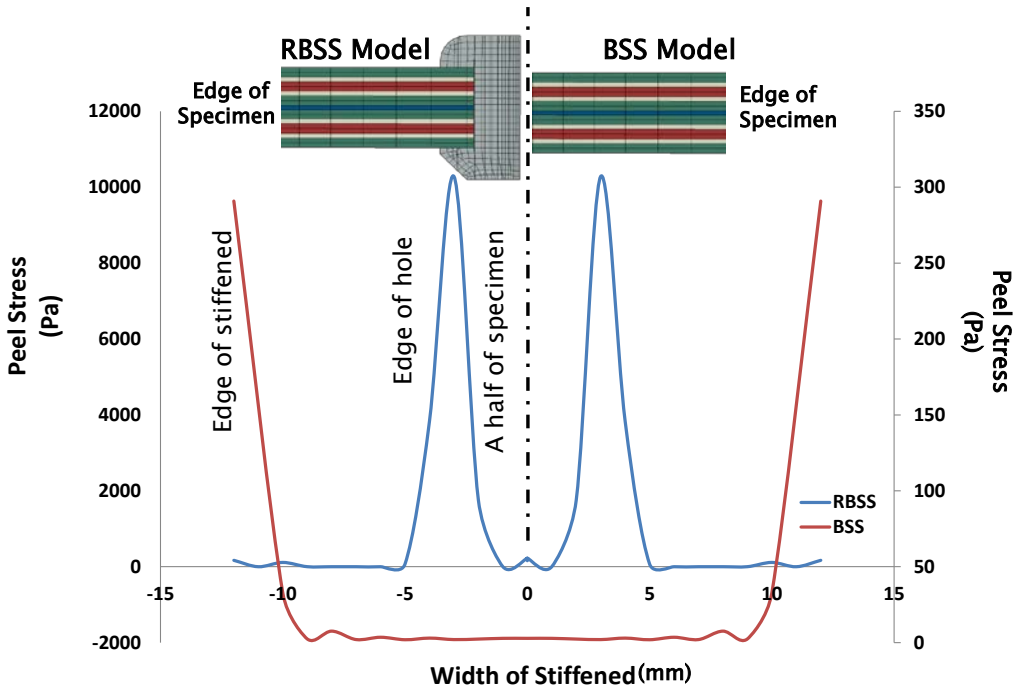

Figure 25 : Peeling stress comparison in transverse direction.

Figure 26 shows a comparison of the stress concentration in the area around the rivet hole in the transverse direction. In the combined joint, as a result of the addition of the rivets, the stress concentration increases significantly, reaching values 9 times greater than those of the bonded joint. While Fig.27 shows a comparison of the load transferred from the skin to the stiffener exhibits a large difference, approximately 179 times in the case of a bonded joint compared to the combined joint.

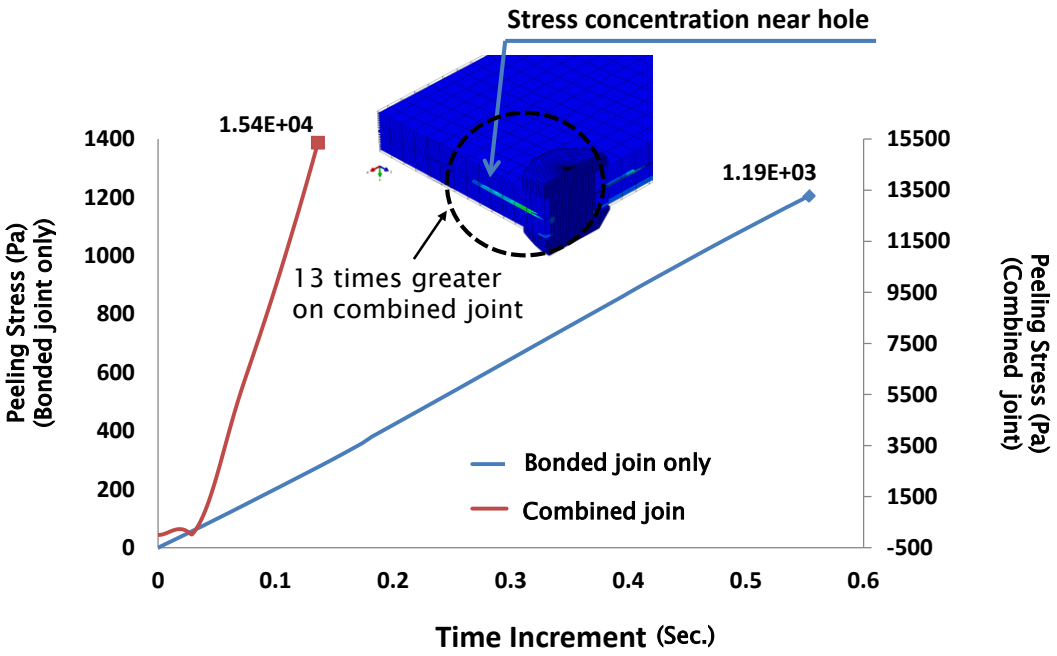

Figure 26 : Comparison of stress concentrations near the rivet hole.

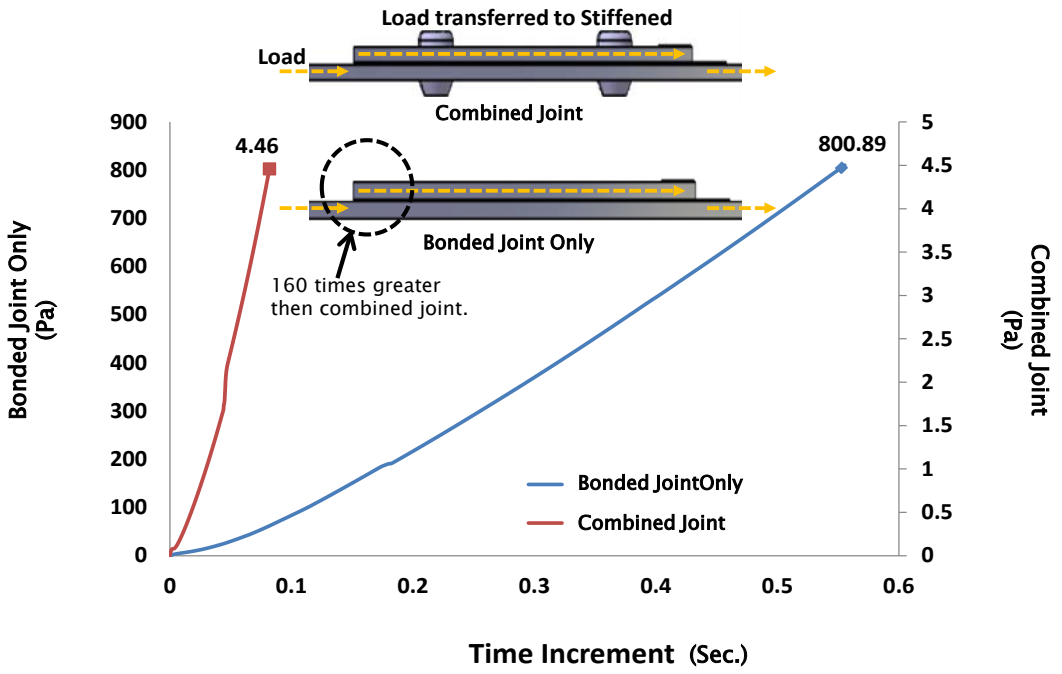

Figure 27 : Comparison of the load transferred to the stiffener.

Figures 28-29 show the differences in stress concentration at the interface between the stiffened and the skin under tensile and three-point-bending loads. In previous results, it can be verified that the onset of delamination will occur at the edge of stiffened and near the riveting hole under tensile loading. But under three-point bending, the load concentration appeared in the center of the specimen and near the riveting hole. No out-of-plane behavior is seen virtually because the element based used is a shell, and this type of structure cannot experience normal directional behavior except as shown by the vector stress response.

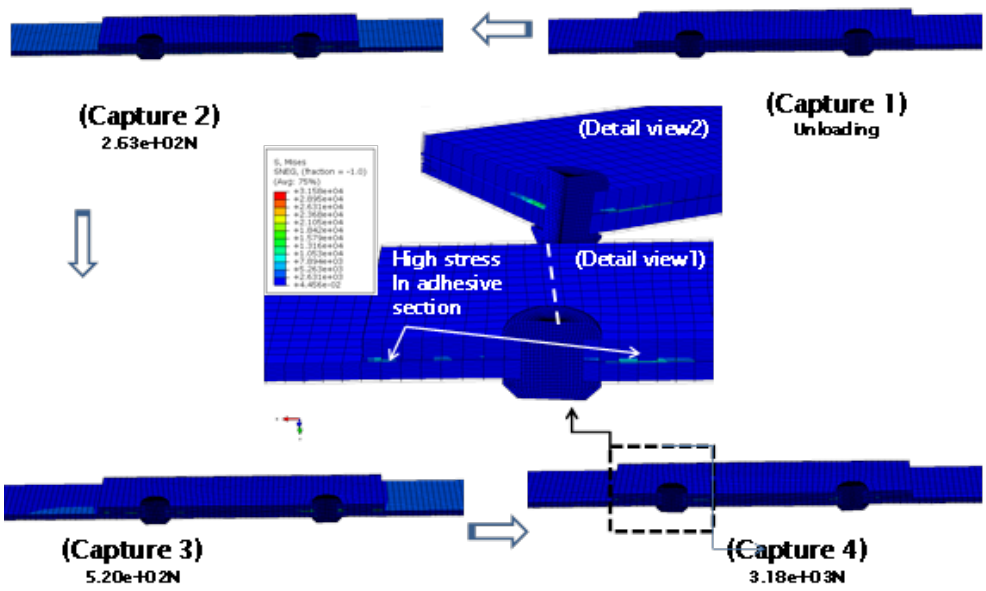

Figure 28 : Onset of delamination based on cohesive zone model theory in a tensile test. Capture 4 indicates when damage onset occurred in certain areas.

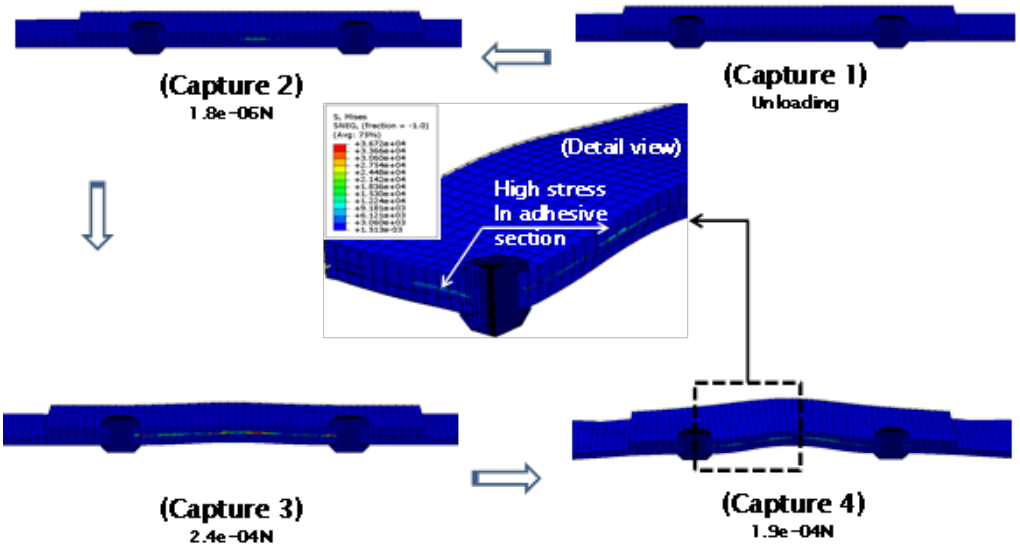

Figure 29 : Onset of delamination based on cohesive zone model theory in three-point-bending test. Capture 4 indicates when damage onset occurred in certain area.

Figure 30-31 show a comparison of the separation element and the stress distribution in the combined joint under tensile. We can see that separation initially occurs at the edge of stiffener as a result of the peeling stress created by the secondary bending moment. This effect occurs because of the stress concentration at the edge region of the stiffened due to a stiffness mismatch: the neutral-axis load was changed, and the load was shifted nearer to the hole rivet area when the load increased. The peel stress caused by the mismatched stiffness and load-shift can also be shown in that virtual figure by the maximum principle stress vector in the normal direction.

Figure 32-33 show a comparison of the separation element and the stress distribution in the combined joint under three-point loading. A different separation pattern appears where the stress distribution response is opposite from that under tensile loading. This pattern shows a significant stress concentration in the middle of the specimen that is load shifted to near the hole rivet area, and loading is increased. Indications are that the addition of the rivet in this case provides a multi-area stress concentration effect. The stress concentration becomes very critical especially in the transverse direction due to the fairly large separation in the area of the rivet. Both loading scenarios have principle differences regarding the stress distribution. However, the shear load is dominant in both specimen models. This outcome will influence the

FBG sensor spectrum perspective behavior which is explained in the next chapter. However, this shearing load response is less critical in the delamination process compared with the normal direction load response.

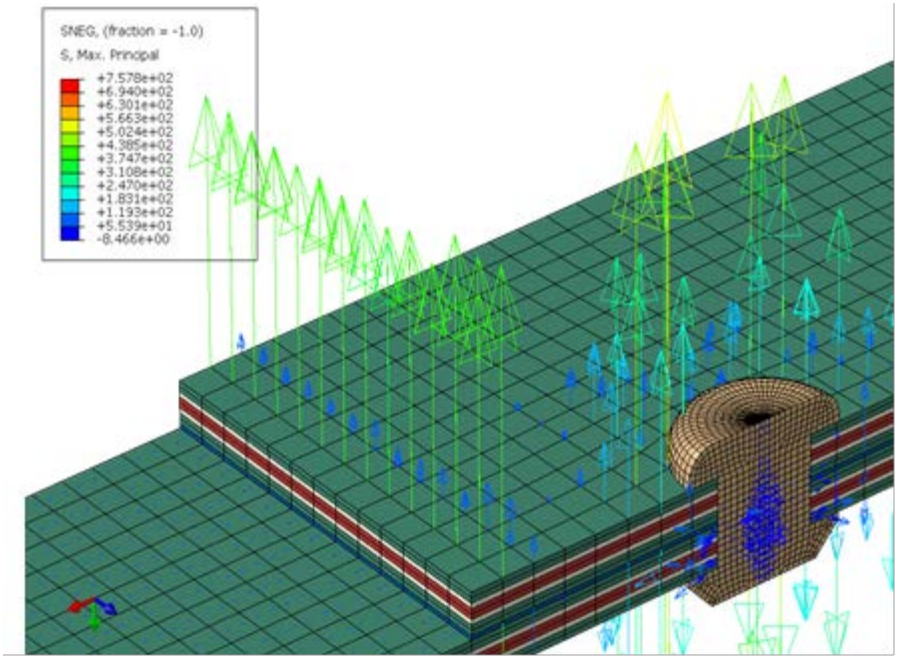

(a) First Load: 4.877E2 N

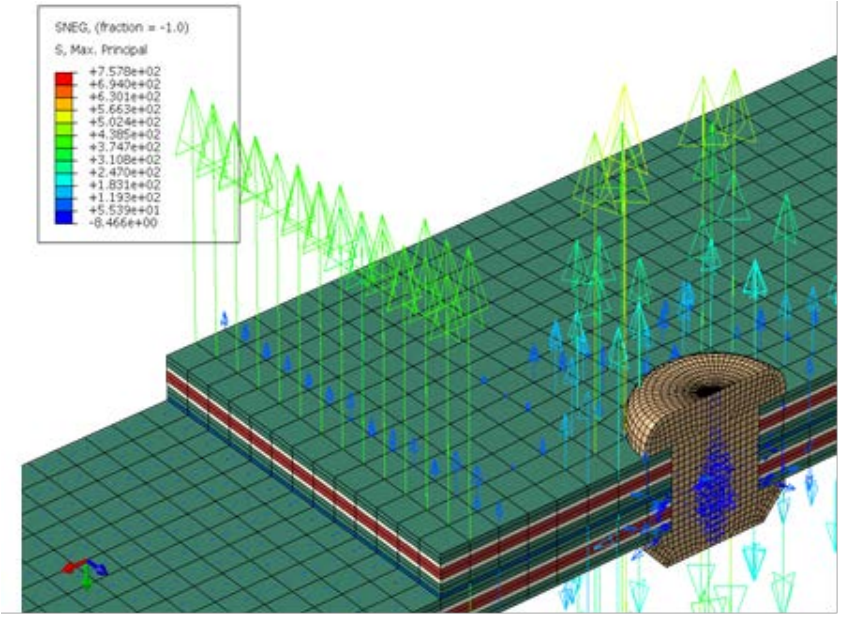

(b) Second Load: 4.526E3 N

Figure 30 (a) (b) : Distribution of principle stress maxima and vector directions under tensile loading for combined joint.

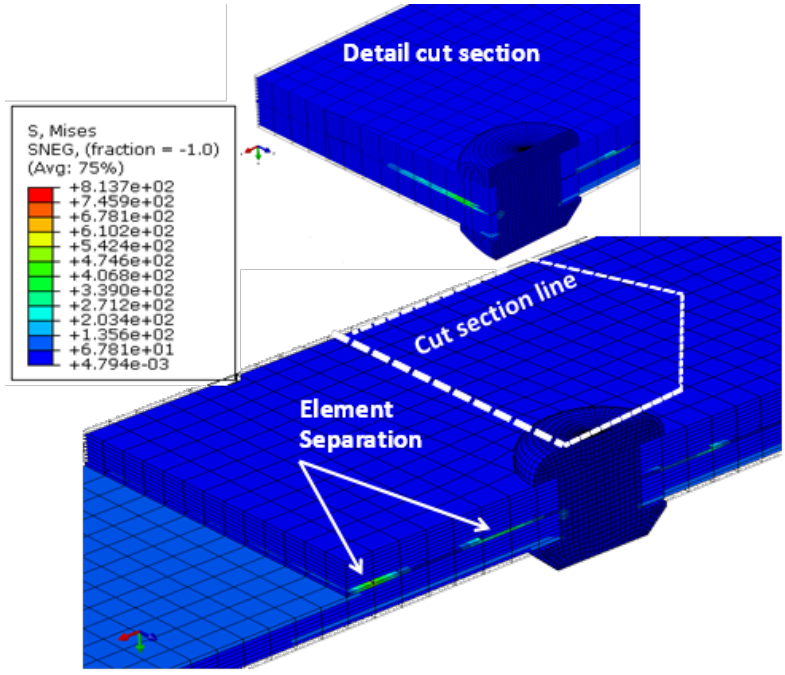

Figure 31 : Separation element location during tensile loading for combined joint.

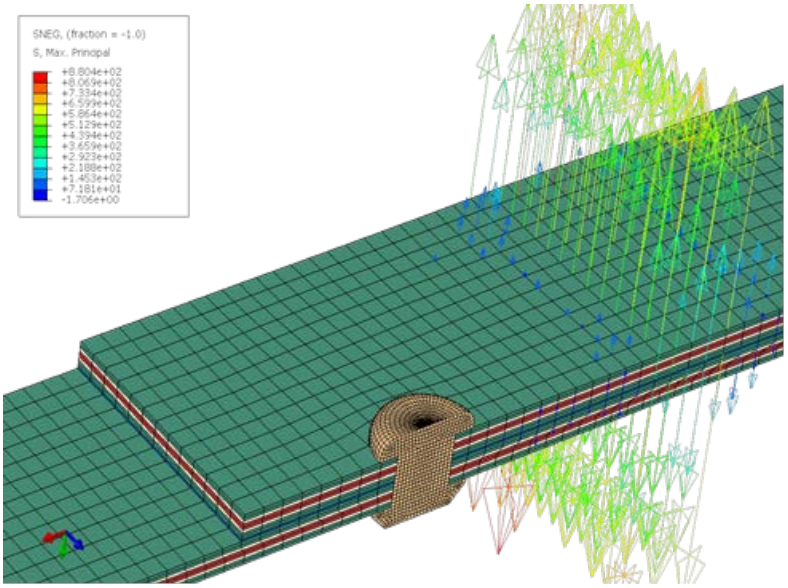

(a) First Load: 8.4E-04 N

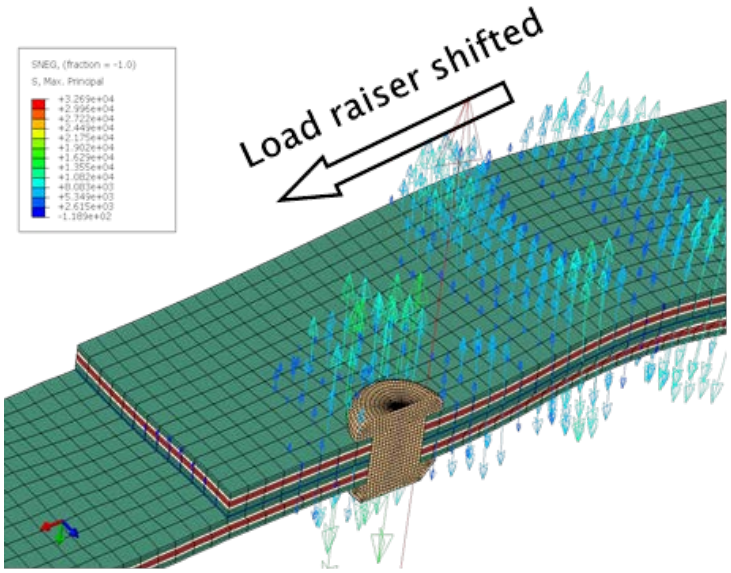

(a) Second Load: 1.3E-01 N

Figure 32 (a) (b) : Distribution of principle stress maxima and vector direction for combined joint under three-point loading.

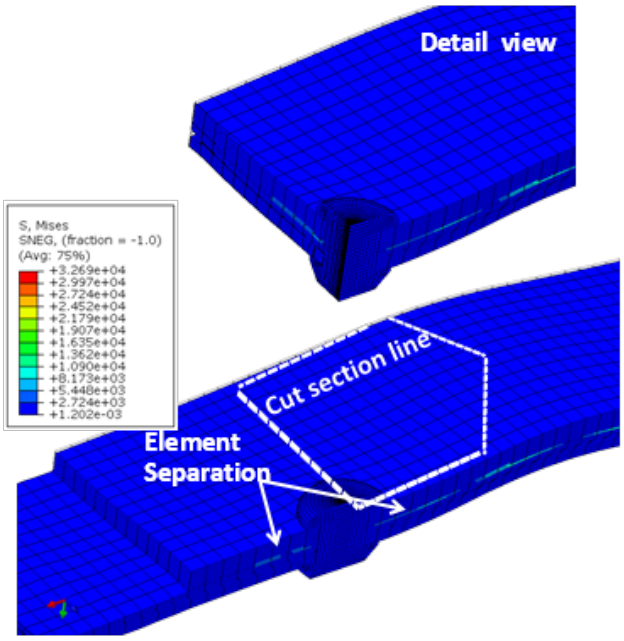

Figure 33 : Separation element location during three-point-bending loading for combined joint.

Figure 34 shows the stress distribution profile in the longitudinal direction under tensile loading for combined joint. This profile is consistent with the previous figure in that multiple areas of peeling stress concentrate on the edges of the stiffener and the rivet holes as local stress concentrations dominate. However, Fig.35 in the case of three-point bending loading for combined joint, no peeling stress concentration occurs at the edge of the stiffener as a result of the mismatched stiffness in the area. The stress is eliminated because the rivet increased the resistance to out-of-plane failure at the edge, although it also increased the risk of bearing failure due to the hole. The addition of the rivet indicated that the stress distribution can shift in the middle of the specimen.

Figures 36-37 show the stress distribution profile in the transverse direction combined joint. A comparison between the test scenarios under different loads indicates that both have nearly the same stress distribution profile in the transverse direction, which has no multi-area stress concentration caused by the addition of the rivet. The stress concentration occurs only around the rivet hole for both test scenarios.

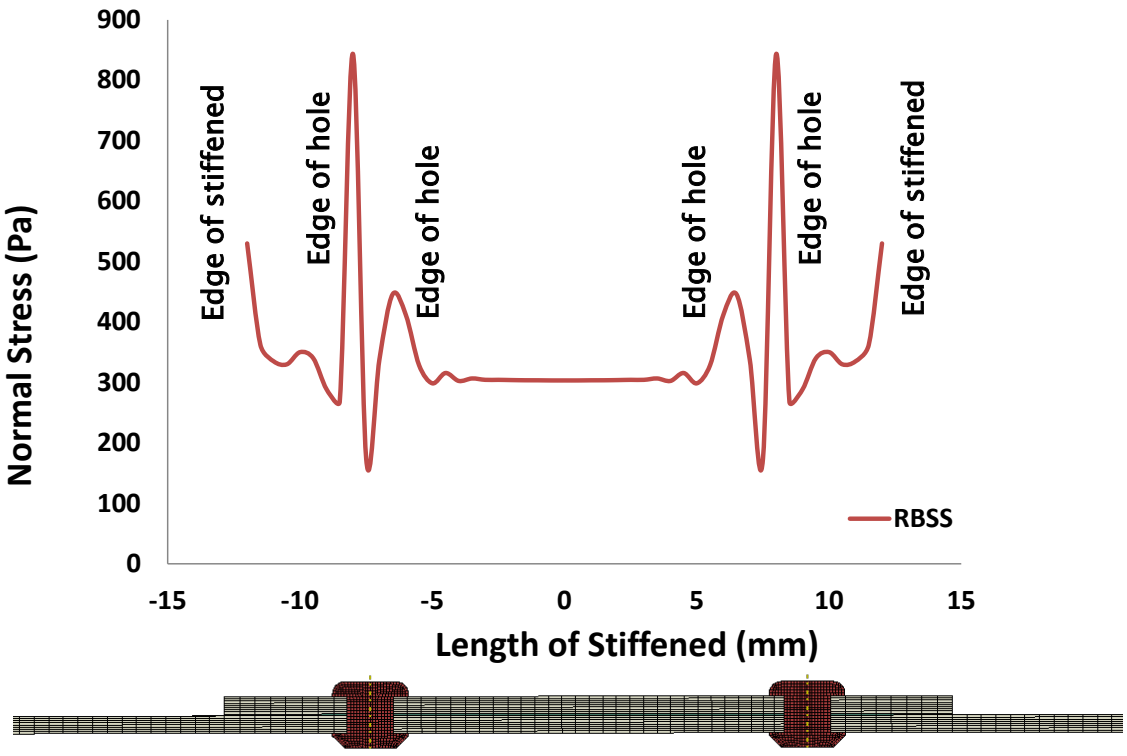

Figure 34 : Stress distribution profile in the longitudinal under tensile loading for combined joint.

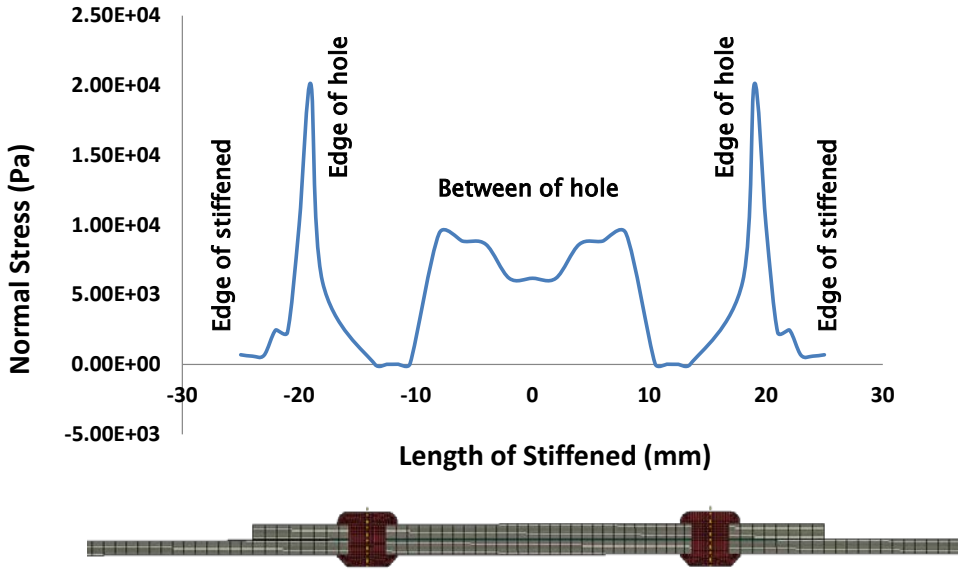

Figure 35 : Stress distribution profile in the longitudinal direction of the test under three-point-bending loading for combined joint.

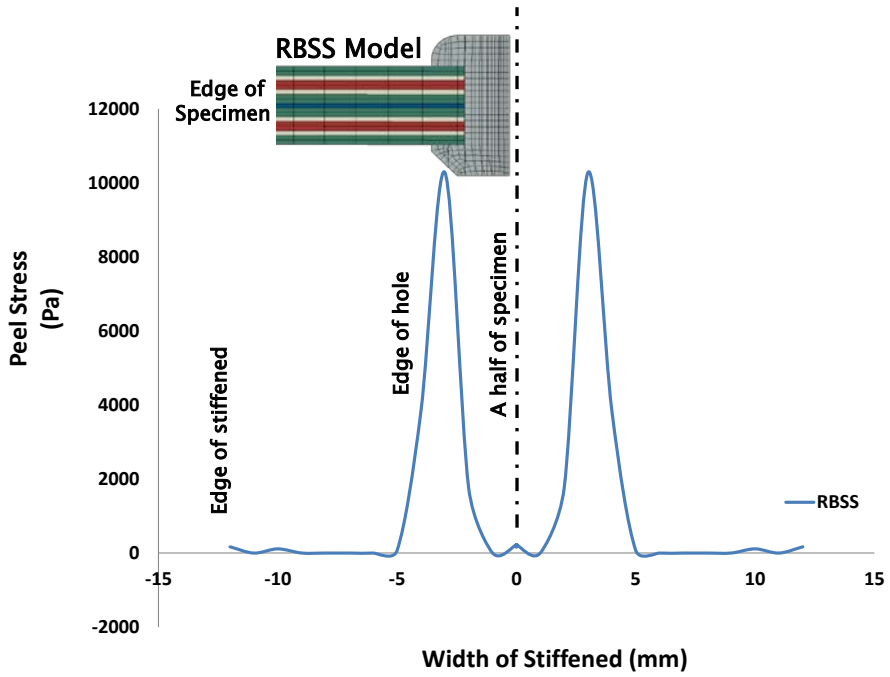

Figure 36 : Stress distribution profile in the transverse direction of the test under tensile loading for combined joint.

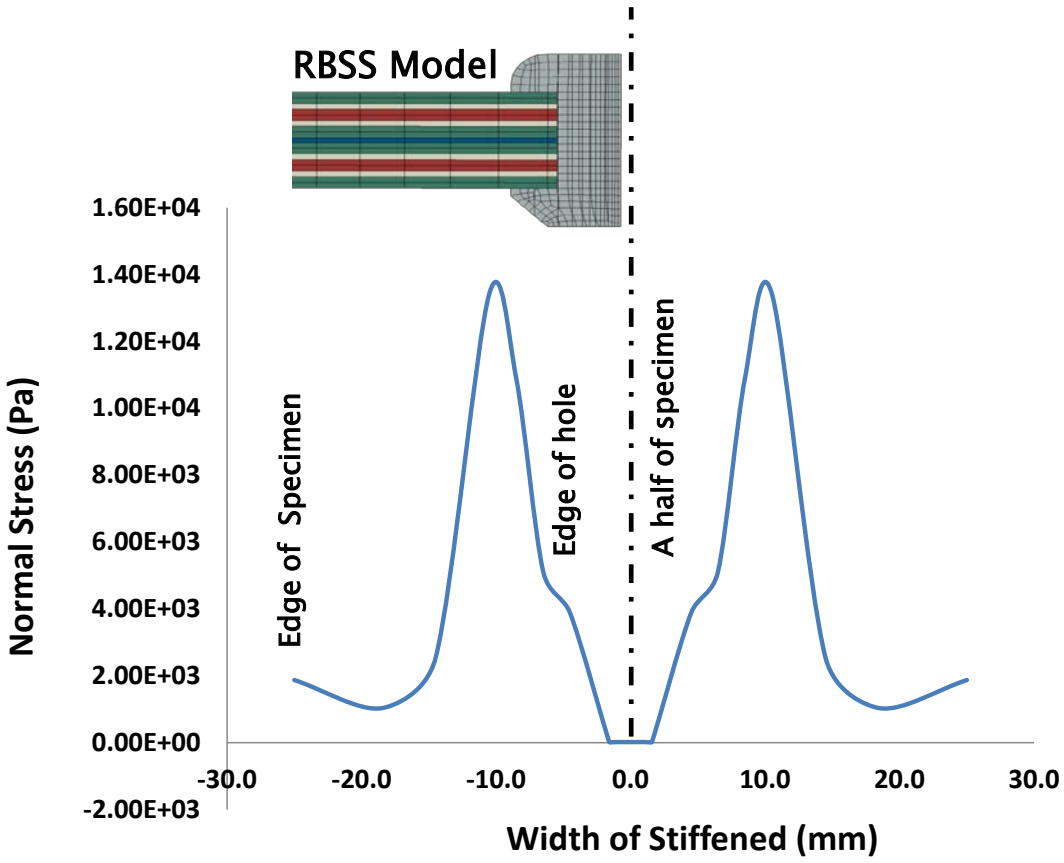

Figure 37 : Stress distribution profile in the transverse direction of the test under three-point-bending loading for combined joint.

Figure 38-39 show a comparison of the load transferred to the rivet area for the two test scenarios. Under tensile loading, all the load is transferred to the rivet area. As a consequence, nearly no load is transferred to the stiffener in this case, and the load accumulated in the hole rivet area. The situation is different in the test scenario under three-point loading in which it can be seen that the load is transferred partially to the rivet area. This means that the risk of bearing failure is also minimized.

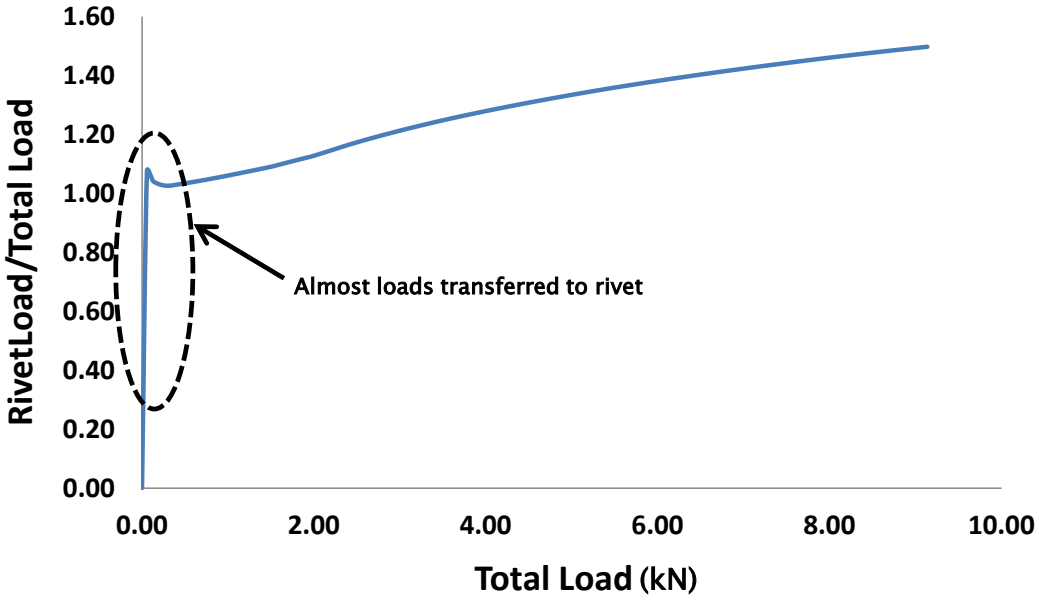

Figure 38 : Normalized load transfer in the rivet area under tensile loading.

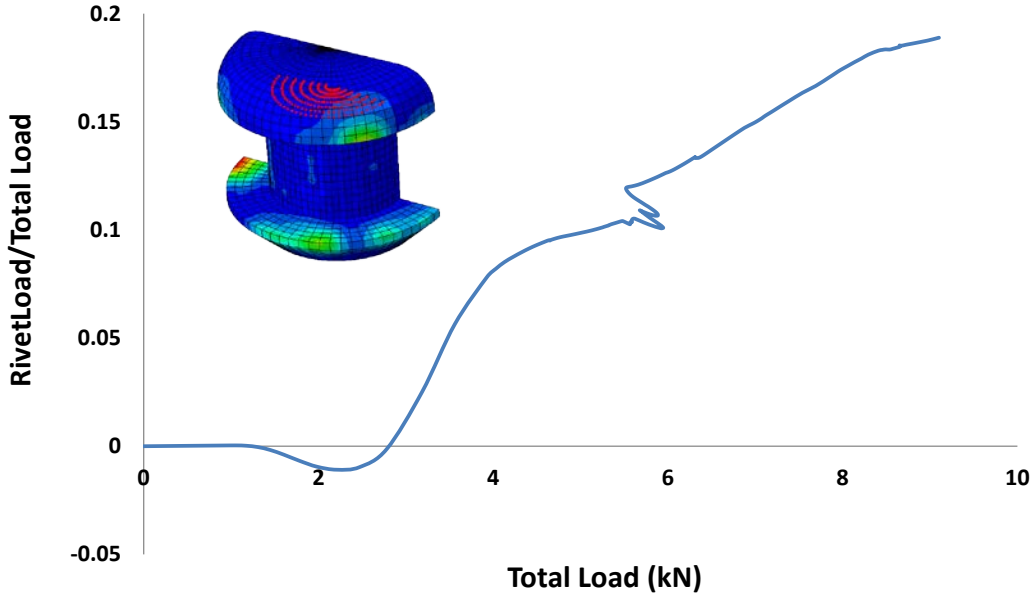

Figure 39 : Normalized load transfer in the rivet area under three-point-bending loading.

The analysis of a thin structure with a stiffness mismatch indicated that the damage initiation is prone to occur at the edge of the stiffener area and tends to create a delamination failure triggered by the occurrence of a peeling stress created by a change in the neutral axis. The addition of rivets to form the combined joint does not always increase the joint strength, but may actually decrease it because of a change of failure mode and location. The combination, however, has considerable benefits in the context of imperfectly bonded structures or in thick composite adherends.

Concluded here, FEM studies have verified and concluded that the mechanical behavior of the failure scenarios and the critical positions in which to place the FBG sensor as reference to build the specimen and then test it. The test will be conducted in two steps. First, the profile spectrum from zero loading until specimen breakage is determined to obtain the complete spectrum behavior based as continuous monitoring with FBG sensor. Then, an interrupted test is conducted to determine the loaded/unloaded spectrum and the growth of delamination. After the loaded/unloaded test, the specimen is evaluated using a C-scan machine to catch an image of delamination growth and used it to quantify the damage.

2.4. Specimen Fabrication.

Analysis alone is generally not considered adequate for substantiation of composite structural design. It is generally recognized that numerical analysis is supplemental to design of composite structures. However, it should always be used in conjunction with a rigorous test program. The purpose of the experiments was to measure the distribution of the strain on the specimen and subsequently use the results as a validation of the finite element analysis. The parameters of the finite element analysis used in the study were verified through a comparison with the experimental results. The experimental setup included strain gages, an advanced video extensometer (AVE), and a C-scan inspection to quantify the delamination as it occurred. The strain gages used were KFG-5-120-C1-11L10M3R, single-direction gages fabricated by Kyowa, and a GNES Corporation 6AX600RS ultrasonic scanner was used for the C-scan.

2.4.1. Pre-impregnated Lay-up Preparation

Figure 40 shows the curing circle of IMS60/#133 whereby the resin within the prepreg changes from a liquid to a solid through the application of heat. A prepreg consists of a reinforcement material preimpregnated with a resin matrix in controlled quantities. The resin is partially cured to a B-stage, and in this form is supplied to the

fabricator, who lays up the finished part and completes the cure with heat and pressure. The required heat and pressure will vary with the resin system and the intended application. There are a number of stages in this cycle:

Curing Temperature and Time : For each prepreg resin system there is a range of options for cure temperature. For a given cure temperature there will be a corresponding cure time. The autoclave, laminate, and tooling should all reach and maintain the given cure temperature throughout the specified cure cycle. Thermocouples are used to monitor the temperature.

Heat Up Rate : The heat up rate is a measure of how quickly the laminate is brought up to the cure temperature. For highly reactive matrices and thick laminates the heat up rate will be low, and may incorporate an intermediate temperature soak, in order to avoid exothermic reactions.

Cooling Rate : The cooling rate is controlled in order to avoid sudden temperature drops that may induce thermal stresses in the component.

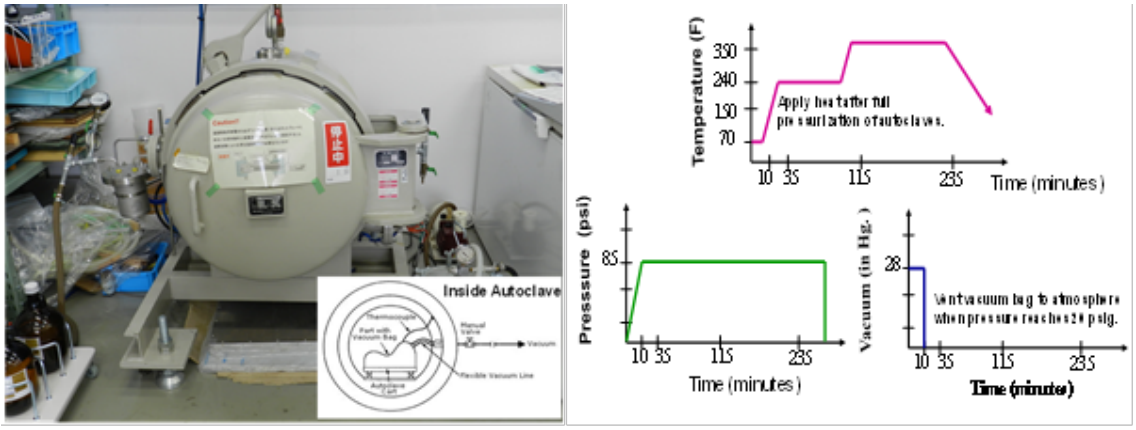

Figure 40 : Autoclave system and curing circle process for impregnated laminate.

2.4.2. Bonding Process and FBG Sensor Installation

Two component low viscosity epoxies are used to join the specimen model called the Epoxy Adhesive DP-420 Off-white; Part A and Part B. Preparation of the adhesive is a critical step in the bonding procedure. Inaccuracy during the mixing process can be the single contributing factor to bond failure. All steps must be taken to ensure that the adhesive is prepared according to manufacturer specifications. And abrading surface will help the adhesive to form a better bond with the surface. A general rule is not to abrade the surface more than 0.1 microns. This will trap air bubbles in the bond which will lessen the bonding surface.

Figure 41 shows bond-line thickness category. Before applying adhesive to surfaces it is important to check the alignment to ensure the bond line thickness.

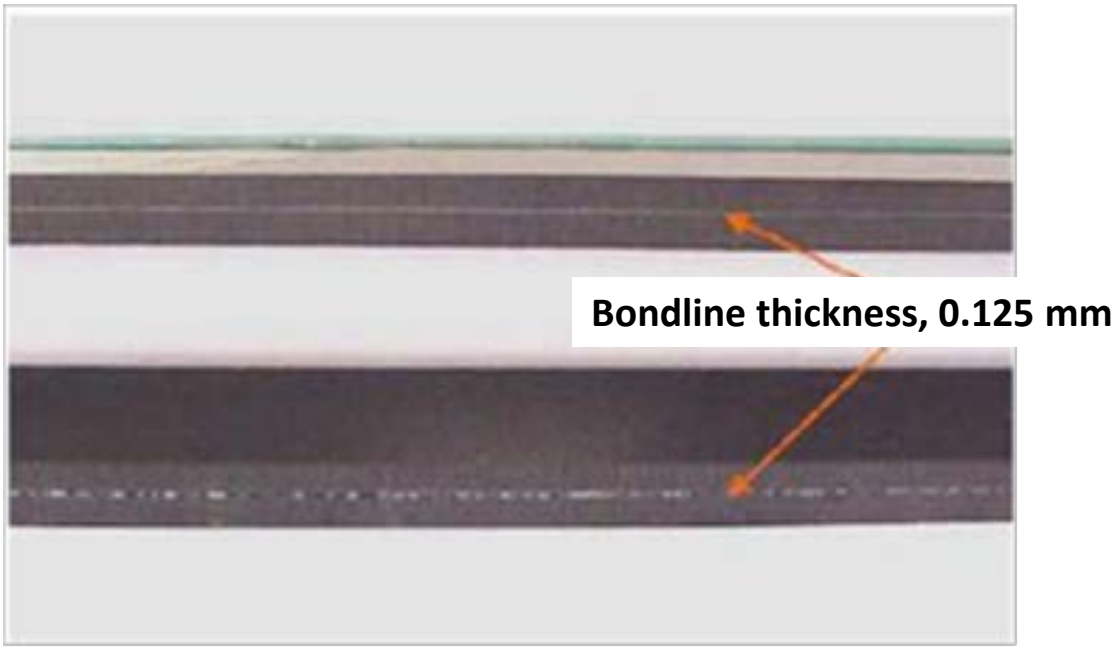

Figure 41 : Top is a good bond-line and bottom is a bad bond line.

Figure 42 shows preparation of adhesive used by gun-mixer and fixing. The adhesive shall be applied to both faying surfaces. The adhesive thickness shall be the same thickness with FBG sensor diameter. It is around 0.125 mm. Care shall be taken in assembling parts to assure that the adhesive is not disturbed during the cure period. For this activity, the interface between the composite skin and the stiffener was bonded using the adhesive DP420 Off-White from 3M with a double-stage bonding method. And the FBG sensor was embedded in the interface between the skin and the stiffener near the edge of the specimen as mentioned on numerical analysis result because this area has the greatest potential for failure.

Figure 42 : Adhesive gun-mixer system and specimen pre-fit.

2.4.3. Drilling Process

Figure 43 shows drilling rivet holes as follows the procedure stated in the MIL-R4796 for rivet application and installation. Drilling rivet holes should be drilled in accordance with the following recommendations;

- All holes shall be drilled normal to the working surface.
- Extreme pressure shall not be applied and holes shall not be punched through with the drill.

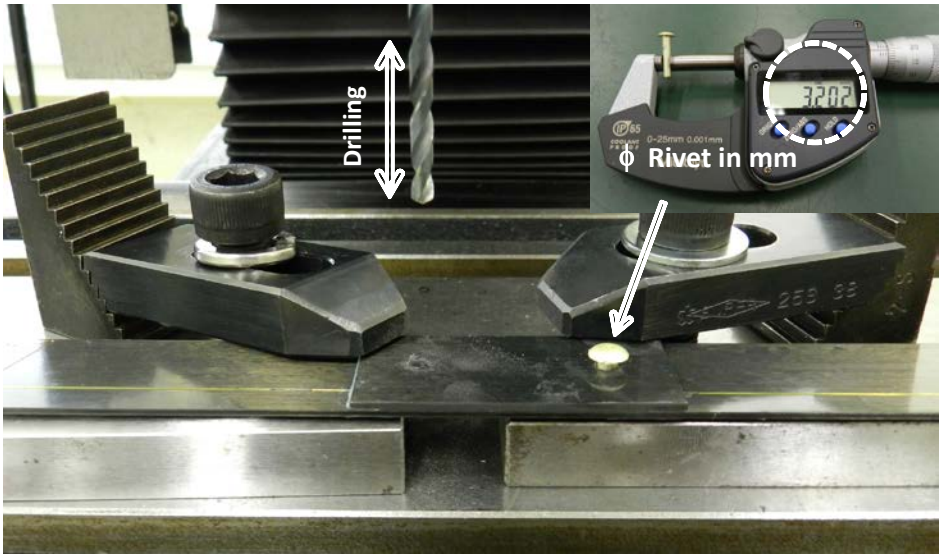

Figure 43 : Drilling process.

Figure 44-45 show pre-fit preparation to get ideal rivet head shape and rivet installation equipment. Mating surface should be cleaned before parts are riveted together. All chips, burr and foreign material must be removed from the mating surfaces. The formed head at the back of the rivet should be flat and round, and it should have a diameter 50-percent larger than the shank diameter with a thickness of one half of the shank diameter to get the ideal rivet head shape.

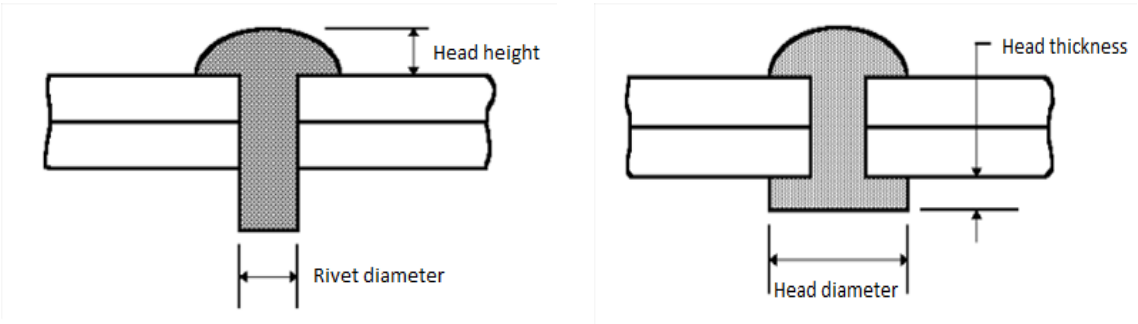

Figure 44 : (a) Rivet pre-fit preparation, (b) After rivet squeezing.

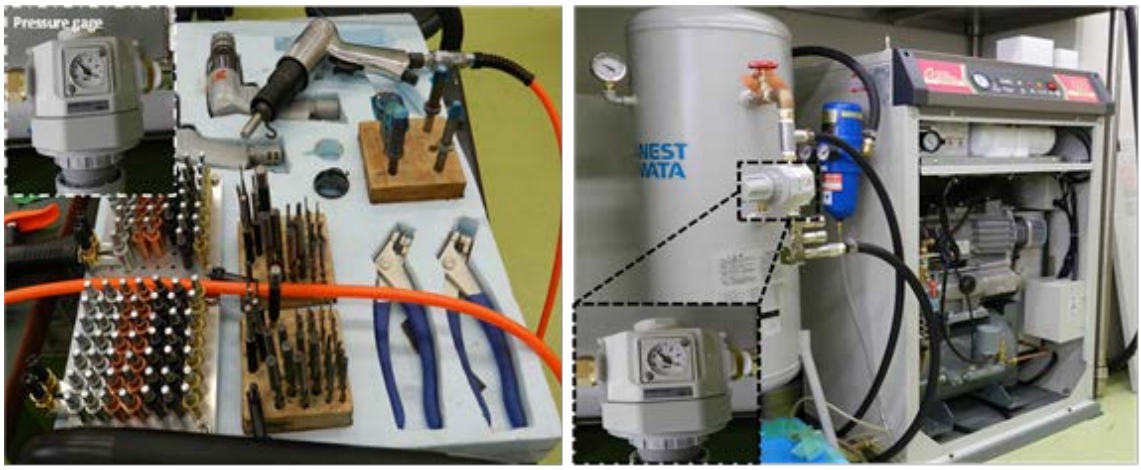

Figure 45 : Rivet assembles equipment and the compressor system for rivet gun.

2.4.4. Strain Gauge Installation

Figure 46 shows the strain gauge installation. The surface of the test piece has to be prepared prior to installation. The primary function of the preparation process is to create a clean surface free of grease, dust and other particulates that could interfere with the quality of the bond. Laminate can be affected by some solvents, so they should be cleaned with water and a mild surfactant, then dried with a clean cloth. Installed the strain

gauge onto a certain surface of specimen model using a cyanoacrylate adhesive. The adhesive is quick-drying and forms a stiff bond that transfers the strain with minimal loss of the test piece to the strain gauge. To facilitate the installation process, use a piece of clear tape to pick up the strain gauge. Position the tape containing the gauge onto the surface of specimen, then peel one end of the tape back to expose the back side of the gauge. Apply a drop of cyanoacrylate adhesive to the back of the gauge, then quickly push the tape back onto the surface specimen model. Apply soft pressure across the entire gauge surface for about one minute. Leave the tape on the gauge for at least 10 to 15 minutes.

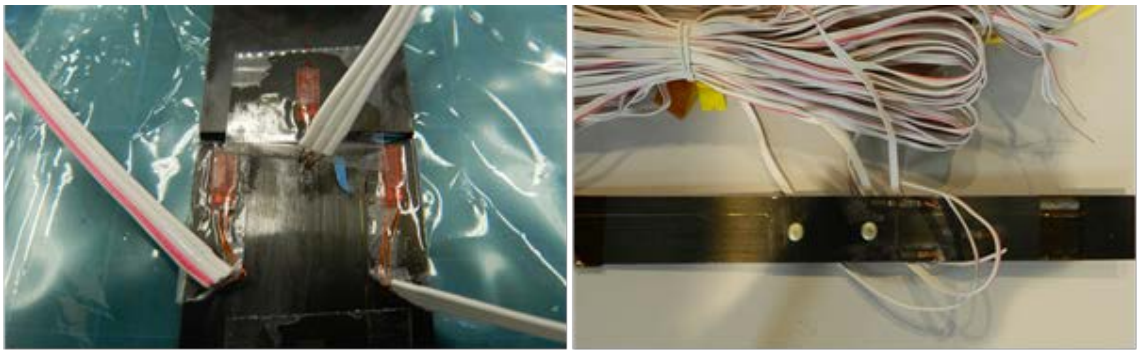

Figure 46 : Strain gage bondable process for combining joint and bonded join only specimen.

2.5. Experimental Procedure.

Test results in an empirical determination from a small and relatively simple specimen are often used as input to a simulation of larger and more complicated

structure. While the basic physics of test methods for composites may be similar to their un-reinforced counterparts. The heterogeneity, moisture sensitivity and low ductility of composite materials often lead to significant differences in testing requirements, particularly with the mechanical tests, including:

- The strong influence of the constituent content of material response, creating a need to measure the material response of every specimen,
- A need to evaluate properties in multiple directions,
- A need to condition specimens to quantify and control moisture absorption and desorption, increased importance of specimen alignment and load introduction method, and
- A need to assume the consistency of failure modes.

However, the above factors tend to increase the sensitivity of composite material to a wider variety of testing parameters. Therefore test method robustness, or relative insensitivity to minor variations in specimen and test procedure, is just as important as theoretical perfection. Robustness, or lack thereof, are assessed by laboratory testing, and is measured by precision (variation in the sample population) and bias (variance of the sample mean from the true average). The obvious ideal is a high precision (low variation) and low bias (sample mean close to true average) both within-laboratory and

between laboratories.

For heterogeneous materials, physically larger specimens can be expected to contain within the coupon specimen a more representative sample of the material microstructure. While desirable, a larger specimen is more contain a greater number of micro- or macro-structural defects than a smaller specimen, and thus can be expected to produce lower strengths. Variations in specimen geometry can also create differing results. Size and geometry effects can produce statistical differences in results independent of the "degree of perfection" of the remaining aspects of a test method. Therefore, even though the specimen response may not be identical to that of the structure, the "ideal" test method will incorporate a specimen geometry that can be consistently correlated with structural response.

2.5.1. Tensile test

Figure 47 shows the tensile test setup which it was fully computer controlled, which allowed for the acquisition of the load, the displacement and the strain data. The tensile test measures the force required to strained a specimen under tensile loading as explained in test standard ASTM D638. In this test, the gripped area has the same cross-section with the gauge area in span length where failure or large deformation be

expected as long span area. This type of machine (Instron 8802) has two crossheads; one adjusts for the length of the specimen and the other is driven to apply tensile to the test specimen. Before the test, force capacity set to 100kN with the speed of crosshead movement in 1 mm/mm for profiling test and 0.5 mm/mm for interruted test, while data acquisition retrieving by Bluehill software. It is adjusted before load running. Alignment of the test specimen in the testing machine is critical, because if the specimen is misaligned, either at an angle or offset to one side, the machine will exert a bending force on the specimen. The strain measurements are measured by strain gage attached to surface of the specimen, Advanced Visual Extensometer (AVE) and by Instron machine itself. When the strain value exhibited a sharp spike, the test was immediately stopped.

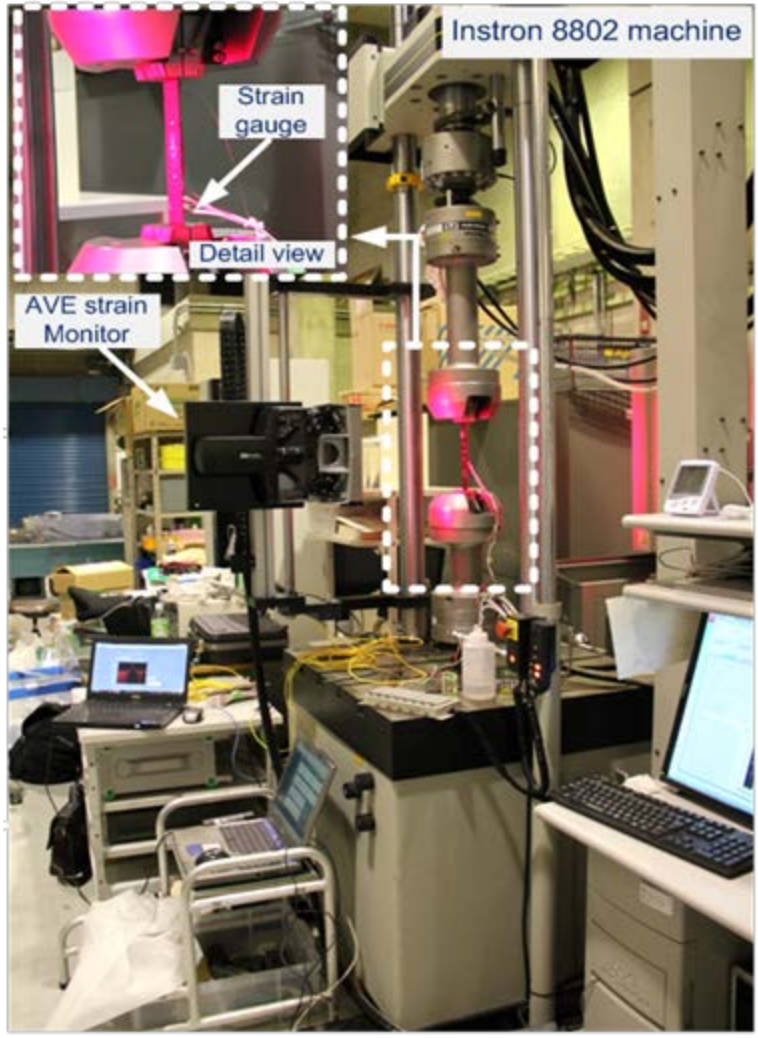

Figure 47 : Tensile test setup.

2.5.2. Three-point loading test

Figure 48 shows the flexural test measures the force required to bend a specimen under three point loading conditions as explained in test standard ASTM D790. Flexural modulus is used as an indication of a material's stiffness when flexed. The specimen lies on a support span and the load is applied to the center of the loading nose producing three point bending at a specified rate. The parameters for this test are the support span,

the speed of the loading, and the maximum deflection of the test with Instron 4505. For ASTM D790, the test is stopped when the specimen breaks. For ISO 178, the test is stopped when the specimen breaks. If the specimen does not break, the test is continued as far a possible.

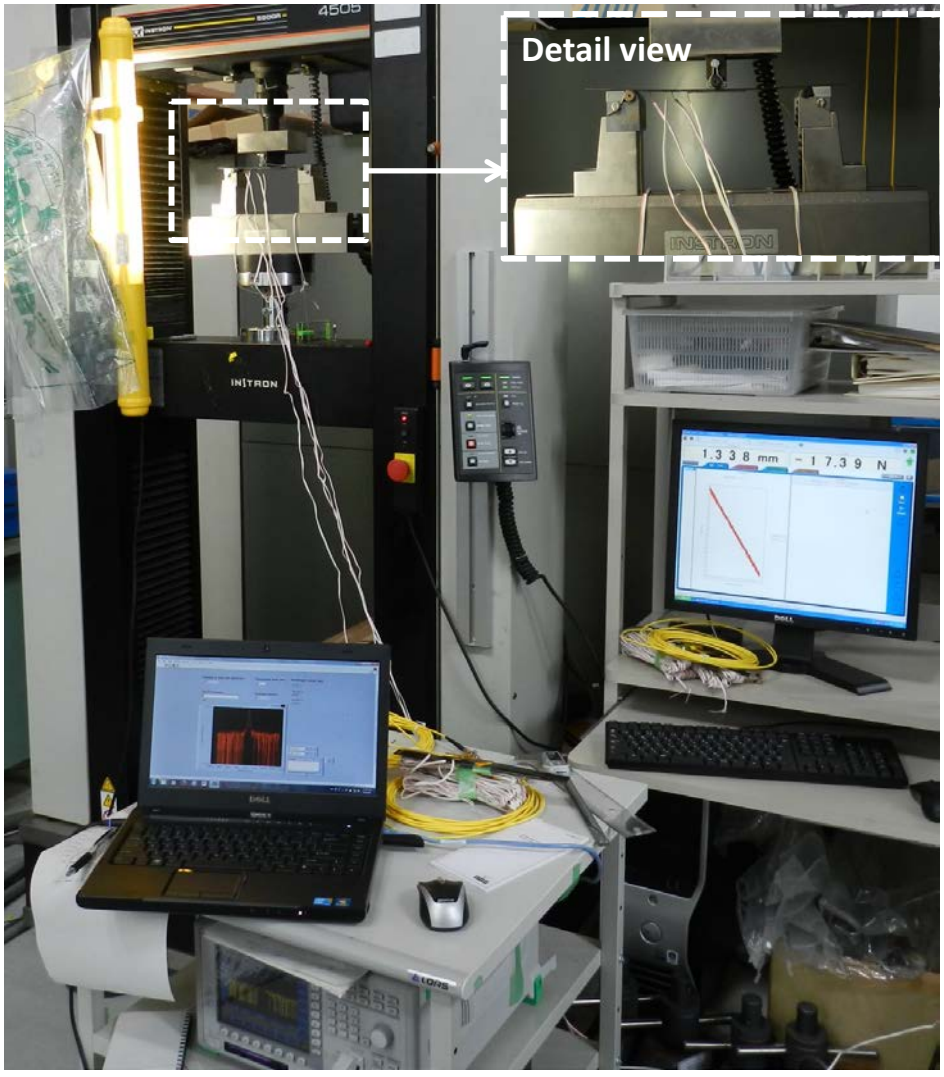

Figure 48 : Flexural test setup.

2.5.3. Bondable strain gauge test

Strain gages are structures of precisely etched metal foil or wire (usually on a

Polyimide film substrate) which are permanently bonded to a specimen surface so that the strain field of that surface is immediately transmitted to the gage.

Careful evaluation of surface preparation and bonding techniques for strain gages must be done if reliable data are to be obtained. Extreme care should be used when abrading composites to minimize damage to the fibers of the surface laminae. It should be noted that the bonding of strain gages of thermoplastic materials is especially difficult.

Strain conditioner linearity (calibration) is verified by the use of strain simulation. With 350Ω taken as the balance point or zero, strain values can be simulated by using a high accuracy decade resistance box with ranges from 0.01Ω to 100Ω in place of the active gage, and using the following equation to simulate strain values:

$$\Omega = 0.0007\varepsilon_{sim}+350$$

Where

Ω = decade resistance box setting to simulate the target strain (ohms)

ε_{sim} = target strain to be simulated (microstrain)

When fixed excitation conditioners have been verified in this way and found acceptable, no further calibration is necessary before testing. The output of the conditioner is simply multiplied by 2/K, where K is the gage factor reported by the gage manufacturer.

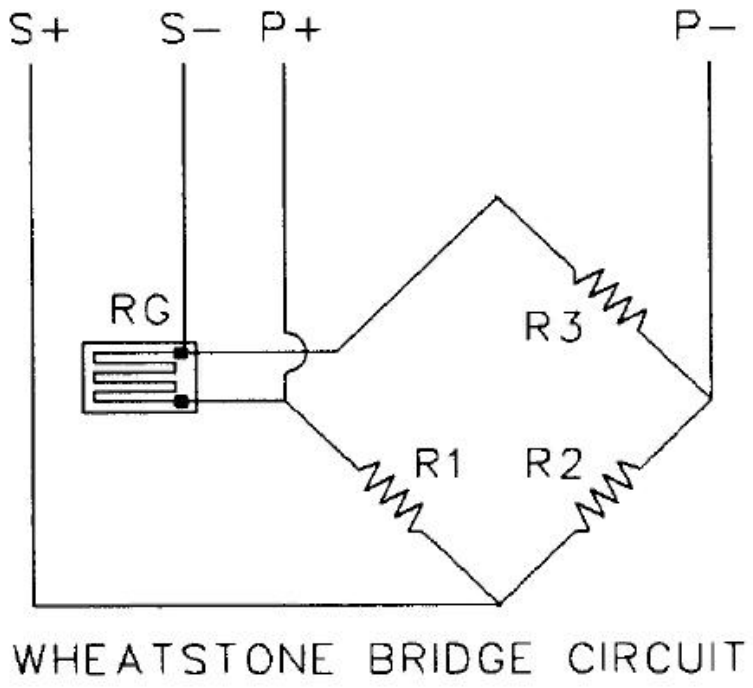

Figure 49 : Wheatstone Bridge Circuit.

2.5.4. Ultrasonic C-scan test

Figure 50 shows the illustration how the machine detects delamination within the specimen. Defects are defined as any deviation from the nominal, ideal or specified geometric and/or physical make-up of a structure or component. Delamination is a defect type frequently met in composite materials, described as the separation of a layer or group of layers, due to failure of the internal bonding between the layers. It can occur either during the curing phase of the resin in the manufacturing stage or during the subsequent service life of the laminated part or or the bonded structure parts.

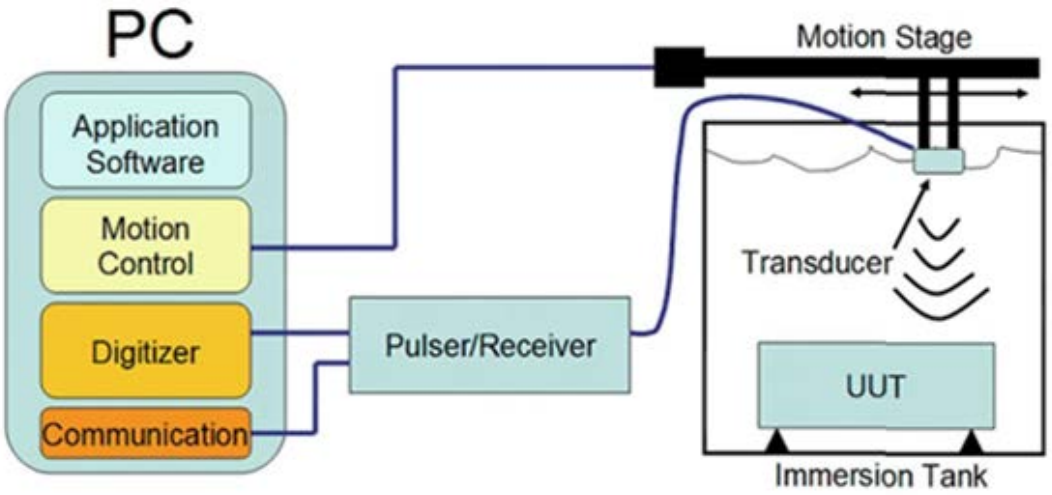

Figure 50 : The ultrasonic system illustration.

The pulse-echo method, which is the most widely used ultrasonic methods, involves the detection of echoes produced when an ultrasonic pulse is reflected from discontinuity of a test specimen. C-scan display record echoes from the internal portions of test specimen as a function of the position of each reflecting interface within an area. Flaws are shown on a read-out, superimposed on a plan view of the test specimen and both flaw sizes (flaw area) and position within the plan view can be recorded.

Figure 51 shows the transducer used in C-scan device manufactured by Gsonic Scan 6A x 600 to generate a short pulse-echo with flat transducer of 5 MHz then analyses the reflected sound pulse. The inspection is made with the specimen immersed in the water. The transducer is mounted on a multi-axis manipulator then travels through water before entering the specimen.

Figure 51 : Types of ultrasonic transducer used.

The C-scan device used is automated immersion system, in association with GScan software for data acquisition, control and imaging. The transducers fitted with the probe holding device, can move along two mutually perpendicular directions in precise steps and are capable of scanning any predefined two-dimensional region. The specimen is kept immersed in water and is held parallel to the plane of the movement of the transducer.

Tuning procedures were applied to the ultrasonic C-scan inspection of the various specimens, as it is commonly done, the distance between the transducer and the material (water path) was set at around 25 mm. A steel plate, on which the specimen is

placed, is used as a reflective plane, in order to distinguish the backwall echo from any other one. A linear Distance Amplitude Correction (DAC) curve is used in order to increase the ultrasonic signal amplitude, thus facing the signal losses owing to factors like scattering, absorption, etc. The gates synchronize with the first echo from the specimen and the detection threshold is adjusted to a value above 50% of the Full Screen Height (FSH), thus avoiding the produced noise echoes.

2.5.5. Fiber Bragg grating sensor test

During the static test, the FBG sensor with diameter 125 μm and grating length 15 mm is lit with a broadband light source (ASE FL7002, 1530-1610 nm, FiberLabs). The power spectrum is measured from the reflected light in the FBG sensor, which is embedded inside the stitched laminate. The losses after the fiber optic joining using a Fujikara arc splicer device is 0.00 dB, which it indicated a perfect joining result. The spectrum reflection is measured using an optical spectrum analyzer (MS9710C, Anritsu Co.). And broadband light source will emit until the specimen is broken.

2.6. Results and Discussion

2.6.1. Experimental verification of numerical analysis.

The measured and predicted data were compared for both the combined joint and the bonded-only joint in thin composite structure has a mismatch stiffened. The strain data

from strain gauges and the C-scan result were compared with the finite element analysis result to verify the mechanical behaviour of the specimen, especially at the edge of the stiffener and the area around the rivet hole.

2.6.1.1. Bonded joint model

Figure 52 to 56 compare the strain from the finite element analysis results and the strain gauge measurements for bonded joint specimen. There is a closed agreement on the trend value of both data. Possible explanations for the differences in the results is the installation of the strain gauges, such as imperfect bonding in the joint. In the area of investigation strains gage SC04, the results of the finite element analysis and the strain gauge data, both indicated the occurrence of a peel stress at the edge of the stiffener as a result of the secondary bending moment.

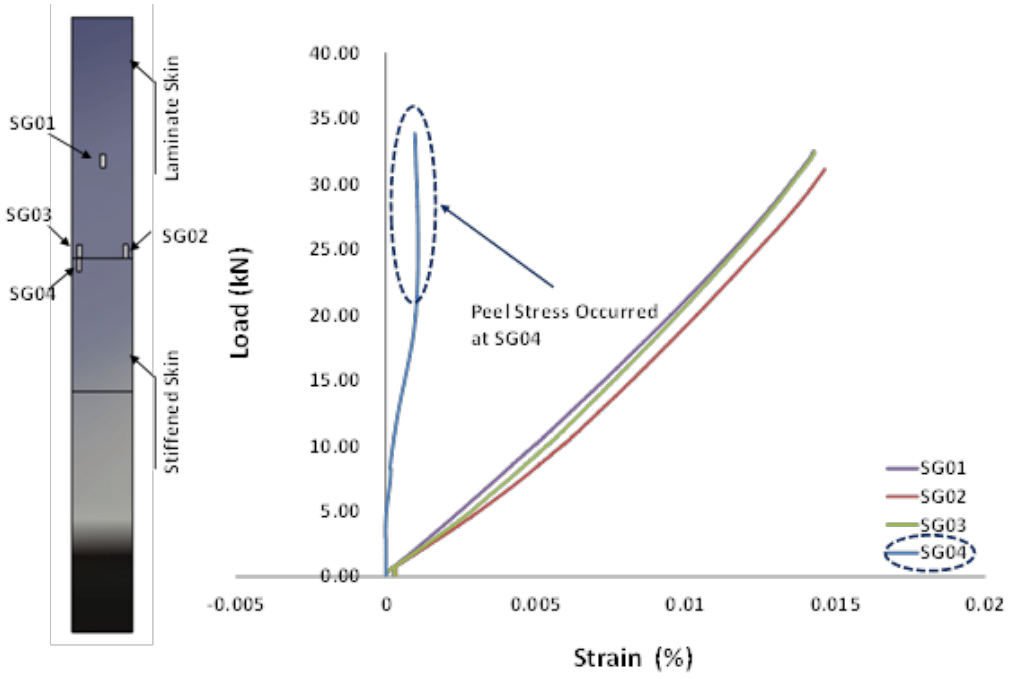

Figure 52 : Locations of strain gages and measurements of the bonded joint.

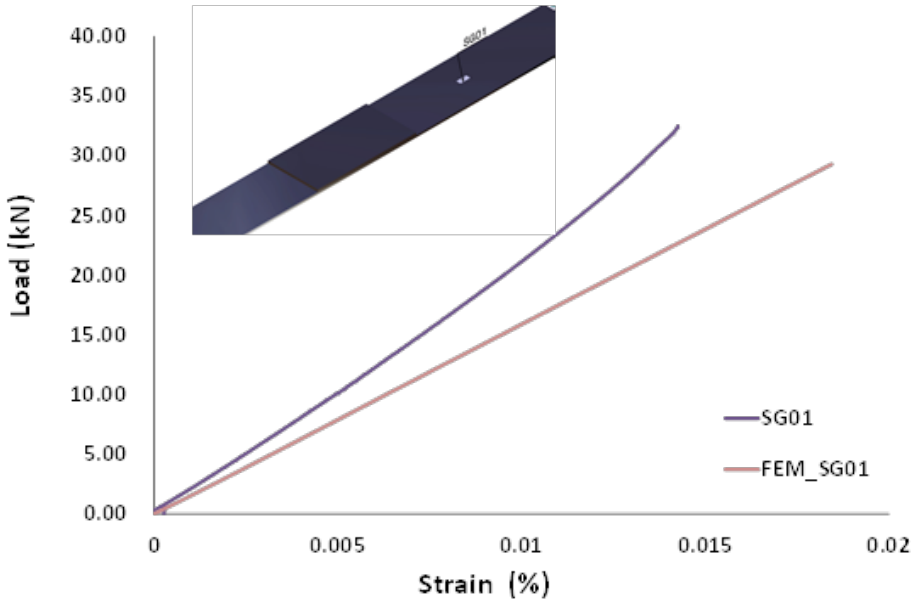

Figure 53 : Comparison between finite element analysis and experimental data at area1 for the bonded joint.

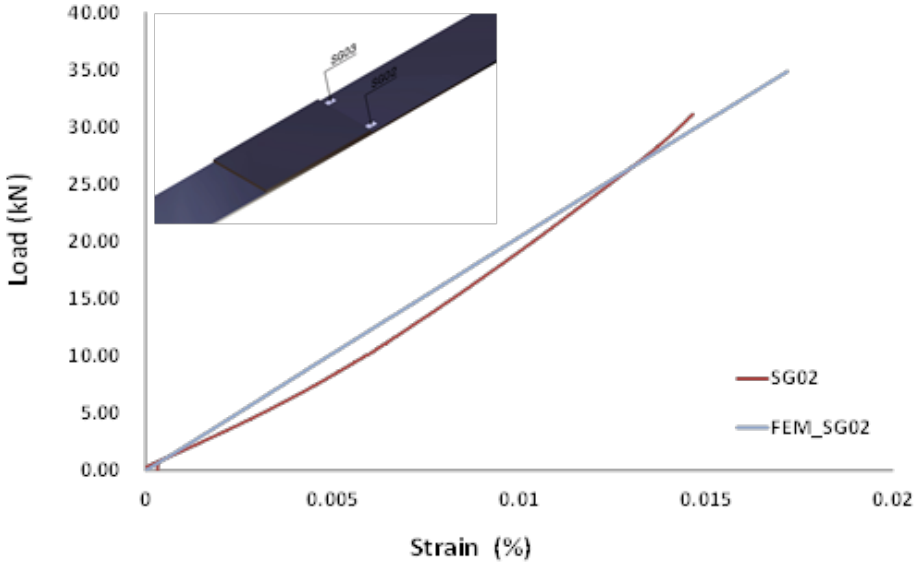

Figure 54 : Comparison between finite element analysis and experimental data at area2 for the bonded joint.

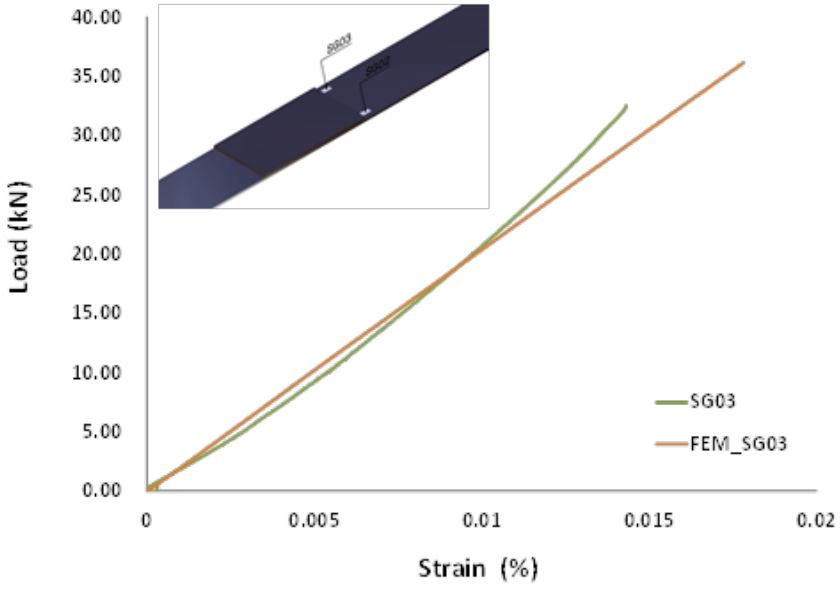

Figure 55 : Comparison between finite element analysis and experimental data at area3 for the bonded joint.

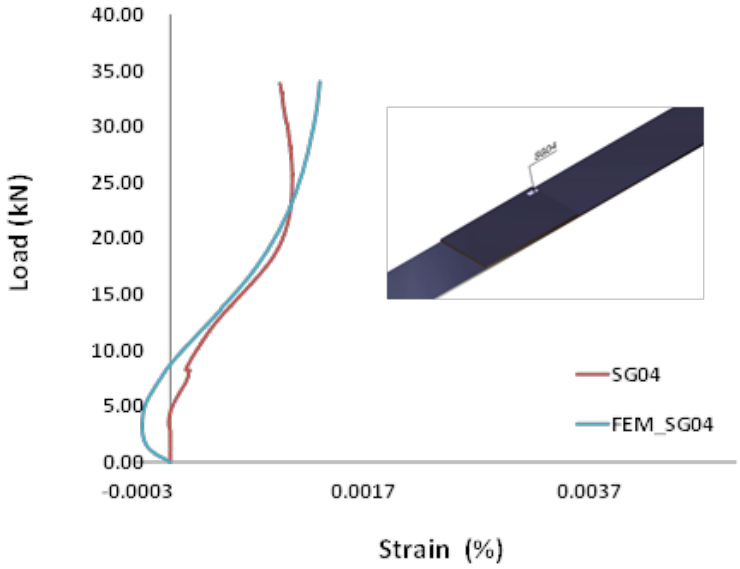

Figure 56 : Comparison between finite element analysis and experimental data at area4 for the bonded joint only.

2.6.1.2. Combined joint model

Figures 57 to 61 show comparison the strain from the finite element analysis results and the strain gage measurements of the combined joint specimen. There is a closed agreement also on the trend value of both data. The addition of the rivet in the stiffened created an excessive stress concentration that caused the specimen to fail at a much lower value compared with the bonded joint only.

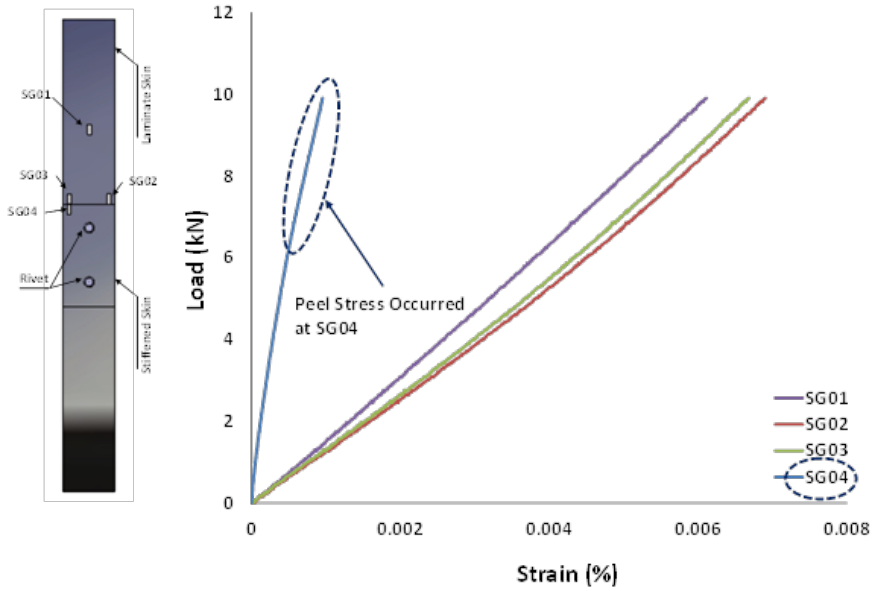

Figure 57 : Locations of strain gages and measurements of combined joint.

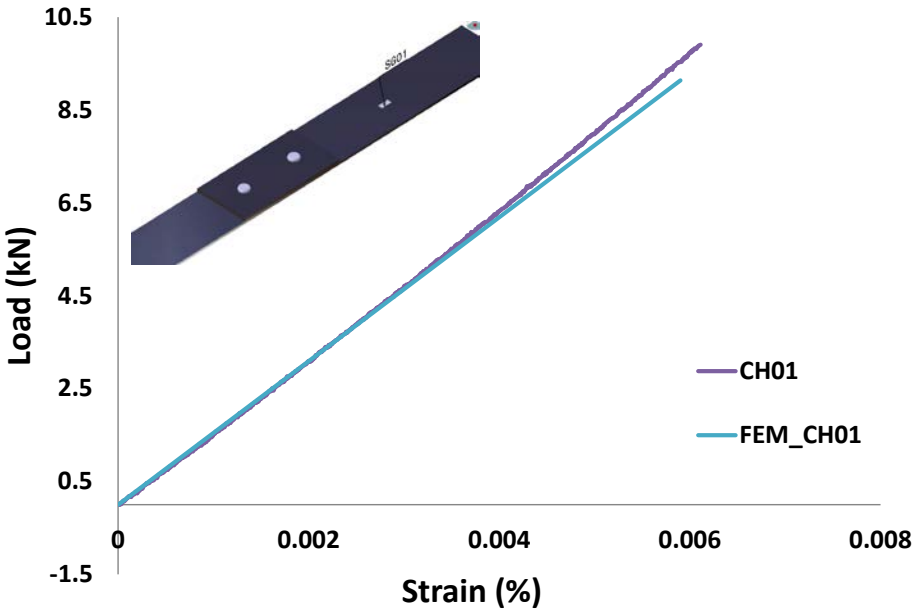

Figure 58 : Comparison between finite element analysis and experimental data at area1 for the combined joint.

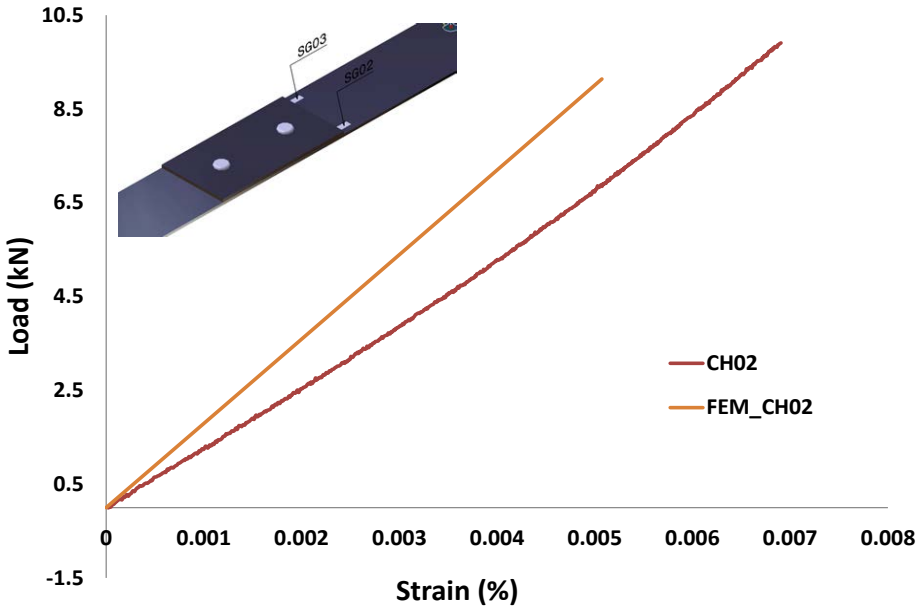

Figure 59 : Comparison between finite element analysis and experimental data at area2 for the combined joint.

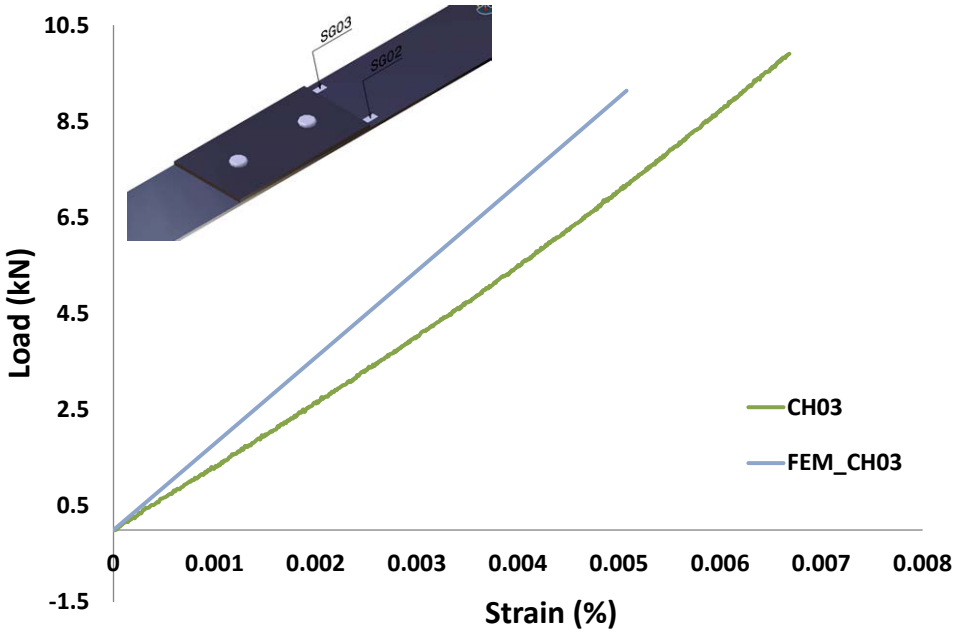

Figure 60 : Comparison between finite element analysis and experimental data at area3 for the combined joint.

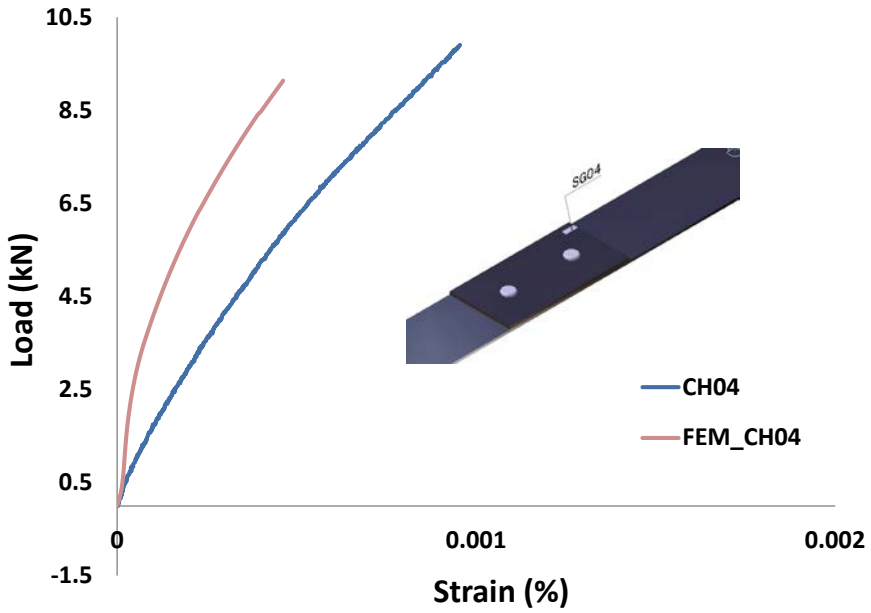

Figure 61 : Comparison between finite element analysis and experimental data at area4 for the combined joint.

2.6.1.3. Ultrasonic C-scan result

The interrupt (loading/unloading) test was performed to gather data for comparison with C-scan data to determine the degree of delamination. The interrupt test was used to simulate real conditions to represent operating-grounded conditions.

Figure 62-63 show the C-can result under interrupted tensile loading. In Bonded joint, it is clear that delamination initiate on the edge of stiffener as a result of peeling stress created by neutral axis changing. While in combined joint, the delamination appears in two places as a result of the two areas of stress concentration:

these areas begin with and around the rivet hole and then grow to the edge of the stiffener. Only a small load is needed to initiate delamination because the high stress concentration occurs near the rivet hole area.

Figure 64-65 show the C-scan result under interrupted three point bending loading. In bonded joint, the delamination occurred gradually and required a high load to initiate and propagate. This difference is caused by shear stress dominance in three-point loading. In another one can be interpreted that the addition of the rivet, which created the stress concentration, is more sensitive in tension than shearing.

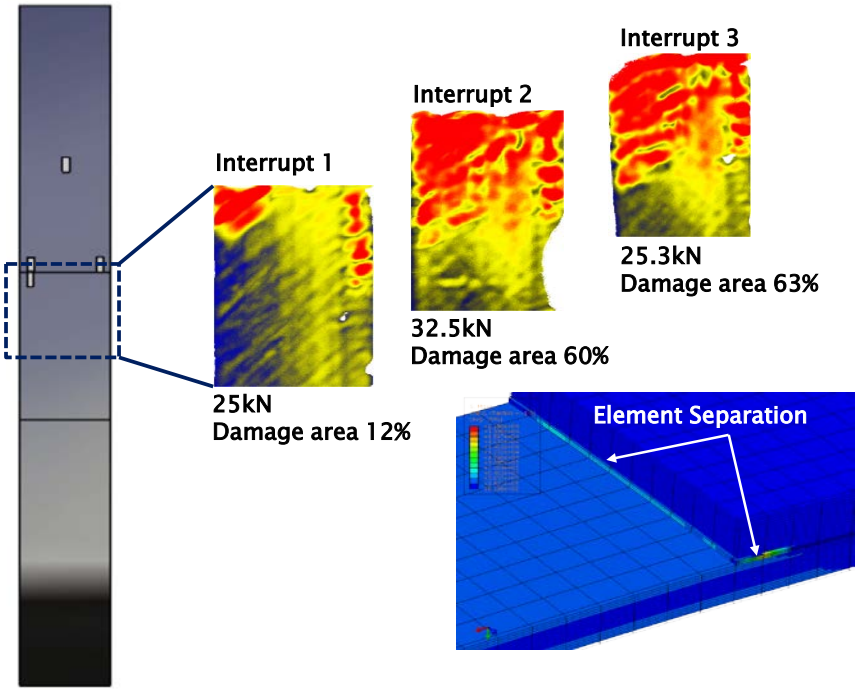

Figure 62 : Tensile loading interrupt tests in bonded joint only.

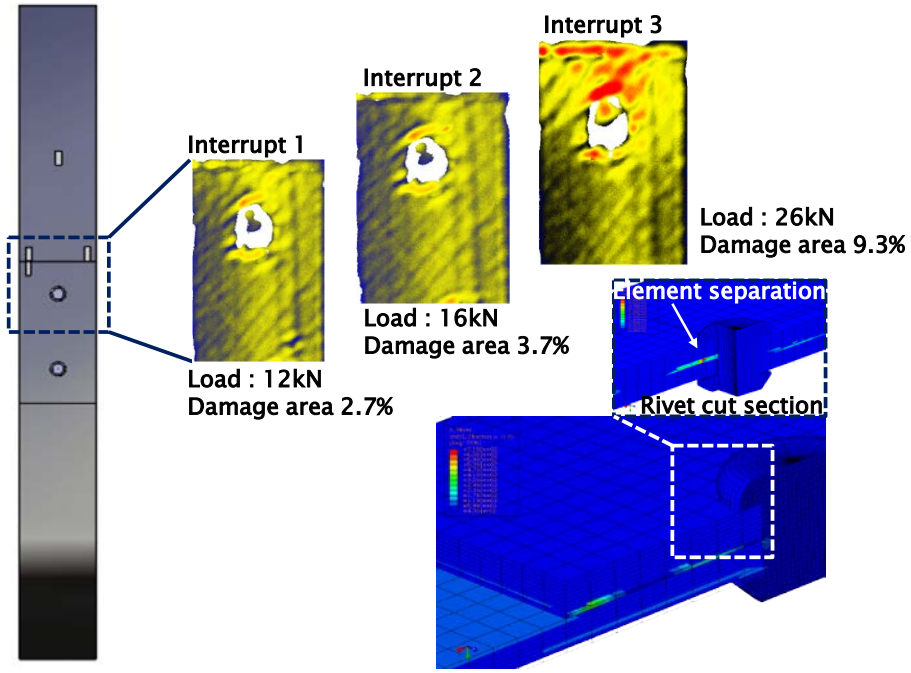

Figure 63 : Tensile loading interrupt tests in combined joint.

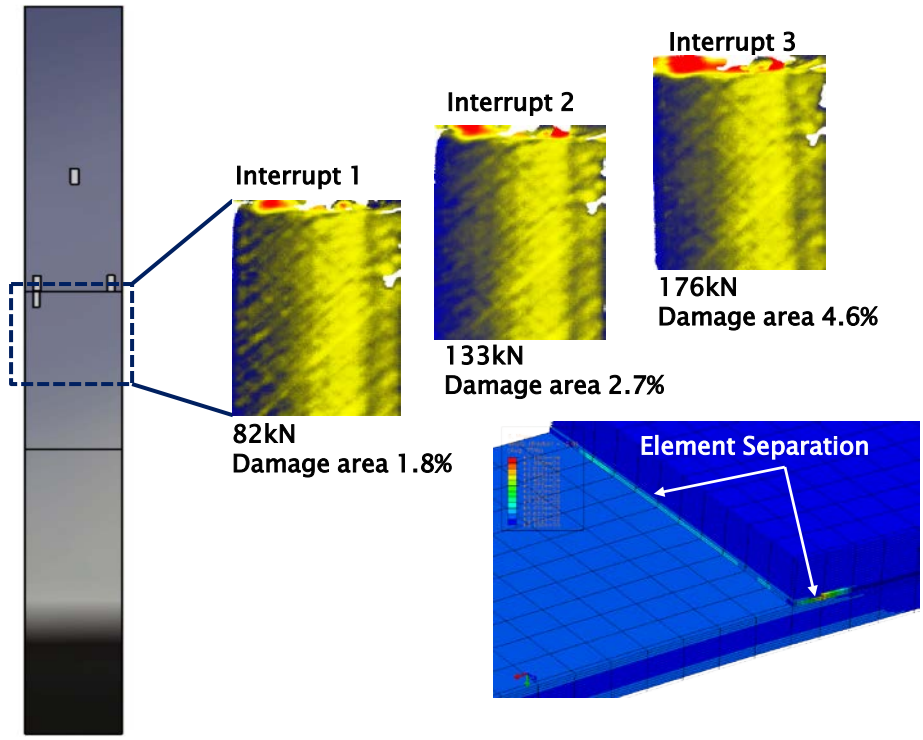

Figure 64 : Three point bending loading interrupt tests in bonded joint only.

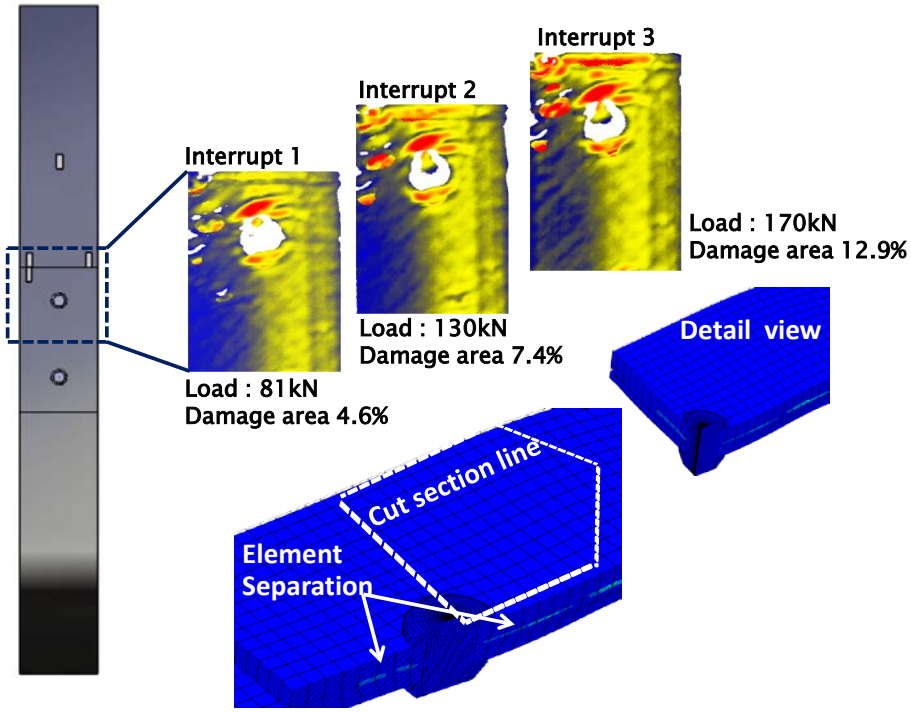

Figure 65 : Three point bending loading interrupt tests in combined joint.

2.6.2. The perspective of FBG sensor reading

The ability of FBG sensors to be integrated with the composite materials and structures is very good natural technology. And the advantage of the technology combined is having the same concepts regarding with lightweight issues caused by almost no additional weight caused by FBG sensor installation.

2.6.2.1. Post-manufacturing spectrum

Figure 66 shows the difference in the FBG sensor spectrum pattern due to the manufacturing process of the specimen. In the bonded joint only, the FBG sensor reflection spectrum has the shape with original/undamaged spectrum reflection, but the

reflection spectrum is deformed for combined joint specimen. This indicates that the riveting process affects the initial form of the spectrum, or it could be that the installation of the rivets causes slight damage that is invisible but can still be detected by the FBG sensor. From the results of the C-scan, we found that the rivet installation using a rivet gun caused minor damage in the area around the hole, as shown by the red color, which is an indication of delamination. While bonding process, the spectrum of the bonded joint only was same as the original/undamaged spectrum. This result demonstrates the sensitivity of the manufacturing process such as the addition of rivets in the FBG sensor reading.

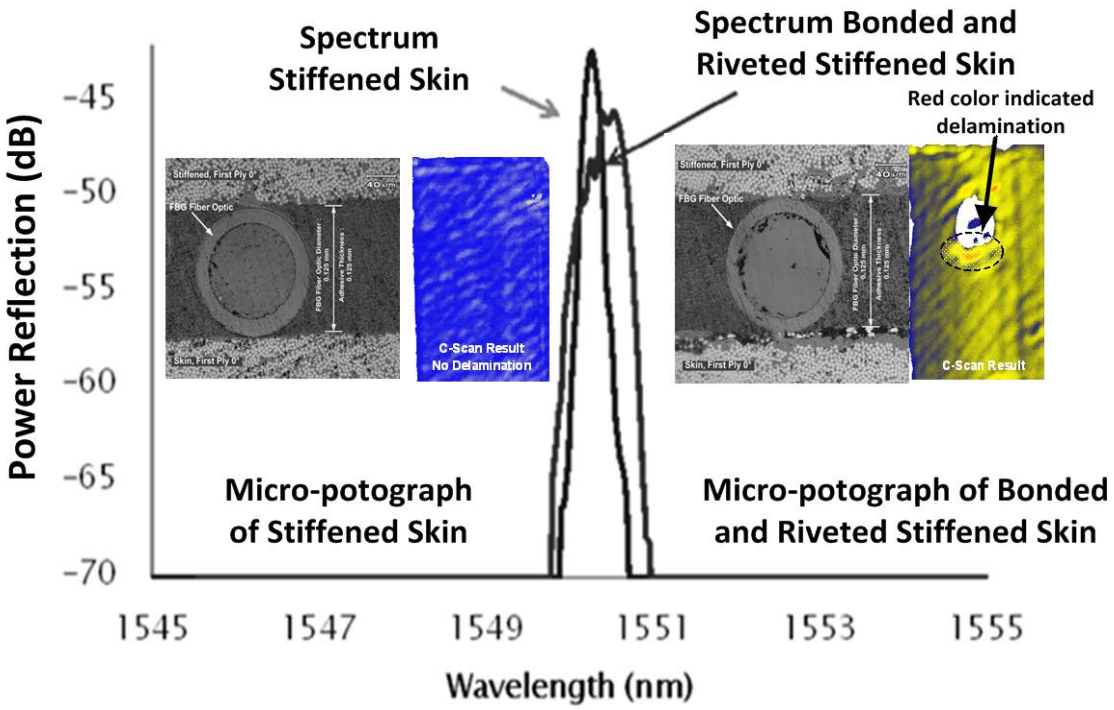

Figure 66 : The effect of post-manufacturing processes for FBG sensor installation based on the spectrum reflection reading.

2.6.2.2. Power spectrum characteristic under tension loading

The spectrum of the FBG sensor was characterized using a static test until specimen failure. The interrupted test was performed to approximate the damage growth of the specimen. An ultrasonic C-scan test was used for damage inspection to get a physical delamination image of the specimen under the interrupted test. Also, only half of the stiffener area was inspected to overcome the limited capability of the ultrasonic C-scan method to detect warpage specimen.

Figure 67 (a) – (l) show the characteristic spectrum evolution of the

bonded joint only under FBG sensor reading. Data acquisition was performed continuously until the specimens fractured. From the data evolution of the spectrum, it can be seen that the spectrum has a consistent pattern during loading evolved with increasing size of the damage. There are two dominant peaks of the spectrum named P_{fp} (first peak) and P_{sp} (second peak) under FBG sensor readings during loading. One peak decreased significantly with an increase in the applied load, while another peak decreased slowly. Two dominant peaks of the spectrum changed with the growth of delamination. It will then be used as a guide to identify the damage and will be explained the detail in the Fig.69.

Meanwhile, Fig.68 shows the combined join under FBG sensor reading. Three dominant peaks occurred: P_{fp} (first peak), P_{sp} (second peak) and P_{tp} (third peak). These three peaks also show a consistent pattern for a given load on the specimen. At first, two dominant peaks appeared as shown in Fig.68 (b) to (d). Then, the third peak appeared as shown in Fig.68 (e) to (i), which indicates the emergence of new delamination in other places.

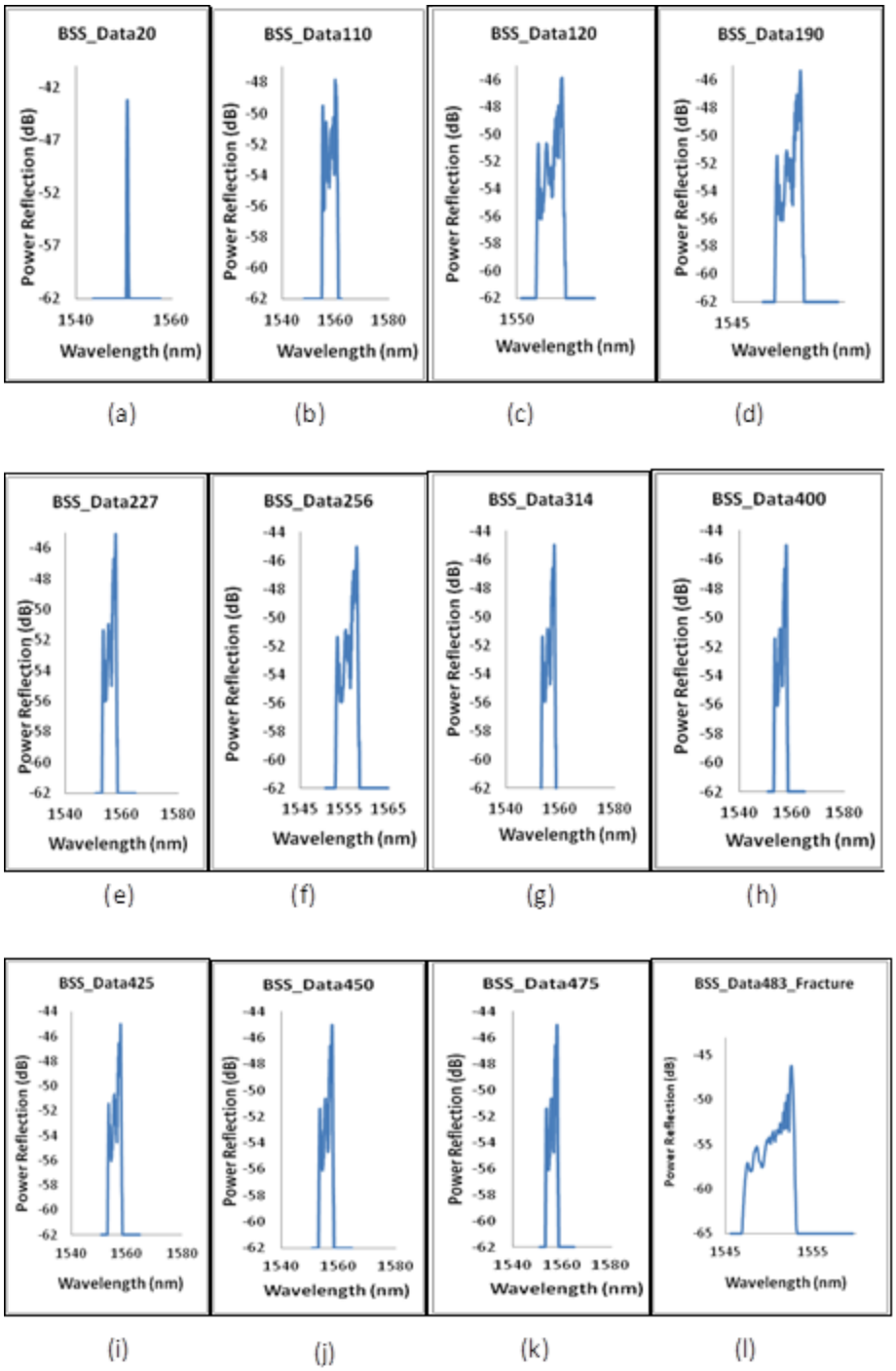

Figure 67 : Evolution of spectrum from FBG sensor reading in bonded joint only.

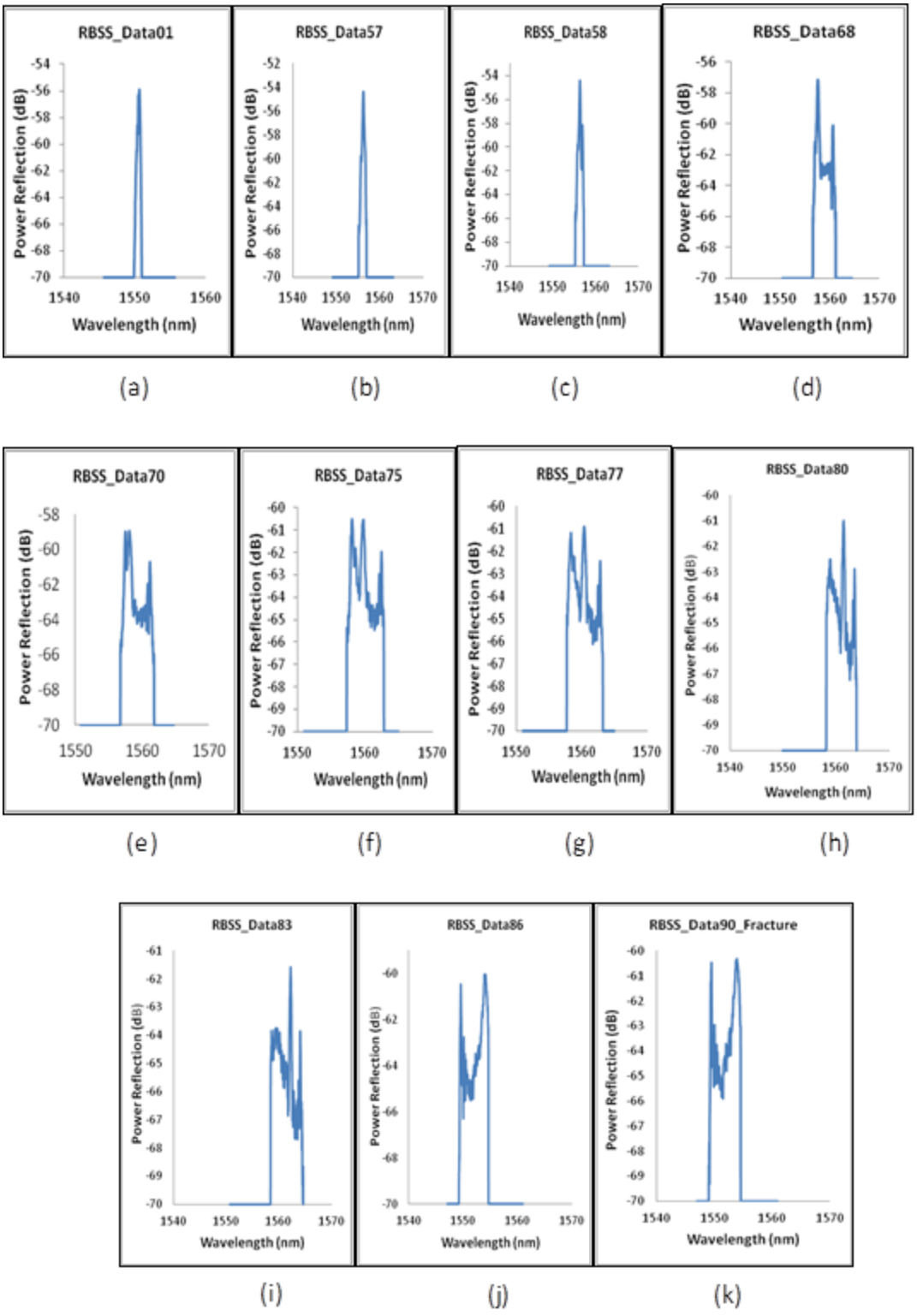

Figure 68 : Evolution of spectrum from FBG sensor reading in combined joint.

Figures 69 (a) and (b) show the spectrum pattern from the FBG sensor reading reading in bonded joint only. The two dominant peaks in the spectrum are defined as P_{fp} (first peak) and P_{sp} (second peak). The appearance of the two peaks in this spectrum has a relatively linear value ratio (P_{fp} - P_{sp}), so it can be used to indicate the growth of delamination as a result of the secondary bending moment on the edge of the stiffener. Delamination started to occur from the two peaks in the intensity spectrum of the FBG sensor reading, in which the delamination size increases and is then followed by a change in the relative value of multiple peaks it used to quantify the size of the delamination. This consistency can be seen from the fact that both peaks remained dominant until the specimen failed and from the different peak heights that are used as a reference.

Figures 70 (a), (b), and (c) show the spectrum patterns from the FBG sensor reading reading in combined join. Delamination started to occur near the fastener hole and grew, and then, a new delamination occurred on the edge of the stiffener as a result of the secondary bending moment on the edge of the stiffener. All of the new delamination grew until the specimen approached failure

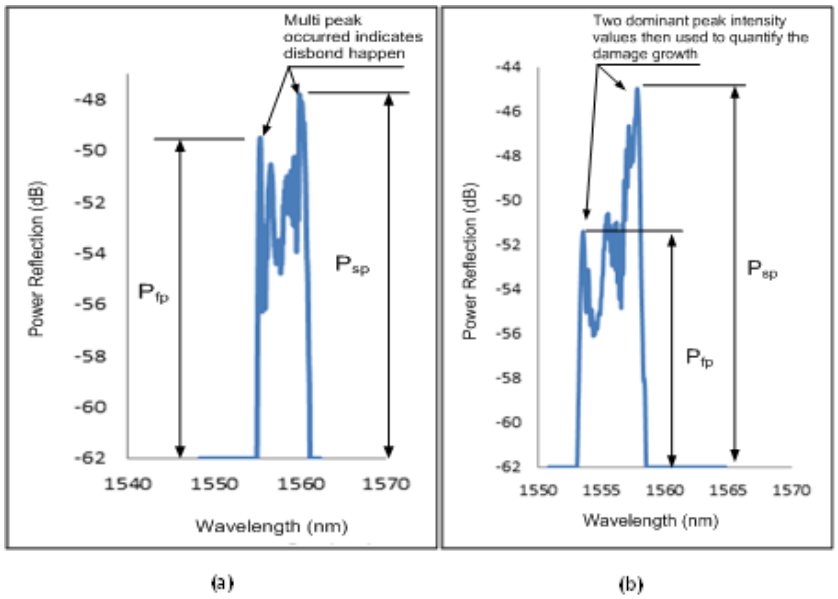

Figure 69 : Spectrum pattern explanation under FBG sensor reading in bonded only.

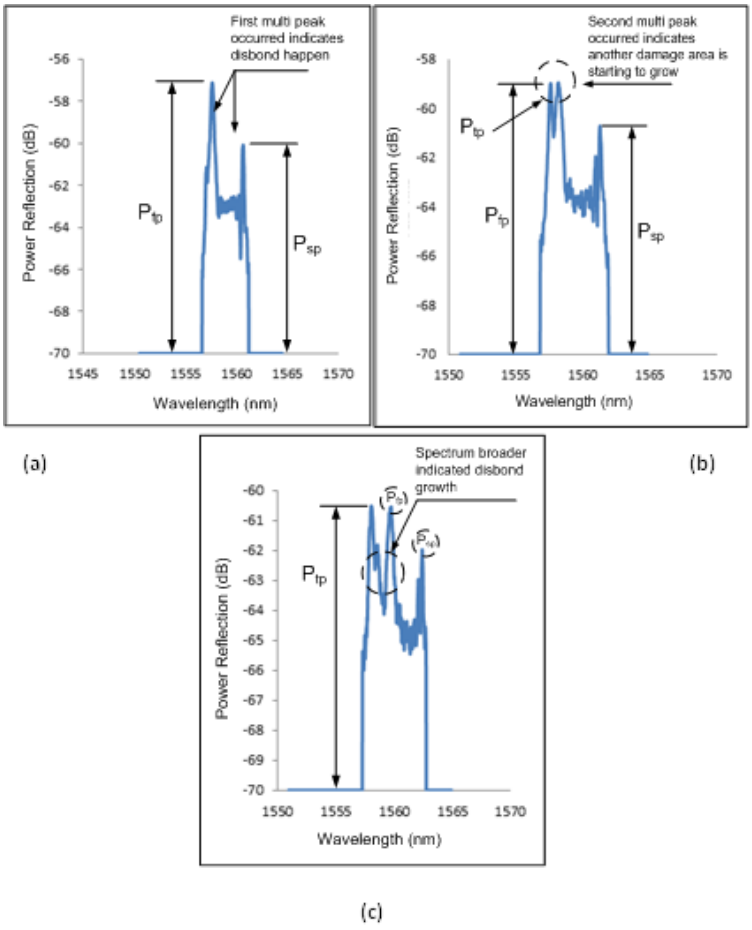

Figure 70 : Spectrum pattern explanation under joint reading in combined join.

Figures 71 (a) and (b) show plotting the spectrum graph versus the mechanical behavior the bonded joint only under tensile loading. After concentrating load in the stiffener area, then all loads covered with the adhesive in the joint area and then peeling mode failure begins. It was indicated by the absence of load increasing, but the displacement ascent until the specimen break. The spectrum shape was also broad and changed significantly and it was indicated damage occurred. After load becomes constant, the shape of spectrum reflection was not changed until the specimen was broken. The graph also shows both the normalized intensity and the normalized wavelength give a clear indication that the normalized graph can be followed by either mechanical graph, which means that the normalized graph can represent the mechanical characteristics of the graph.

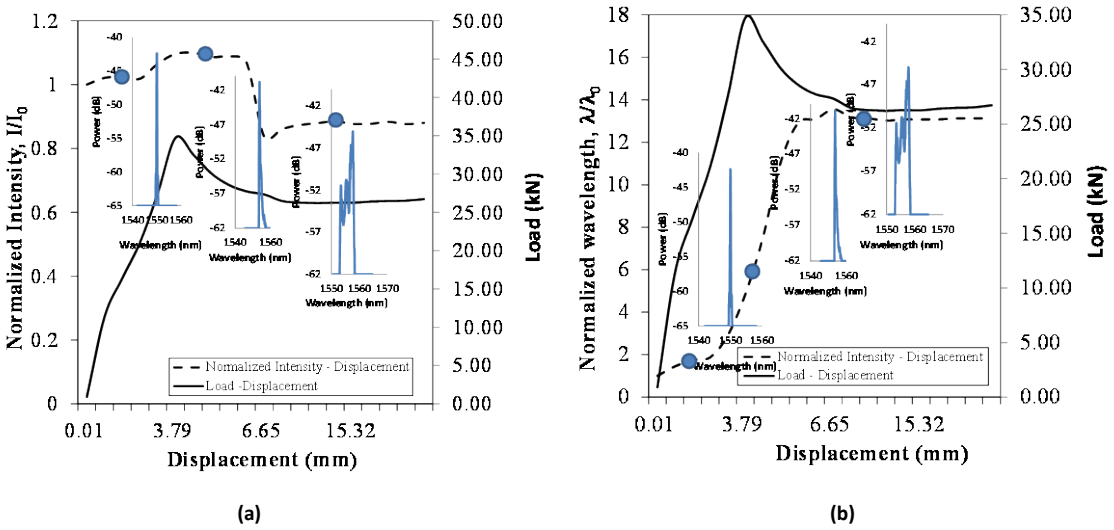

Figure 71 (a) (b) : The relationship between normalized intensity and normalized wavelength during loading run in bonded join only structure has a mismatch stiffened at the tensile test.

Figures 72 (a) and (b) explains the relationship between normalized intensity and normalized wavelength during a loading run in combined join under tensile loading. These graphs explained that normalized intensity and normalized wavelength as clue of damage progression. It was correspondingly revealed that spectrum reflection spacious and has developed compared with the original spectrum shape. After damage occurred indicated with spectrum reflection broad and advanced, normalized intensity graph declined expressively while loading ascents, and also for normalized wavelength graph increased significantly after damage happen. It was shown with wavelength broad expressively while load increased. Riveting process with

pressure rivet gun introduced damage prior loading, created bearing failure and caused damage growth faster.

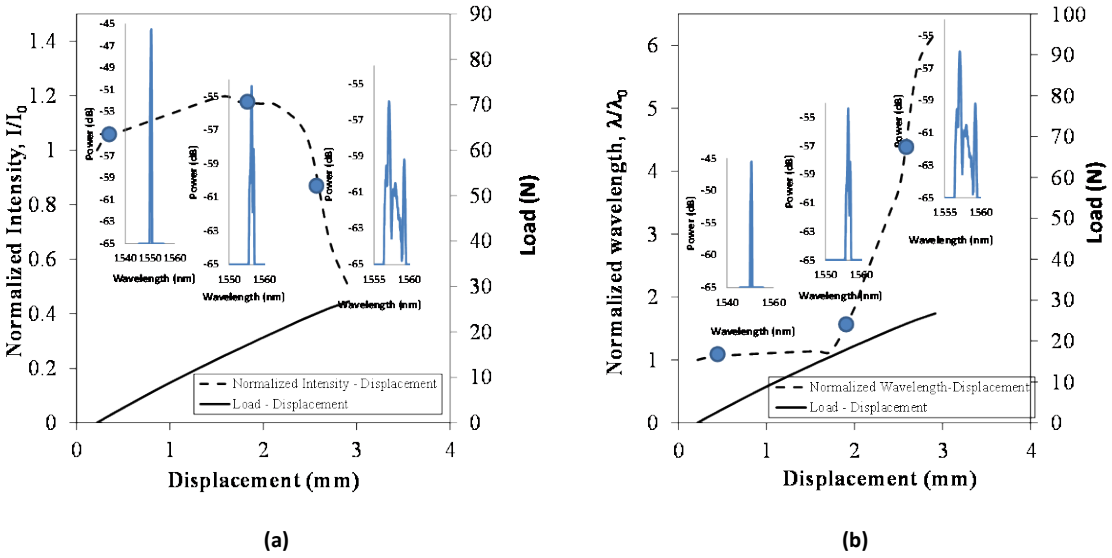

Figure 72 (a) (b) : The relationship between normalized intensity and normalized wavelength during a loading run in combined join.

Figures 73 (a) and (b) show the damage resistance (indicated by the failure speed over time) curve comparison between the two specimen models under tensile loading. In combined joint showed damage growing faster than bonded joint only. It could be seen from normalized spectrum and wavelength which changing more significant than bonded joint only. The addition of rivet has led to a post-manufacturing damage due to drilling process and the presence of stress concentration during loading.

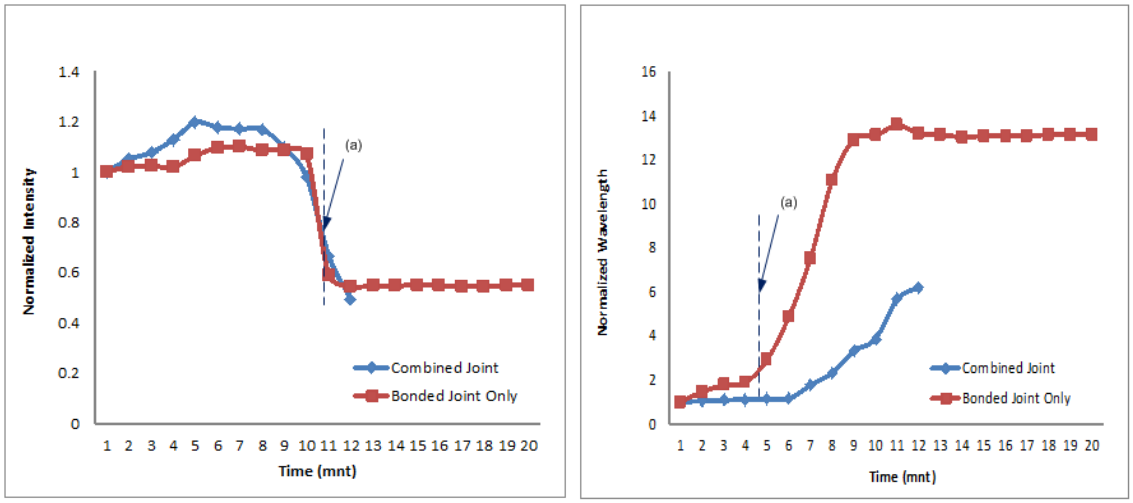

(a) (b)

Figure 73 (a) (b) : Comparison normalizing power intensity and wavelength for bonded join only and combined join due to resistance to damage under tension loading. *(a) It indicated the damage start to growth.

2.6.2.3. Power spectrum characteristic under three-point loading

Figure 74 shows the spectrum pattern from the FBG sensor reading in the combined joint. There is no multi-peak happen in three-point bending loading like in under tensile loading. It caused strain as long grating length of FBG sensor is linear, thus only single-dominant peak happens during loading run. But behaviour of wavelength showed broader linearly, then distant between λ_0 and λ_1 become wider significantly when delamination occurred. This phenomena then become clear as

delamination quantification of the specimen combining with C-scan result.

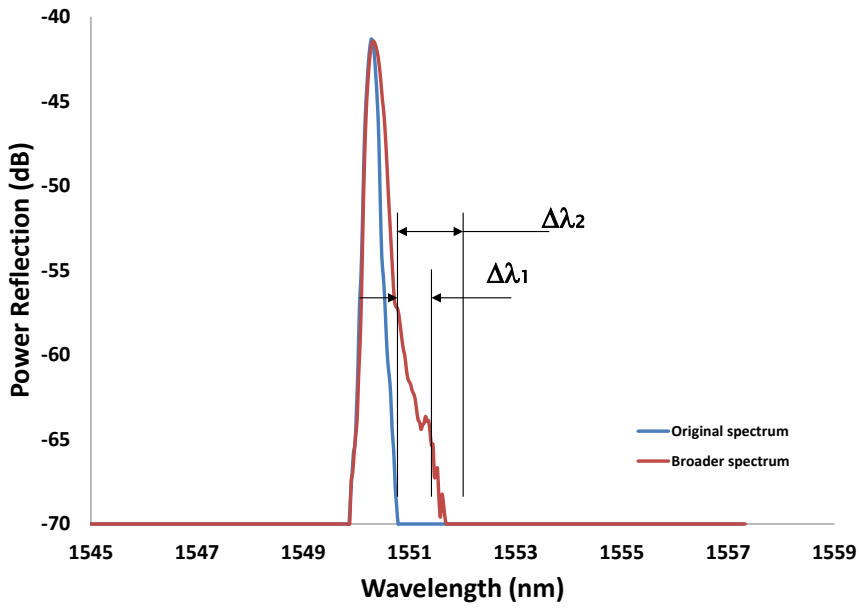

Figure 74 : Spectrum pattern evolution under FBG sensor reading in combined join in three-point loading.

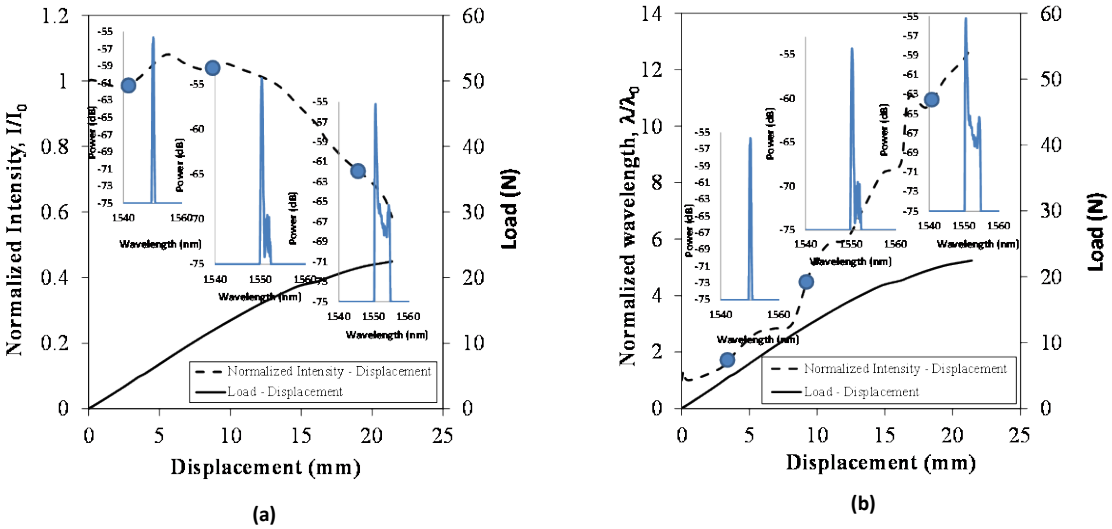

Figure 75 (a) (b) : The correlation between normalized intensity and normalized wavelength to during a loading run to combined join at three point bending.

Figures 75 (a) and (b) explains the combined joint characteristics comparing the spectrum graph versus the mechanical behaviour under three point bending loading. These graphs clarify that normalized intensity and normalized wavelength during loading run could be used as an indication of damage growth. It is also shown that spectrum reflection broad and has advanced compared with the original spectrum shape. After damage occurred, the normalized intensity curve decreased significantly while loading increased, but normalized wavelength curve increased significantly while load increased. The riveting process with a pressure rivet gun also introduced damage prior to loading, created bearing failure, and caused damage to grow faster. It is shown that the spectrum shapes changed dramatically compared with bonded joint only as shown in Fig.76. The addition of rivets has led to post-manufacturing damage due to the drilling and rivet installation processes and the presence of stress concentrations during loading.

Figures 76 (a) and (b) explain the relationship between normalized intensity and normalized wavelength of bonded join only under three point bending loading. These graphs explain that normalized intensity could not be used as a precept of damage growth because the normalized intensity have value almost same during a loading run. It was a typically uniform strain response of FBG sensor reading. But

normalized wavelength during loading run could be used as an indication of damage growth. It was also shown that the wavelength constantly broad compared with the original spectrum shape. After damage occurred, normalized wavelength curve increased significantly while load increased. It was meant that the normalized wavelength could be used for damage quantitative measuring in uniform strain failure.

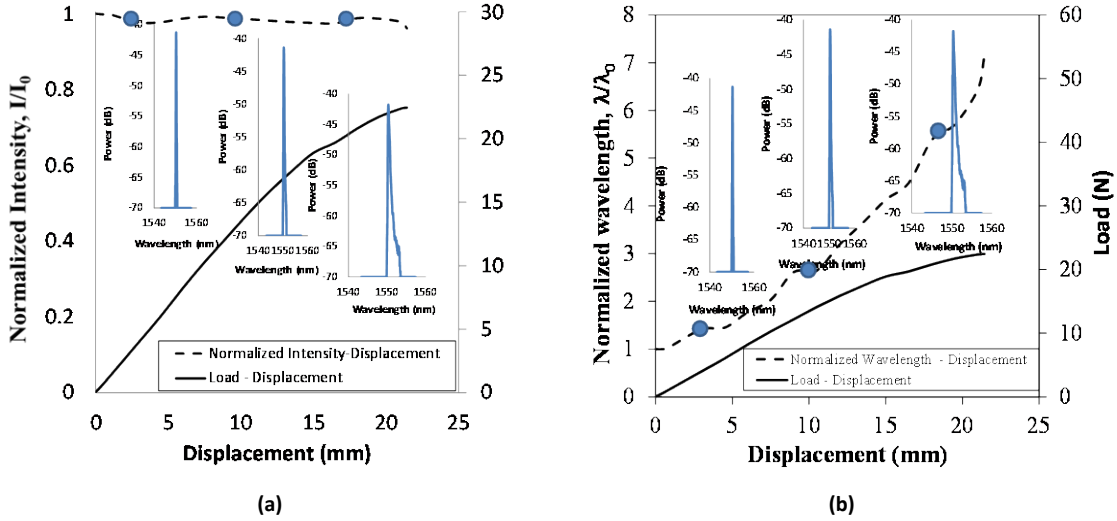

Figure 76 (a) and (b) : The relationship between normalized intensity and normalized wavelength during a loading run of bonded join only at three point bending test.

Figures 77 (a) and (b) explains the curve comparison between two specimen models under three point bending loading. In this case, combined joint showed damage growth slightly faster than bonded joint. The difference in damage growth was more significant in a tensile loading compared with in three point bending loading. This means that the addition of rivet may have benefits to shear loads and this

can be seen on the load-displacement graph in which combined joint displacement was higher than in bonded joint only. And bearing failure due to the addition of rivet was not dominant in the shearing load case.

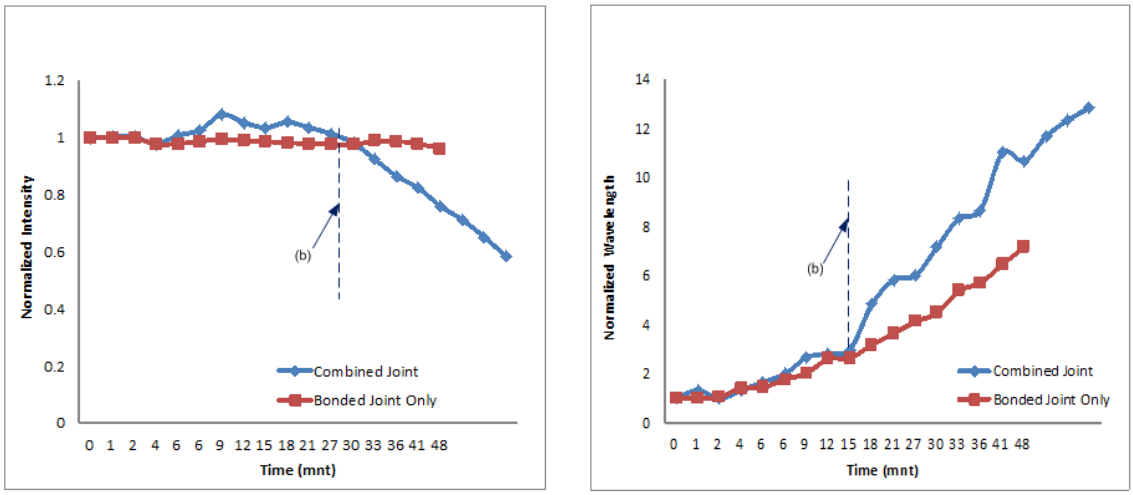

(a) **(b)**

Figure 77 (a) and (b) : Curve comparison in normalized intensity and wavelength between two specimen models under three point bending test. *(b)It indicated the damage start to grow.

2.6.2.4. Power spectrum characteristic under loading-unloading test

The reflection spectrum changes due to loading–unloading are also important in describing the real condition of the aircraft structure during operation, and it is indicated by the interrupted load test. The three locations selected for load interruption are determined based on the changes in the reflection spectrum shape,

which indicate damage initiation or damage growth. The importance of the interruption test is that the loading–unloading spectrum reflection data can be used to determine the critical level of damage in the aircraft structure (if applied in an aircraft) when the aircraft is in the on-ground position (when no load is present, it can be compared with the reference reflection spectrum). Also, the difference in the spectrum of the secondary bending failure characteristics from continuous loading and interrupted loading for the developed damage at any point of the interrupted load tests are indicated by the results of the ultrasonic C-scan.

Figures 78 (a) - (d) show the reflection spectrum changes in the combined joint during the loading-unloading under tensile test. In this case, the reflection spectrum was not only a change indication of the occurrence of multi-peak but also a change indication in wavelength broad. From C-scan results of the interrupted load test first to third could be seen that there was a significant damage growth in the area around a hole. This showed that the addition of rivet will create a stress concentration and strength of the structure will decrease caused by bearing failure happened.

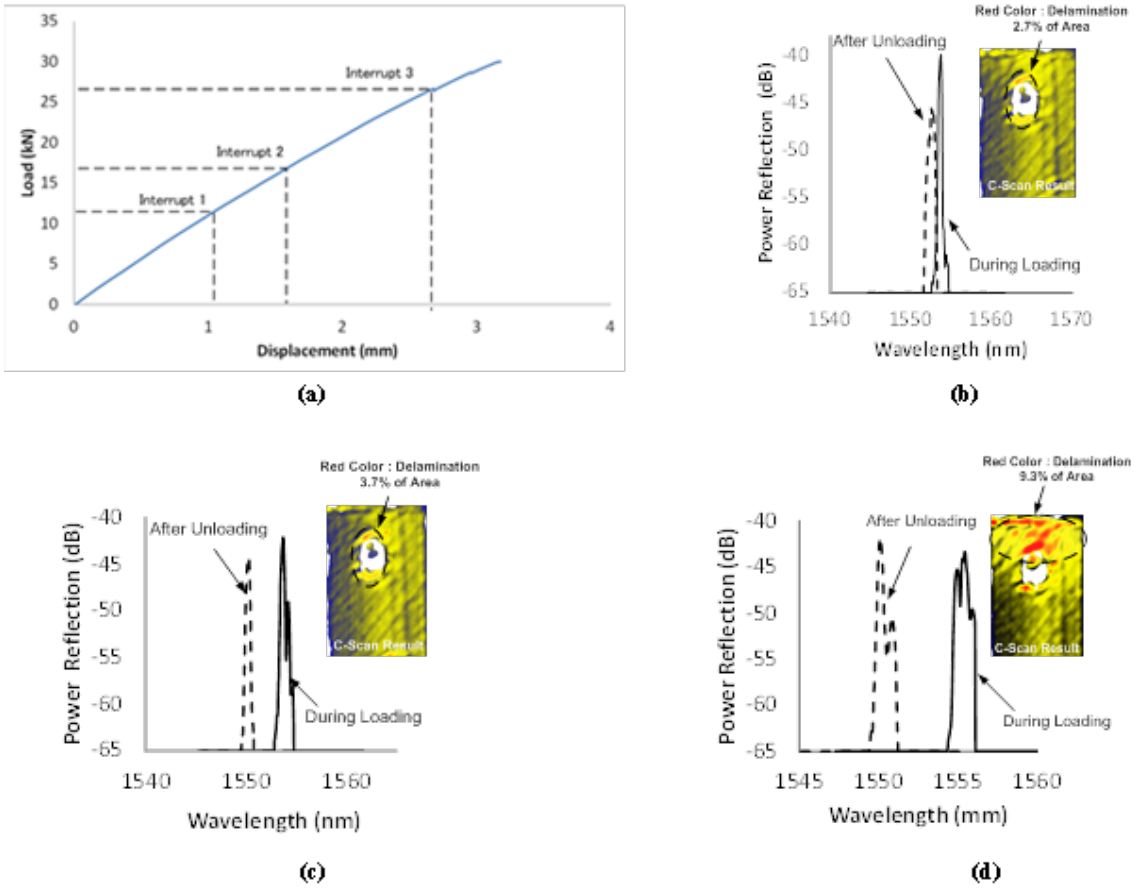

Figure 78 : (a). The load - displacement curve of combined join under tensile test and location of load interrupted during test running. (b) Interrupted 1st at Displacement: 1 mm, Load: 10.6 N and Damage area: 2.7%. (c) Interrupted 2nd at Displacement: 1.5 mm, Load: 14.5 N and Damage area: 3.7%. (d) Interrupted 3rd at Displacement: 2.5 mm, Load: 23.50 N and Damage area: 9.3%.

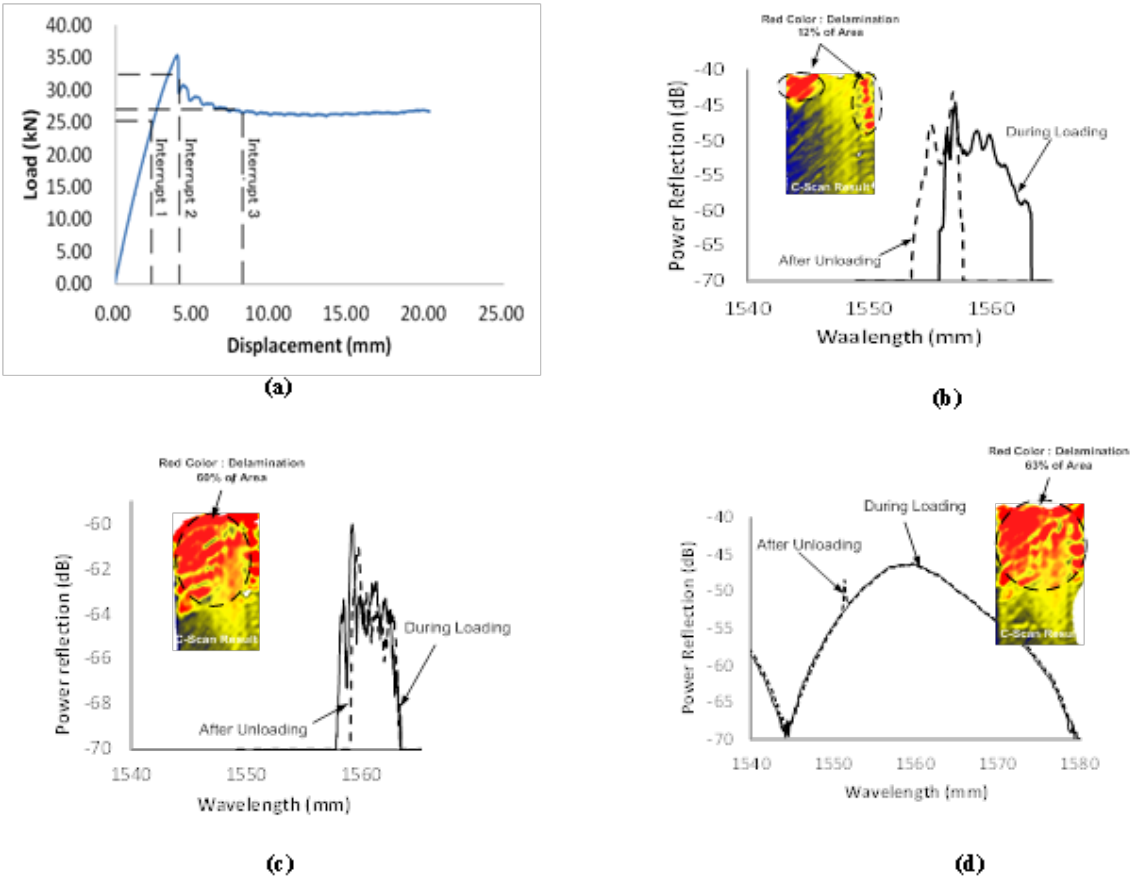

Figure 79 : (a). The load - displacement curve of bonded join only under tensile test and location of load interrupted during test running. (b) Interrupted 1st at Displacement: 2.5 mm, Load: 25 kN and Damage area: 12%. (c) Interrupted 2nd at Displacement: 4.5 mm, Load: 32.5 kN and Damage area: 60%. (d) Interrupted 3rd at Displacement: 7 mm, Load: 25.3 kN and Damage area: 63%.

Figures 79 (a) - (d) show the load-strain curve of bonded joint only during a tensile test and the location of the interrupted test. The location selection of load interrupted is determined when the reflection spectrum shape changes that indicate

initiation damage occurred or damage growth. In interrupted test will be known spectrum shape changes during loading-unloading conditions and the growth of the damage taken from C-scan in a response spectrum of behavior. Sloping line shows adhesive failure was started. Load almost constant in this phase as peeling failure characteristic created by secondary bending phenomena. In the third interrupted load test, spectrum reflection could not be recited as qualitative data to indicate damage and the growth, possibly affected FBG sensor was already strained too high as shown wavelength broad and advanced.

Figures 80 (a) - (d) show the interrupted load test of combined joint under three point bending loading. The graph indicated that no significant change in spectrum reflection until interrupted load test third if comparing with bonded joint only. This shows that added of rivet gave a positive value on damage resistance of the specimen. It was also indicated with a displacement value was higher than the bonded joint only. But in the third interrupted load test, the spectrum reflection broader significantly. That was also meant damage growth significantly in that phase. Based on C-scan result, there was not indication that damage growth was caused by the addition of rivets, but rather indicated as a damage growth on bonded joint only.

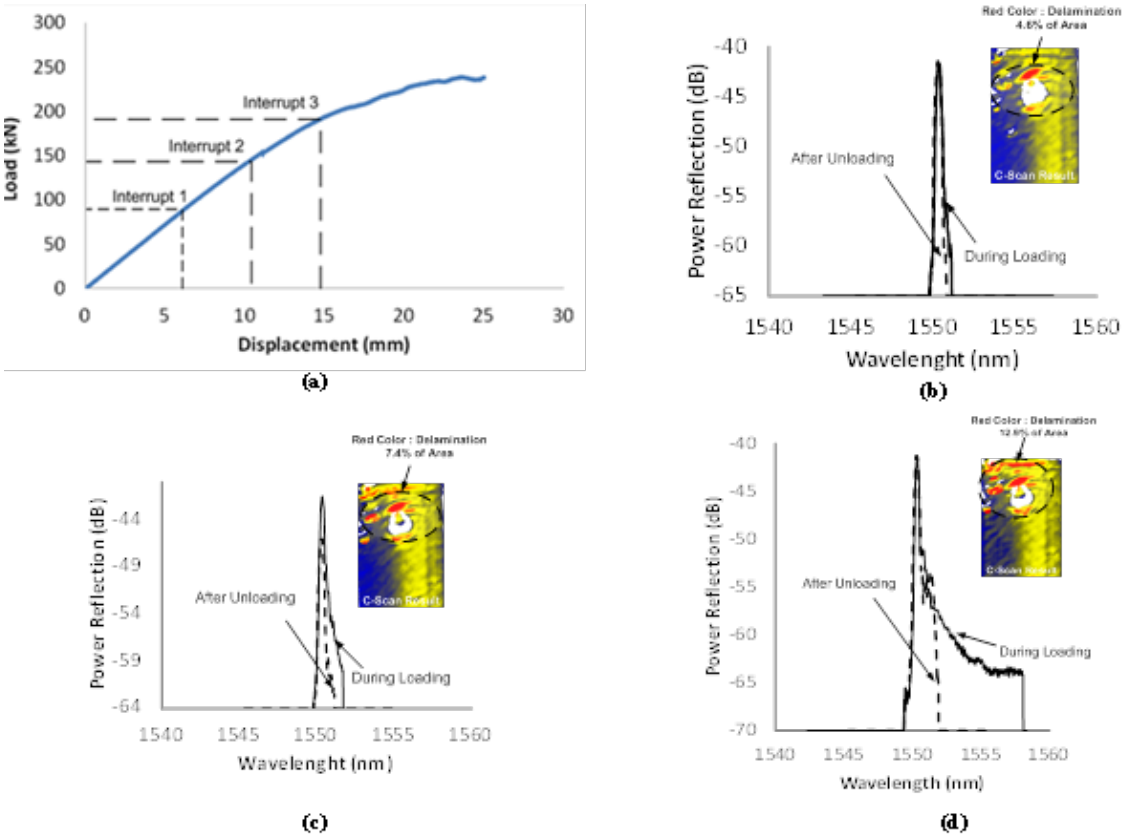

Figure 80 : (a). The load - displacement curve of combined join under three point bending test and location of load interrupted during test running. (b) Interrupted 1st at Displacement: 6 mm, Load: 81 N and Damage area: 4.6%. (c) Interrupted 2nd at Displacement: 10 mm, Load: 130 N and Damage area: 7.4%. (d) Interrupted 3rd at Displacement: 14 mm, Load: 170 N and Damage area: 12.9%.

Figures 80 (a) - (d) show the interrupted load test in three levels of load of bonded joint only under three point bending loading. The reflection spectrum became broader and developed some peak in the spectrum shape. The emergence of multi peak

in the spectrum shape indicated damage occurred. And if the spectrum reflection became broader it was indicated damage became growth as shown in the figure with a damaged area larger.

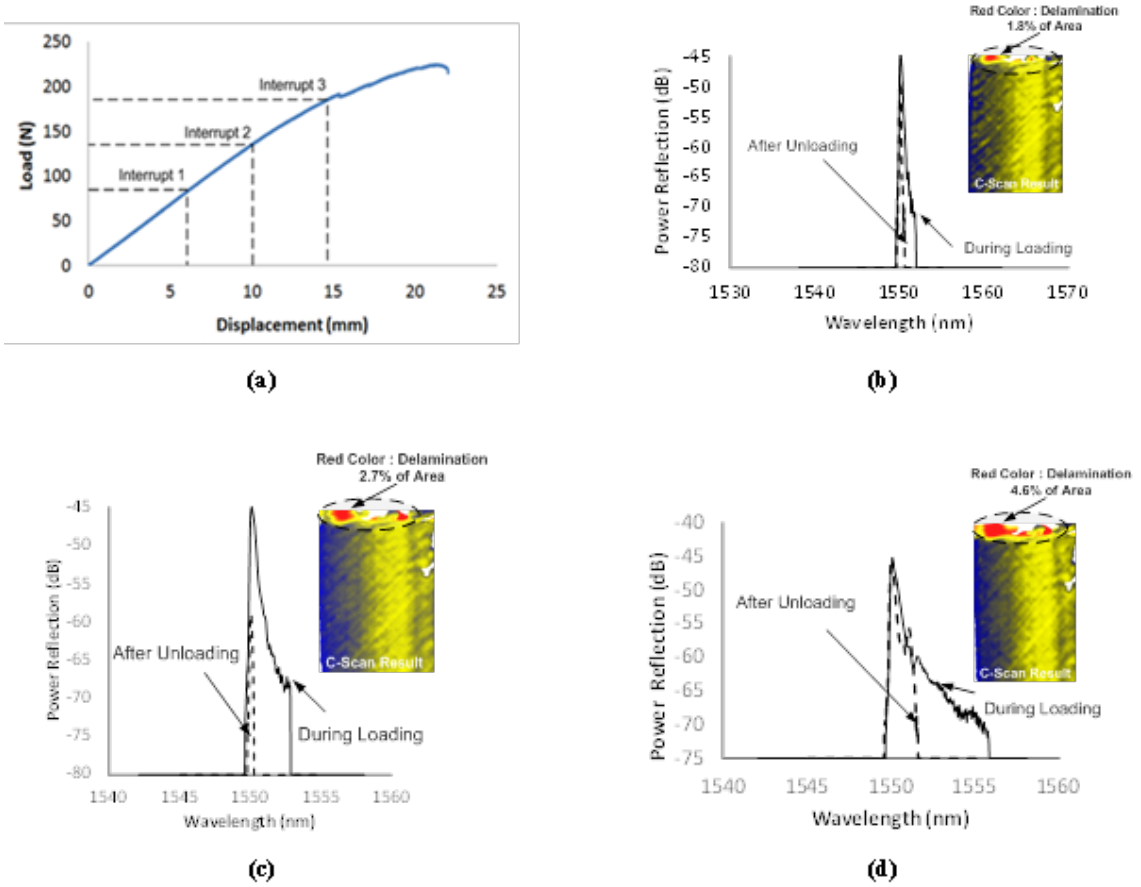

Figure 81 : (a). Graphic load - displacement of bonded join only under three point bending test and location of load interrupted during test running. (b) Interrupted 1st at Displacement: 6 mm, Load: 82 N and Damage area: 1.8%. (c) Interrupted 2nd at Displacement: 10 mm, Load: 133 N and Damage area: 2.7%. (d) Interrupted 3rd at Displacement: 14 mm, Load: 176 N and Damage area: 4.6%.

2.6.3. Damage quantification.

Figure 82 (a) shows the ratio (P_{fp} - P_{sp}) in relation to the delamination growth in the bonded joint only specimen, where quantification is obtained by referring to the ratio of the difference between P_{fp} and P_{sp} and is then compared with the trend of the delamination size as the result of the ultrasonic C-scan result for the specimen. Meanwhile, Fig.82(b) shows the graph plotted the damage quantification on combined joint. it was evaluated in the same way to obtain the average ratio with the formulation [(P_{fp} - P_{sp}) + (P_{fp} - P_{tp})]/2 in relation to the delamination growth. The trend lines in the graph have some notable differences; in the bonded joint only, the line increased in the relationship between the spectrum ratio and the damage area, but in the combined joint, that line decreased. The reason is in bonded joint only used ratio value, while in the combined joint used average ratio value. The important information is that both specimens have a linear trend corresponding to the delamination size and growth in the spectrum under the FBG sensor reading.

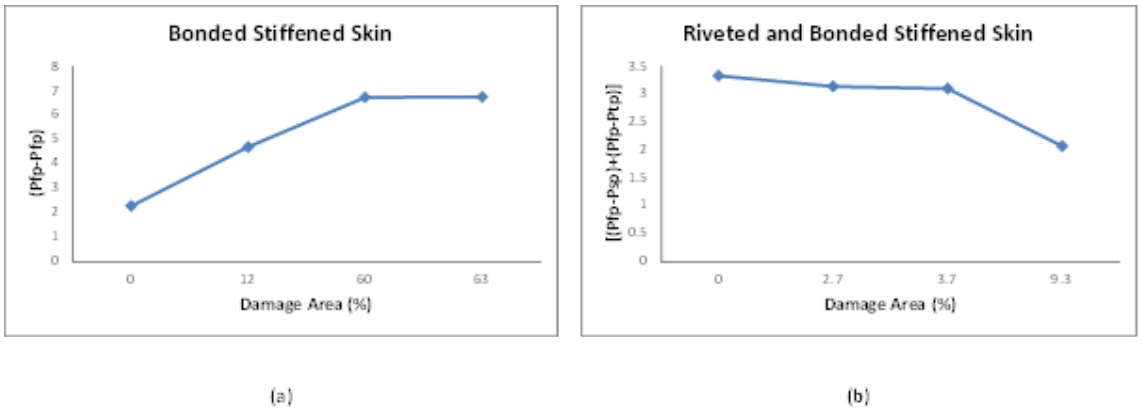

Figure 82 : Quantification ratio of spectrum intensity due to damage area of bonded join only and combined joint.

Figure 83 shows the ratio of wavelength (λ_1 - λ_0) in relation to the delamination growth in the combined join, where quantification is obtained by referring to the ratio of the difference between λ_1 and λ_0 and is then compared with the trend of the delamination size as the result of the ultrasonic C-scan result for the specimen. The wavelength used because in the three-point bending loading, load distribution along the grating line of FBG sensor was linear, therefore no multi peak occurred, but wavelength broader significantly during loading run. The wavelength broader consistency happens during loading run, then it used as clue for damage quantification by comparing C-scan result.

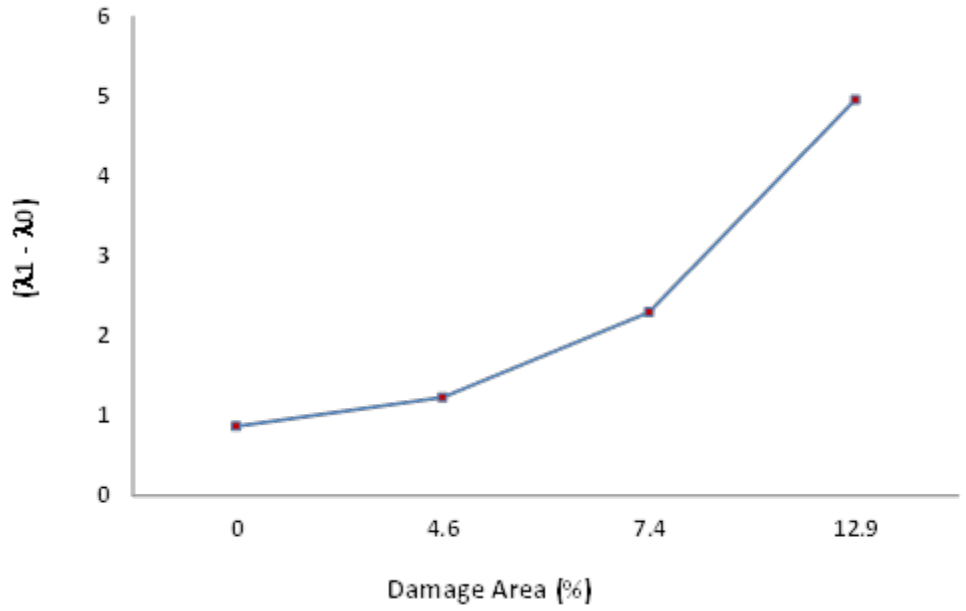

Figure 83 : Quantification ratio of wavelength due to the damage area of combined join in three-point bending loading.

Figure 84 shows the comparison damage rates for both joints. It can be observed that the damage to the combined joint occurs faster and propagates more rapidly than in the bonded joint only. The reason is that in combined joint, multiple areas of stress concentration occurred; in the edge of the stiffener and in the area around the rivet hole, where the rivet hole has the most dominant effect on the propagation of damage. Nearly all of the load applied to the specimen is concentrated on the rivet holes, causing rapid damage propagation in the transverse direction.

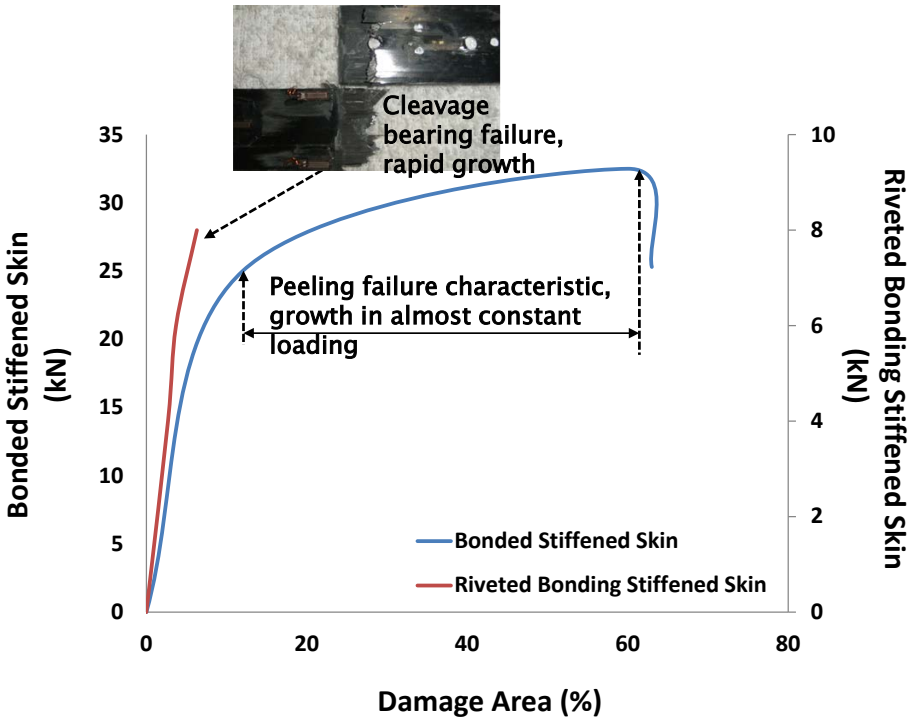

Figure 84 : Delamination growth: stress concentrations around rivet holes leading to catastrophic failure in cleavage bearing mode.

2.7. Conclusions

The behavior of a thin composite structure with stiffness mismatch in the bonded joint only and combined joint has been demonstrated by numerical analysis and experimental approaches. Continuous damage monitoring using FBG sensor has also demonstrated. FEA predicted the mechanical behavior of the structure, which demonstrates a fundamental behavior difference under tensile and three-point bending loading. Where the normal stress at the edge of the stiffened plays an important role in initiating peeling failure due to tensile loading as shown in Fig.20-21, the addition of a

rivet induces a high risk of bearing failure because nearly all of the given load flowed into the rivet area. In the case of three-point loading, the normal stress distribution shifted to the middle of the specimen as shown in Fig.32. The addition of a rivet increased the resistance to out-of-plane failure at the edge of the stiffness bearing failure, and the risk of bearing failure is small because the load transfer to the rivet area occurred gradually. The experimental approach showed a close trend between strain gage measurements and finite element analysis results as shown in Figs.52-56. The prediction of the growth of delamination in the specimen model also showed a close trend as shown by the results of the C-scan in Figs. 62-65. These conclusions show that the predictions by numerical analysis can be verified well by experimental approaches.

Numerical and experimental approaches have become crucial to determine proper placement of the FBG sensor because the FBG sensor is only able to detect damage adjacent to the grating length. As a result, the behavior of the model and its tendency to damage must be understood before fabrication of the specimen to avoid misreadings.

We conclude that the FBG sensor can detect initial damage caused by secondary bending moment and its subsequent growth properly as predicted by finite element analysis and corroborating with experimental data. FBG sensor is also can detected load shifted caused by multi stress concentration in combined join. This indicates the

sensitivity of FBG sensor to sense the load changing. The occurrence of damage to the specimen can be characterized by FBG sensor with the occurrence of multiple peaks in the power reflection and significantly broader peaks in wavelength. The damage growth can be quantified successfully by FBG sensor readings through the appropriate ratio between multiple spectrum peaks and through the differences in the wavelength ratios. New graph as result of FBG spectrum reading are proposed as shown in Figs.71-72 and Figs. 75-76 as fundamental graph in SHM and it related to this problem. It are poposed to change the conventional stress-strain mechanical graph to understand the mechanical behavior in SHM field. Additionally, if the damage induces a non-linear response at the FBG grating sensor period, then the multi-peak power reflection and wavelength broadening can be used to characterize the damage as indicated by Figs.69-70 and Fig.74. However, if the damage to the specimen still provides a linear response to the FBG sensor period gratings, damage characterization can be performed using the wavelength evolution even if a multi-peak spectrum does not occur as demonstrated by Fig.75(b) and Fig.76(b).

CHAPTER 3 : DAMAGE DETECTION AND MONITORING OF STITCHED LAMINATE MATERIAL.

3.1. Overview

There are numerous aspects and questions related to the use of composite materials for primary structures in aircraft. This is especially true if the main concerns are that the material should have good reliability and durability for the primary structural application. Composite laminates are highly sensitive to out-of-plane failure due to their low interlaminar fracture toughness. One of the best methods to increase the damage resistance is through-the-thickness reinforcement such as stitching. Recent studies have shown this technique can enhance damage tolerance to levels obtainable with toughened resin systems, but contrary it also creates complex failure mechanism. However, for next-generation aircraft, material improvement alone is not enough to assure or increase the safety and reliability of the structure. Continuous damage monitoring during operation will become an important issue in aircraft safety after long time usage. Embedding FBG sensor into the composite structure as strain sensors could potentially solve the above problem because the FBG sensor can be used to detect and characterize the damage before it reaches a critical stage.

The real-time monitoring using the FBG sensors is combined with acoustic emissions that were conducted during the test in this chapter. A classical lamination

theory and first-ply failure criterion are performed to determine the suitable area on the specimen for the FBG sensor installation before manufacturing. Interrupted loading tests are conducted to determine the damage growth that was quantified with an ultrasonic C-scan inspection.

3.2. A Stitched Laminate Concept with FBG Sensor Installed in.

One of the outstanding features of composite material is their ability to match with individual loading or stiffness requirements. Therefore, it follows that many types of different angle-plied laminates are likely to be encountered in different applications.

Figure 85 shows the schematic diagram of the adopted stitching process by Toyota Industries Corporation. Stitched laminate material basically involves inserting a strong fiber thread through a stack of fabric plies in the through-the-thickness direction. Stitching technique has proven to be an effective way of suppressing delamination growth in composite material with reducing the driving force for delamination propagation. The stitching creates closing tractions action across the delamination which resist the delamination tip from the full effect of opening stresses[41-44]. The use of stitching technique in various applications, like lap-joints and T-joints, are evidence that this technique provides a remarkable solution to increase delamination resistant. Then

with complex of the failure mechanism of stitched laminate material, it is important to improve the safety and reliability with embedding FBG sensors during the manufacturing process that can be used to monitor damage within the material[53-59].

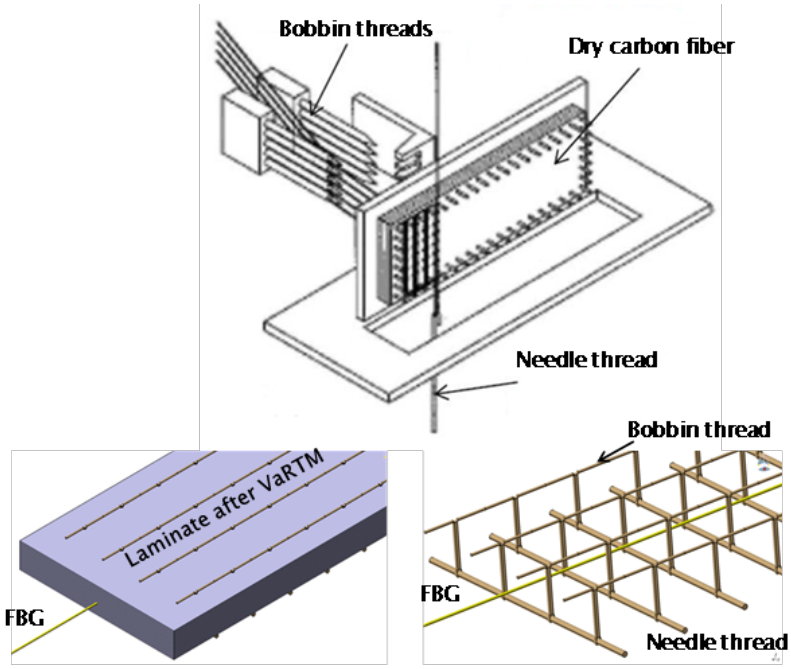

Figure 85 : The schematic processes of the adopted stitching process by Toyota Industries Corporation with FBG sensor embedded into the laminate.

3.3. Numerical Analysis

3.3.1. Geometry and Configuration.

Figure 86 shows the geometry of the stitched laminate specimen. Stitched laminate specimen will build in 20-ply stacking sequence $[45/90/-45/0_2/45/90_2/-45/0]_s$ of T800SC-24K/RTM6 with 6x6 stitch (400-denier Vectran HT) spacing. The stitched

laminate had the following mechanical properties: σ_{t1} = 1721 MPa, σ_{c1} = 1000 MPa, τ_{12} = 105 MPa, E_{t1} = 132.66 GPa, E_{t2} = 12.06 GPa, G_{12} = 3.72 GPa, and ν_{12} = 0.36. The stitch material had the following mechanical properties: E_{t1} = 72 GPa and ν_{12} = 0.3. And the specimen has dimensions of 230 mm long and 25 mm wide. The thickness of specimen is 4 mm.

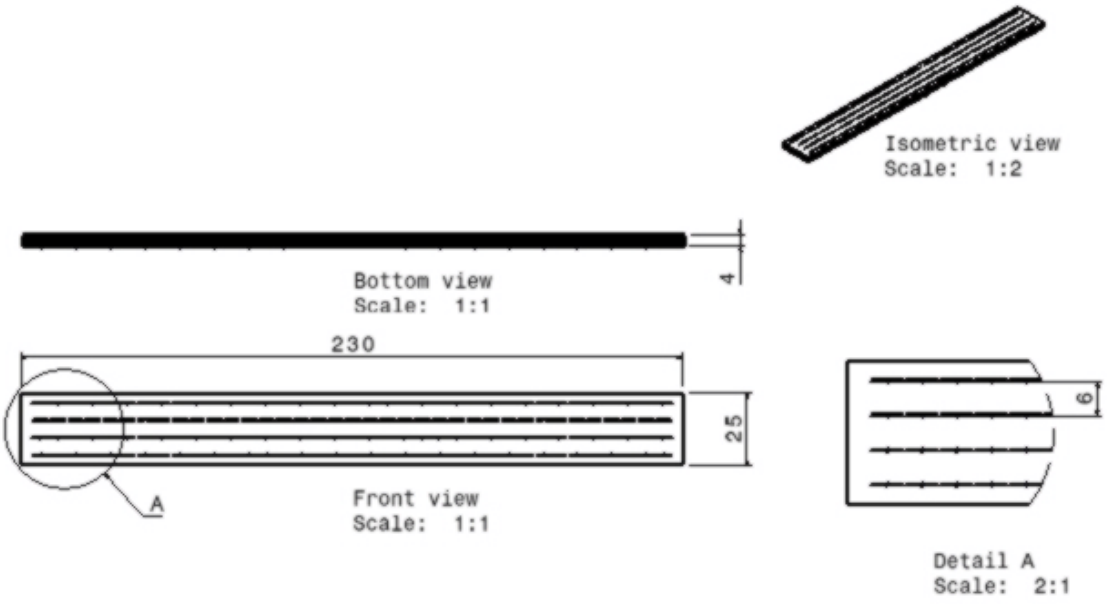

Figure 86 : Specimen model configuration for stitched laminate. All dimensions in mm.

3.3.2. Methodology

3.3.2.1. FEM Analysis Parameter

A finite element analysis of a stitched laminate material was developed using the ABAQUS. To determine the mechanical behavior accurately, including the interface load transfer between the stitching and the host/laminate, three-dimensional

modelling was required, where the pair contact between the stitching to laminate was modelled using rebar technique.

Figure 87 shows a solid model of stitching embedded into laminate as a host material. This alternative computational approach has been successfully applied in computational mechanics of reinforced concrete structures in the context of the infinitesimal theory, see, e.g., Meschke et al[45], turned out to be remarkably effective in finite strain analyses of cord-reinforced rubber composite material, e.g., Sprenger. W et al[46].

Figure 88 shows a boundary condition on the specimen. A half model is analyzed based on the symmetry condition along the length of the specimen to reduce the computational time. The analyses were performed under a tensile load applied to the other end of the specimen, which was free to move in the longitudinal (x) direction only ($u_y u_z = 0$). The opposite end of had clamped boundary conditions. The specimen was fixed in the vertical (z) direction for symmetry condition.

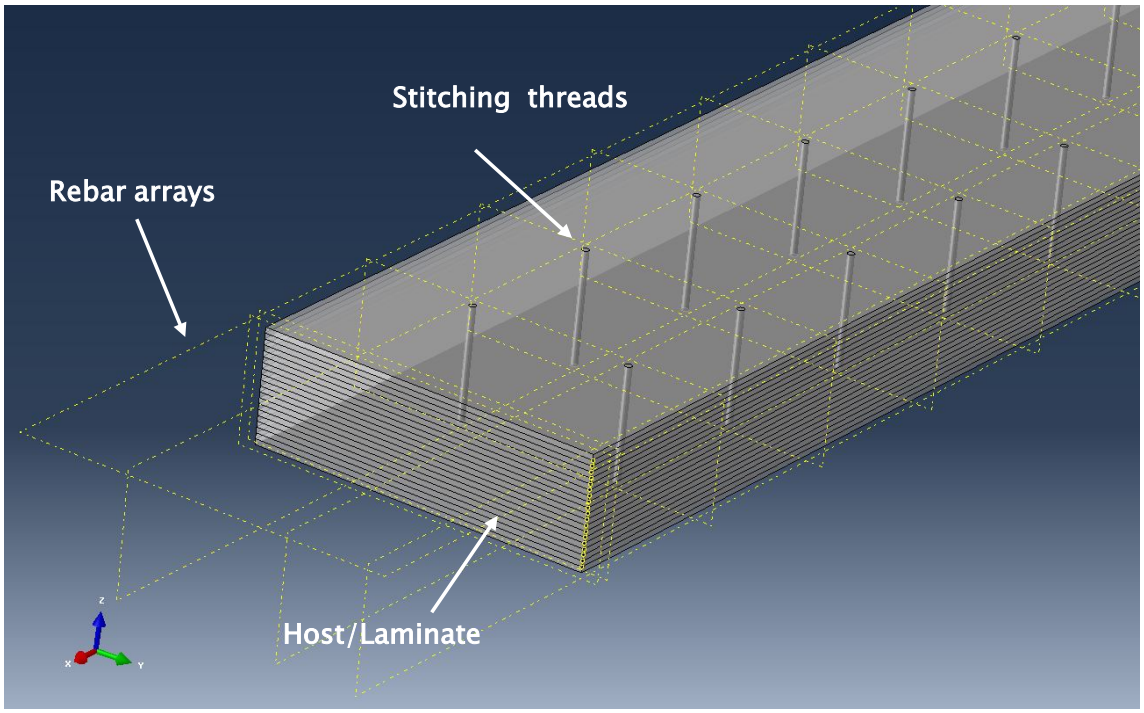

Figure 87 : Three dimensional modelling of stitching into the laminate by using rebar model.

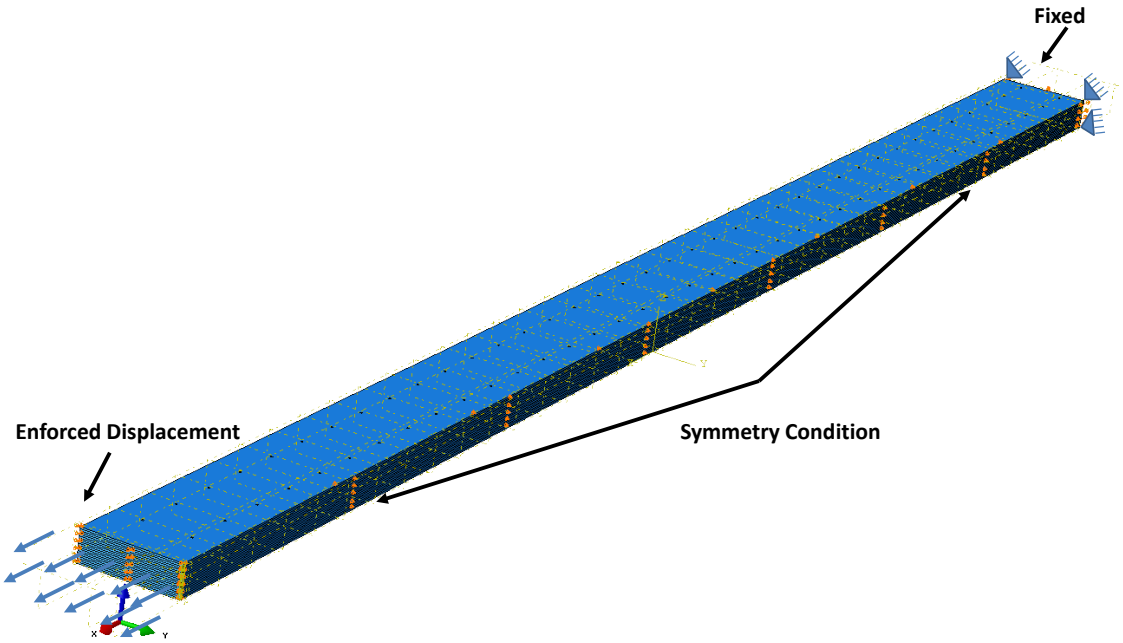

Figure 88 : Boundary condition of the specimen.

3.3.2.2. Stitching threads modelling approach

Stitching threads are modelled using rebar model. Rebar model may be characterized as "overlay" elements that represent one or more cord layers with arbitrary orientation in conjunction with corresponding elements representing the laminate material[42-44]. The laminate element and the "overlay" element share the same nodal points. Therefore, no additional degrees of freedom are introduced. This approach possesses a number of desirable features when compared to standard models based on techniques developed for laminated fibrous materials:

- ✓ Several cord layers may be represented within one single element without inducing any additional discretization error. This makes the use of rebar model particularly efficient in large scale 3D analyses.
- ✓ Experimentally obtained material parameters of the individual components may be used directly as input parameters for the analyses.
- ✓ The (true) stress state is obtained separately in the different plies and in the stitching material, respectively.

The geometry of the rebar model is defined in the context of three-dimensional isoparametric elements, characterized by the map;

$$X_e^h = \sum_{A=1}^{N} N_A(\xi) X^A \qquad (18)$$

Where X_e^h, X^A are the interpolated and the nodal coordinates in the reference configuration, respectively, $N_A(\xi)$ are the shape functions, and $\xi^T = [\xi, \eta]$ are the natural coordinates in the isoparametric domain and *N* is the number of nodal points in the element. Figure 89(a) contains the geometry of the cord layer in the host element, while Fig. 89(b) illustrates the corresponding configuration in the isoparametric mapping. The numbers 1, 2, 3, 4 denote the integration points in one layer. The spatial position and direction of the rebar fibers is defined for each layer in the isoparametric domain at η integration points by the values ξ_n and T_n.

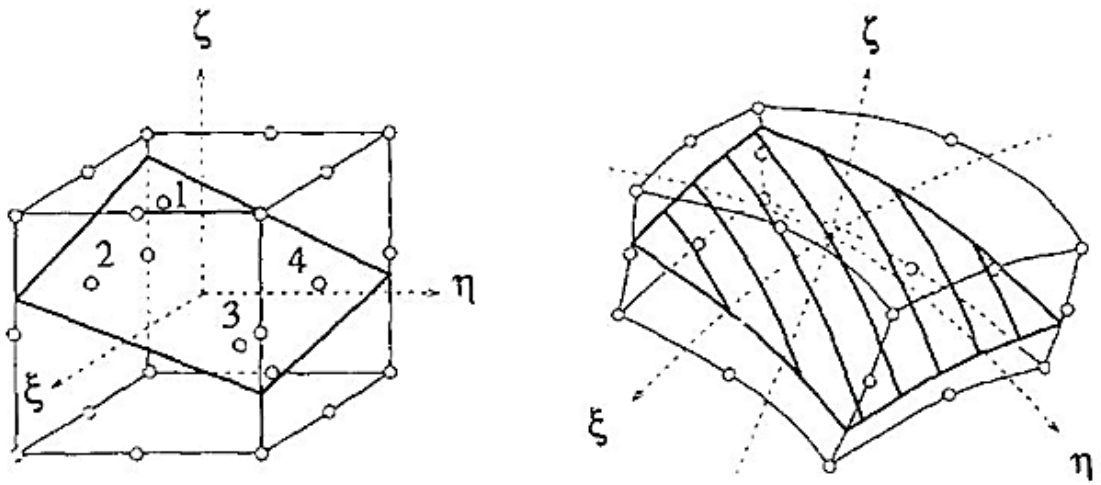

Figure 89 : Typical rebar layer in a 20-node isoparametric element. (a) Geometry in the host element, (b) Geometry in the isoparametric domain.

Which are input by means of a subroutine ξ_n denotes the distance of the rebar fiber

from the middle surface of the element at each integration point *n.* The spatial position of a rebar layer within the element is then defined by the shape functions $N_{r,R}$ as;

$$\xi_R(\xi, N) = \sum_{A=1}^{N} N_{A,R}(\xi, \eta)\xi_A \tag{19}$$

In the present context, the geometry of a rebar layer is approximated by a bilinear form defined in the isoparametric parent element, with the natural coordinates of the integration points.

$$\xi = \pm \frac{1}{\sqrt{3}}, \quad \eta = \pm \frac{1}{\sqrt{3}} \tag{20}$$

And the shape functions $N_{r,R}$ given as;

$$N_{1,R} = \frac{1}{4}\left(\sqrt{3}\xi - 1\right)\left(\sqrt{3}\eta - 1\right), \qquad N_{2,R} = -\frac{1}{4}\left(\sqrt{3}\xi + 1\right)\left(\sqrt{3}\eta - 1\right)$$
$$N_{3,R} = \frac{1}{4}\left(\sqrt{3}\xi + 1\right)\left(\sqrt{3}\eta + 1\right), \qquad N_{4,R} = -\frac{1}{4}\left(\sqrt{3}\xi - 1\right)\left(\sqrt{3}\eta + 1\right) \tag{21}$$

3.3.3. Laminate Mechanical Response

The basic theory to determine the stress distribution in this case is according to classical lamination theory. The force per unit width (N_i) according to this theory is expressed as :

$$\begin{cases} N_x = A_{11}\epsilon_x + A_{12}\varepsilon_y + A_{16}\gamma_{xy} \\ N_y = A_{12}\epsilon_x + A_{22}\epsilon_y + A_{26}\gamma_{xy} \\ N_{xy} = A_{16}\epsilon_x + A_{26}\epsilon_y + A_{66}\gamma_{xy} \end{cases} \tag{22}$$

Where A_{ij} is the laminate stiffnesses, and ε and γ denote normal and shear strains.

For a uniaxial loading in the x-direction (longitudinal direction of test specimen), the

above equation give:

$$\begin{cases} N_x = A_{11}\epsilon_x + A_{12}\varepsilon_y + A_{16}\gamma_{xy} \\ 0 = A_{12}\epsilon_x + A_{22}\epsilon_y + A_{26}\gamma_{xy} \\ 0 = A_{16}\epsilon_x + A_{26}\epsilon_y + A_{66}\gamma_{xy} \end{cases} \quad (23)$$

There, the longitudinal modulus of a test specimen under uniaxial tension can be reduced to read:

$$E_x = \frac{1}{n_p h_0}\left(\frac{N_x}{\varepsilon_x}\right) = \frac{1}{n_p h_0} = \left(A_{11} - \frac{A_{12}^2 A_{66} + A_{66}A_{16}^2 - 2A_{12}A_{16}A_{26}}{A_{22}A_{66} - A_{26}^2}\right) \quad (24)$$

Where h_0 is the thickness of a lamina and n_p is the total number of plies.

The stiffenesses A_{ij} is related to the equation below.

$$(A)_{ij} = \sum_{k=1}^{n}. \ Q_{ij}{}^{1}{}_{k} \ (h_k - h_{k-1}) \quad (25)$$

Where $(Q)_{ij}{}^{1}$

$$Q_{11}{}^{1} = Q_{11}m^4 + 2[Q_{12} + 2Q_{66}]\ n^2\ m^2 + C_{22}n^4 \quad (26)$$

$$Q_{12}{}^{1} = [Q_{11} + Q_{66} - 4Q_{66}]\ n^2\ m^2 + Q_{12}\ (\ n^4 + m^4] \quad (27)$$

$$Q_{16}{}^{1} = [Q_{11} - Q_{12} - 2Q_{66}]\ n\ m^3 + (Q_{12} - Q_{22} + 2Q_{66}]\ n^3\ m \quad (28)$$

$$Q_{22}{}^{1} = Q_{11}n^4 + 2[Q_{12} + 2Q_{66}]\ n^2\ m^2 + C_{22}\ m^4 \quad (29)$$

$$Q_{26}{}^{1} = [Q_{11} - Q_{12} - 2Q_{66}]\ n^3\ m + [Q_{12} - Q_{22} + 2Q_{33}]\ n\ m^3 \quad (30)$$

$$Q_{66}{}^{1} = [Q_{11} + Q_{22} - 2Q_{12} - 2\ Q_{66}]\ n^2\ m^2 + Q_{66}\ [n^4 + m^4] \quad (31)$$

In this series of equation, m = cos(θ) and n = sin(θ), where θ denotes the angle between the x direction at off-xis and on-axis and h_k is the distance from the mid-plane of the laminate.

3.3.4. Three dimensional and Elements Modelling

Figure 90 shows three dimensional and elements modelling. For the element modelling, the laminate was modelled using an 8-node quadrilateral in-plane continuum shell with hourglass control and multiple elements in the thickness direction, which improves the performance of the elements in bending. The stitching was modelled using 3D stress 8-node linear bricks with hourglass control.

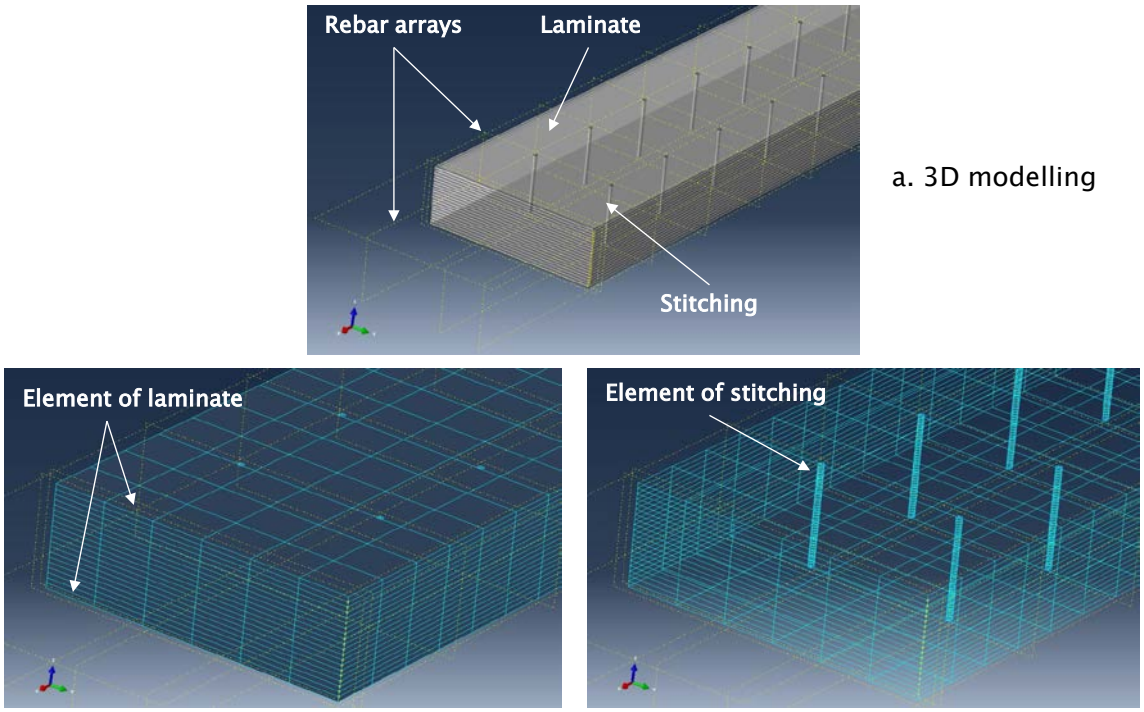

a. 3D modelling

b. Element Modelling of laminate

c. Element modelling of stitching

Figure 90 : Three-dimensional and elements modelling of stitched laminated material.

3.3.5. Numerical Result

Figure 91 shows the stress distribution results within the laminate in each group of orientation layers and the stress magnitude can be seen in Table 1. By using rebar

technique, we can retrieve stress distribution data in each layer separate with stitching stress reaction and used it as inputting data to the first ply failure formulation. Then the data can be used to determine preferred area for FBG sensor installation, while Fig.92 shows the stress distribution results within the selected stitched region only as a result of stress reaction caused the laminate displacement.

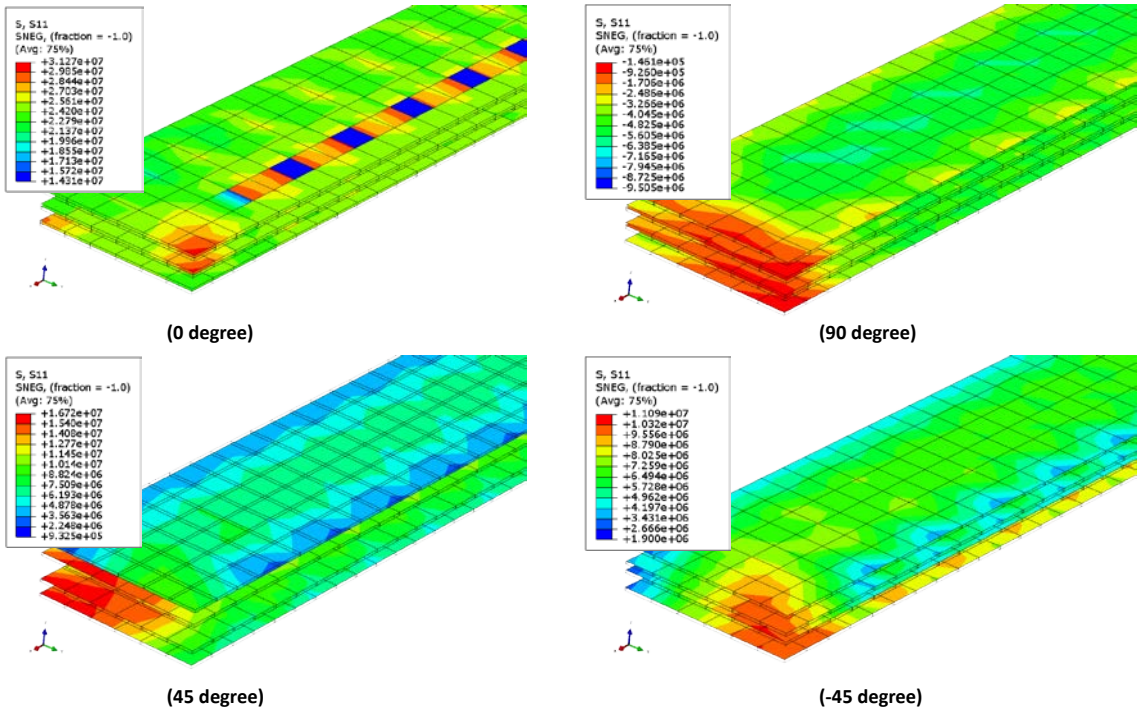

Figure 91 : Off-axis stress distribution within laminate.

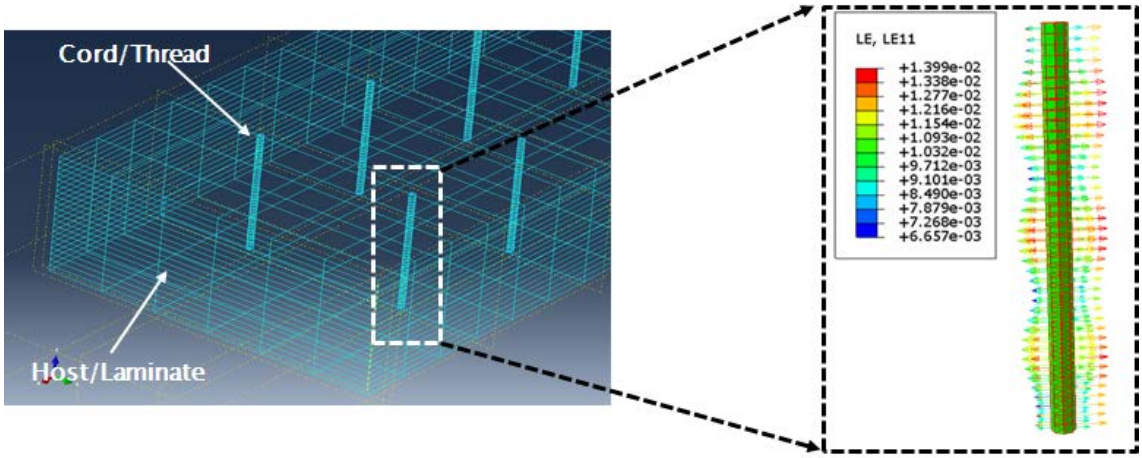

Figure 92 : Stress distribution within stitched region.

Table 1. Stresses magnitude between plies

Orientation Layer	σ_{11} (MPa)	σ_{22} (MPa)	σ_{12} (MPa)
45^0	133.9	16.08	-12.61
90^0	-86.11	29.25	0
-45^0	133.9	16.08	12.61
0^0	353.9	2.918	0

The Tsai-Hill failure criterion, an interactive maximum stress criterion, can be applied to the above results to determine which ply failed first. It predicts failure when any one of the ultimate (yield) strength values exceeds the corresponding allowable stresses in a principal axes direction. Thus, to ensure a safe design, the following inequalities must be satisfied in both tension and compression.

$$(\sigma_{11}|X)^2 + (\sigma_{11}|Y)^2 - (\sigma_{11}\sigma_{22}|X^2) + (\sigma_{12}|S)^2 = 1 \qquad (23)$$

Where the quantities X and Y are the tensile and compressive yield strengths of the material, respectively, and S is the corresponding shear strength. The values of allowable strength mentioned in Chapter 4.3.1 are used in the analysis. We may then draw the conclusion that the first failure group occurred at 90^0 in approx., 629N/mm, the second failure group at $\pm 45^0$ groups in approx., 1110N/mm and the third failure at 0^0 in approx., 2659N/mm. Therefore, the FBG sensor was placed between Ply 8 and Ply 9 to acquire as much spectrum data as possible before the total failure of the specimen.

3.4. Material and Specimen Preparation

3.4.1. Fabric Preform and VaRTM Preparation

Figure 93 shows a VaRTM technique illustration during stitched laminate material fabrication. The type of stitching used in this study is the modified lock stitch which avoids disruption to the laminate from any interior looping processes between the bobbin and needle threads; it is also easier to observe the interlock region between the needle and bobbin thread at the face of the laminate. The fabrication of dry preforms of T800SC-24K involves the lay-up and selective stitching of fabric layers with Vectran HT threads by Kuraray Industries Corporation, A 400-denier Vectran HT thread was selected for the needle threads and for the bobbin. The selective stitching process was

done in a Toyota Industries Corporation using their patented machine with a working platform capable of handling up to 30- x 30- x 2-cm preforms. Bleeder plies were placed at the center where vacuum ports were to be located. A rectangular steel frame covered with a porous ply was inserted to keep the vacuum ports and the bleeder plies apart to avoid resin flow into the two vacuum ports. Airweave breathers were used to cover the top side, and the entire assembly was vacuum bagged with a sealant tape then a leak test was performed. And after the stitching process, the resin transfer molding technique, at a curing temperature of 180^0C, was used to consolidate the composite. The epoxy resin used in this case is RTM6 made by Hexcel.

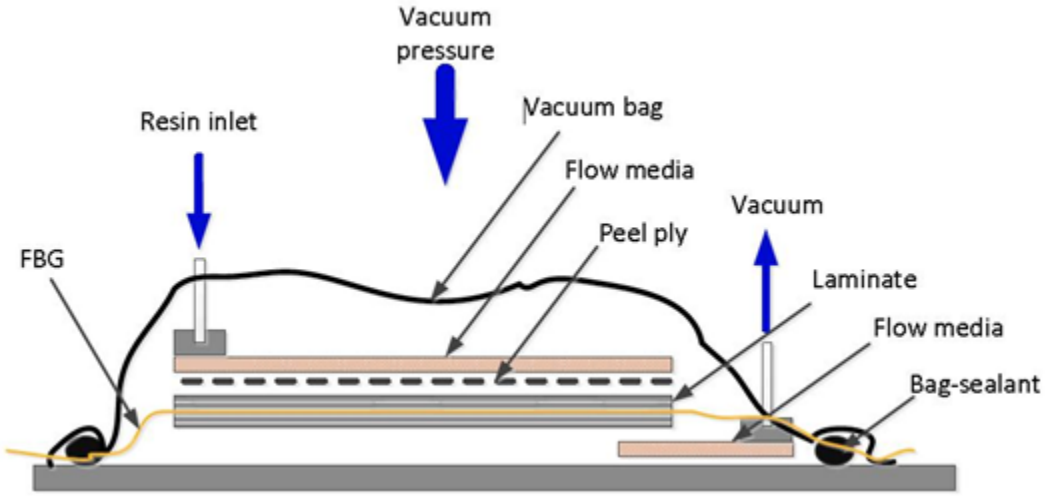

Figure 93 : VaRTM sketch.

3.4.2. FBG Sensor Installation

Figure 94 shows the position of FBG sensor as result of FEA scenario where an

FBG sensor was embedded in the interface between ply no.8 (90^0) and ply no.9 (45^0) as explained in numerical scenario in the previous chapter. Figure 95 shows detail position of FBG sensor in micro-structure photo. The FBG had a grating span of 15 mm and was made using Fujikura Optical Fiber with Ø 125 μm.

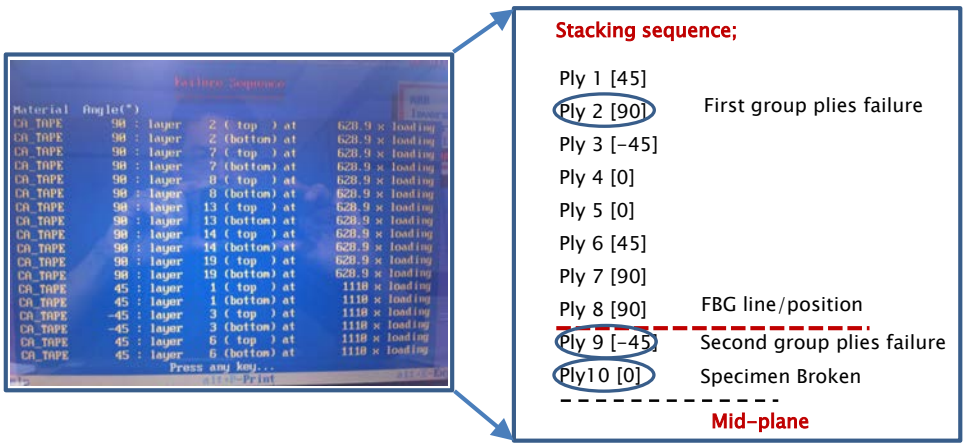

(a)

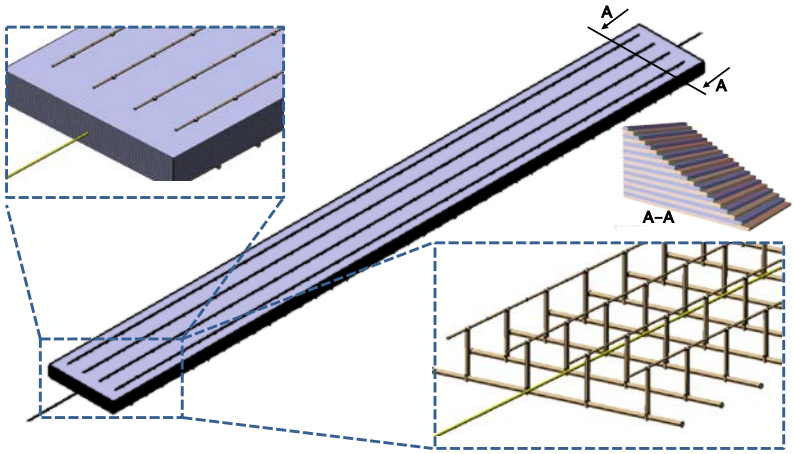

(b)

Figure 94 : FBG placement within stitched laminate material. (a) First ply failure theory result, (b) FBG position illustration within stitching configuration.

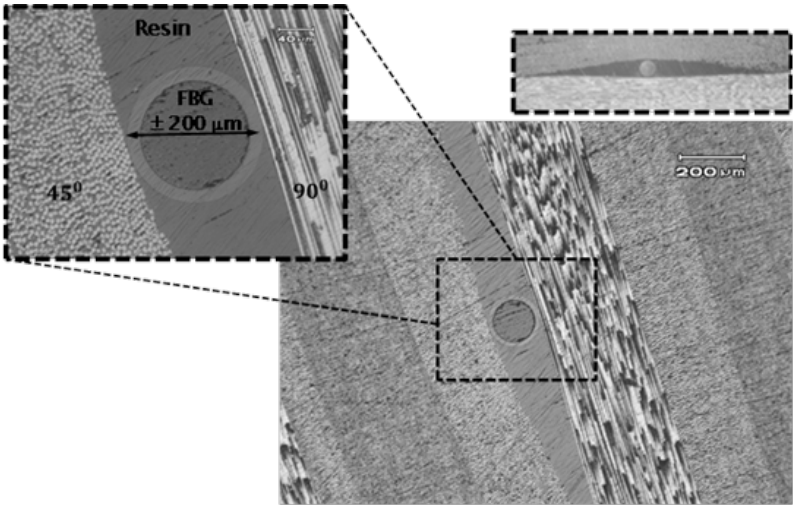

Figure 95 : The micro-structure photo of FBG sensor installation into the specimen.

3.5. Testing and Damage Evaluation Procedure

3.5.1. Tensile test

Figure 96 presents the experimental arrangements. The tensile test was conducted using a universal testing machine (Instron 8802). The crosshead speed was 1 mm/min for the FBG sensor and AE test profiling until the specimen experienced total failure. The crosshead speed on the interrupt load test was 0.5 mm/min to acquire more data. The span length of the tensile test was 130 mm. A non-contact strain sensor, an advanced video extensometer (AVE), was used to monitor the axial strain behavior on the stitched laminate specimen to clarify the accuracy of the universal testing machine. The spectrum reflection was continuously measured until the specimen broken. After that point, an interrupted test at a certain load interval was conducted to observe the

damage growth. The specific load for the interrupted test was chosen based on the load-displacement curve and from the changes in the spectrum reflection, which indicated that damage had initialized. The loading-unloading test was used to represent real conditions when the damage occurs in aircraft structures. The evolution of the shape of the reflected spectrum was observed using a spectrum analyzer, and damage was observed using an ultrasonic C-scan (Gsonic Scan 6A x 600).

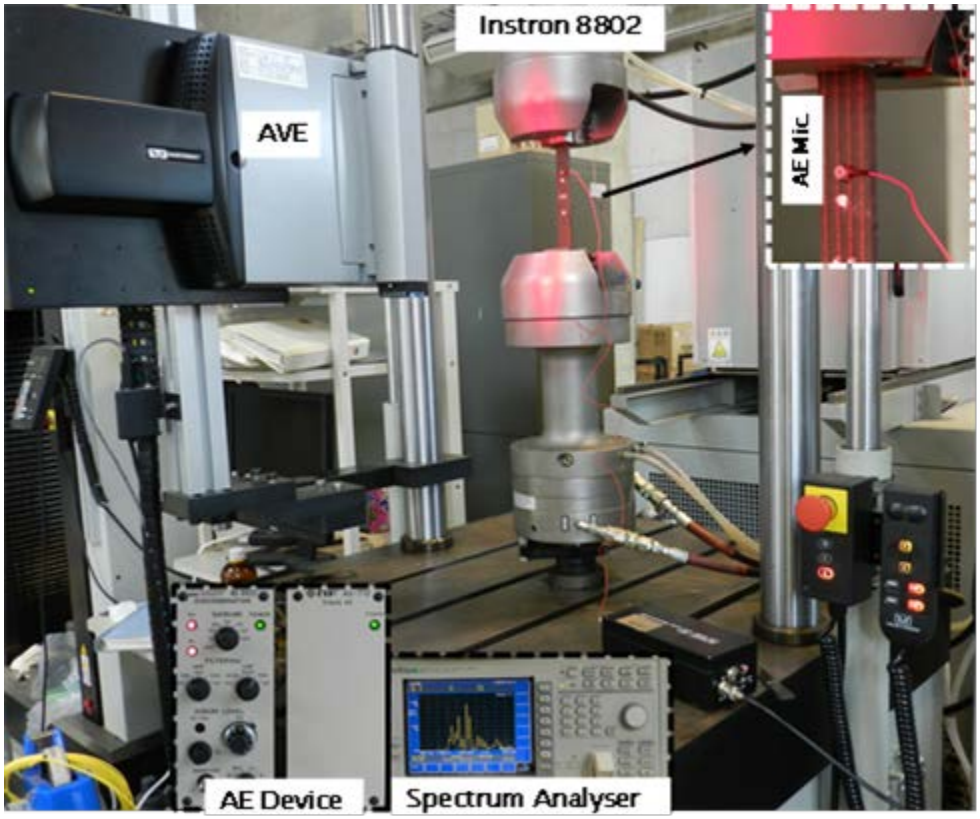

Figure 96 : Tensile, AE, and Spectrum Analyzer test setups.

3.5.2. Ultrasonic C-scan test

Figure 97 shows the setting of the ultrasonic C-scan inspection for the damage quantification after conducting a mechanical test. As is commonly done, the distance between the transducer and the material (water path) was set at the end of the near field value of the transducer that was used (which is 25 mm) to avoid the fluctuation of the acoustic pressure that takes place in the near field zone. A steel plate, on which the specimens were placed, was used as a reflective plane to distinguish the backwall echo from any other echos. A linear Distance Amplitude Correction (DAC) curve was used to increase the ultrasonic signal amplitude, thus reducing the causes of the signal losses to factors such as scattering, absorption, etc. The gates were synchronized with the first echo from the specimen, and the detection threshold was adjusted to a value that was greater than 50% of the Full Screen Height (FSH), avoiding the generated noise echoes.

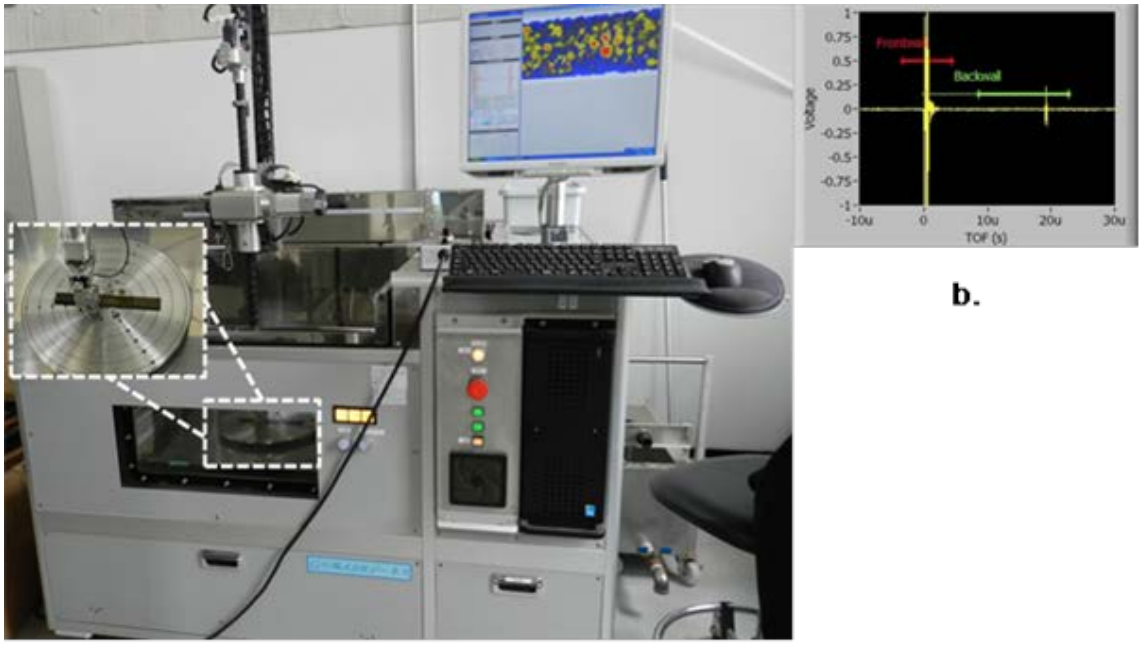

Figure 97 : Ultrasonic C-scan inspection.

3.5.3. Acoustic emission test.

Figure 98 shows AE Graph characteristic which it used as setup reference. It is relatively simple to attach an AE sensor to a composite material and then load the sample. In general, AE sensors respond to deformation (stress) waves in a complex fashion which involves both normal and in-plane deformations and velocities in the test samples. The key information required is the AE signal propagation loss which occurs with distance in the composite structure as a function of the electronic bandpass. This information can be gathered by using pencil-lead breaks right next to the AE sensor and at various distances and directions from the sensor. Once the propagation characteristics of the selected bandpass have been determined, then it is necessary to decide how much

signal propagation loss is acceptable. Since the peak amplitude is one characteristic that has been used to judge the severity of the damage mechanism which caused an AE event in a composite, it may be necessary to limit potential amplitude propagation losses to no more than 6-12 dB, gain AE preamplifier is 40dB, maximum output voltage is 10 volts peak-to-peak and dynamic range minimum is greater than 60 dB.

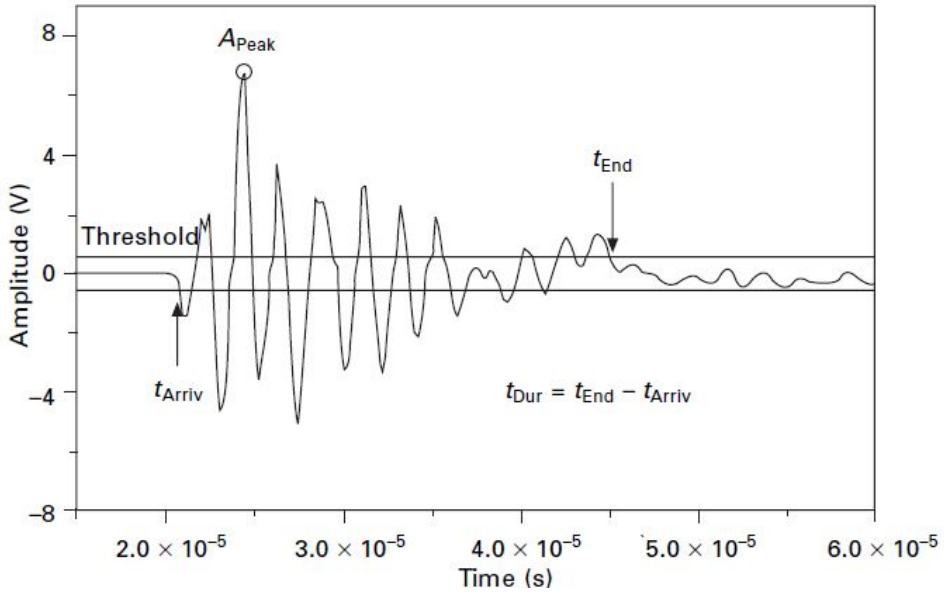

Figure 98 : AE graph characteristic.

3.5.4. Fiber Bragg grating sensor test

Figure 99 shows joining FBG sensor to fiber optic from a broadband light source by using a Fujikara arc splicer and bias light calibration after joining process was done. This process performed before static test start. The losses after the fiber optic joining were 0.00 dB, indicating a perfect joining result. During the static test, the FBG sensor was lit with a broadband light source (ASE FL7002, 1530-1610 nm, FiberLabs). The

power spectrum was measured from the reflected light in the FBG sensor, which it was embedded in the stitched laminate material.

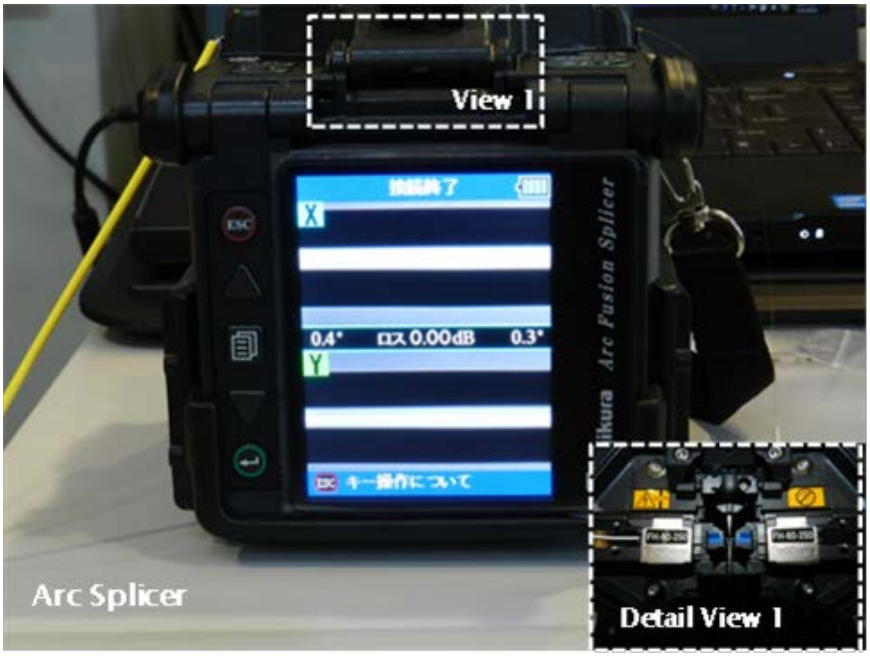

Figure 99 : FBG sensor joining and the losses dB calibration.

3.6. Results and Discussion

3.6.1. Experimental Results.

3.6.1.1. Stitched laminate material.

Figure 100 shows mechanical load-strain graph in 6x6 Vectran stitched laminate material. This graph combined with acoustic emission test and ultrasonic C-scan inspection will used to determine interrupt loading test to characterize the damage progression behavior and quantifying the damage during load.

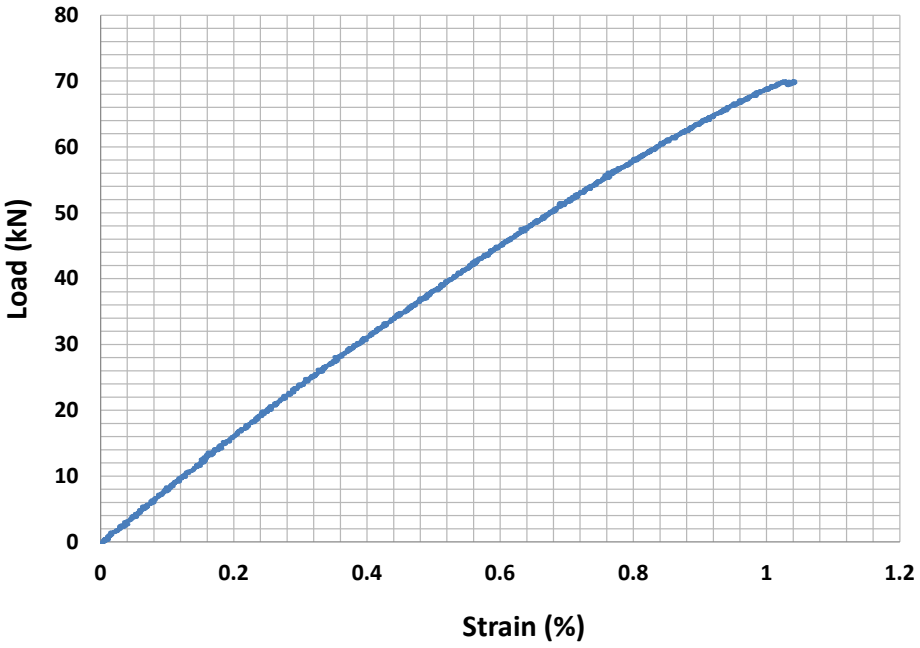

Figure 100 : Load- strain behavior of stitched laminate material.

3.6.1.2. Acoustic emission result

Figures 101-102 show the load-strain graph combined with the acoustic emission result. A hit is as a result of transient energy wave generated by damage growth inside the stitched laminate specimen in the acoustic emission test. Certain load position chosen as interrupt load based on significant spike happened and multi-peak of power spectrum occurred, while Figs.103-104 indicates that energy-load graph and hit-load graph have same trend and almost the same value. It was explained that AE test shows that setting value to calculate the energy wave generated by damage growth and spectrum hit the threshold given was correct.

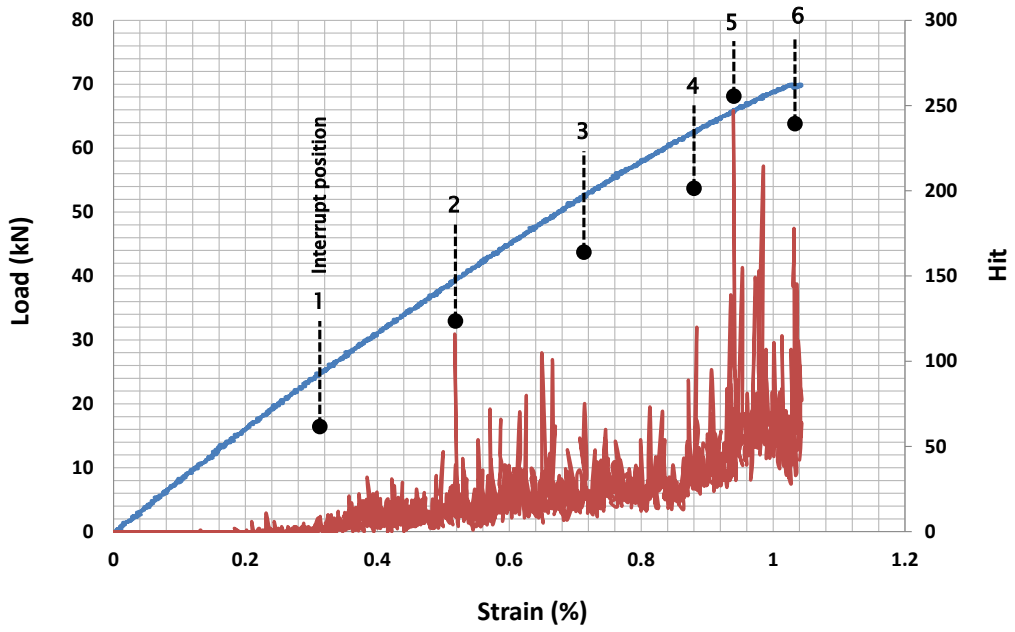

Figure 101 : Mechanical behavior versus AE-Hit of stitched laminate material.

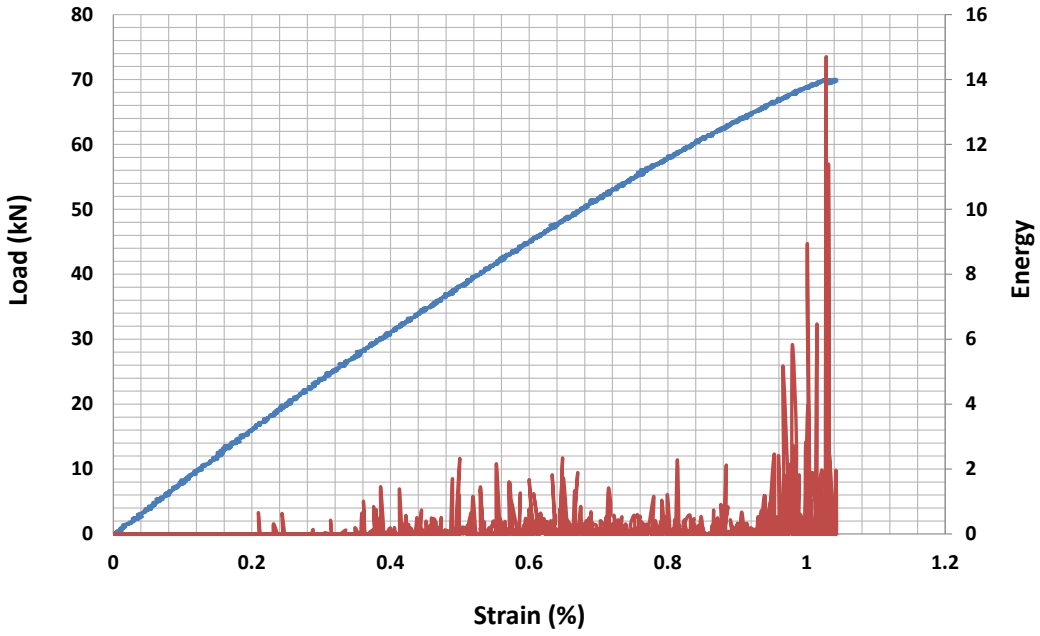

Figure 102 : Mechanical behavior versus AE-Energy of stitched laminate material.

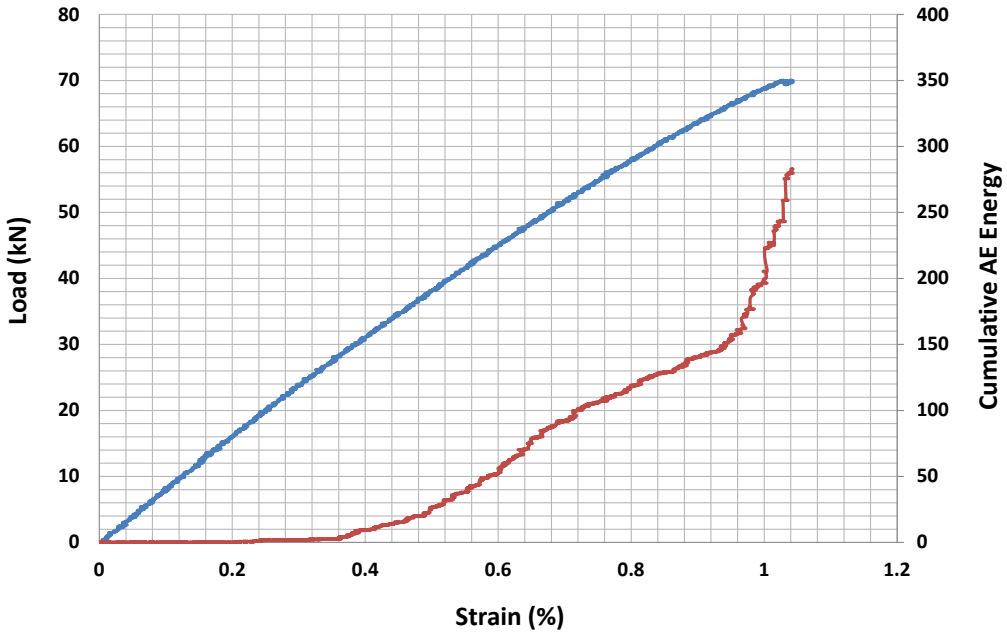

Figure 103 : Mechanical behavior versus AE-Cumulative Energy of stitched laminate material.

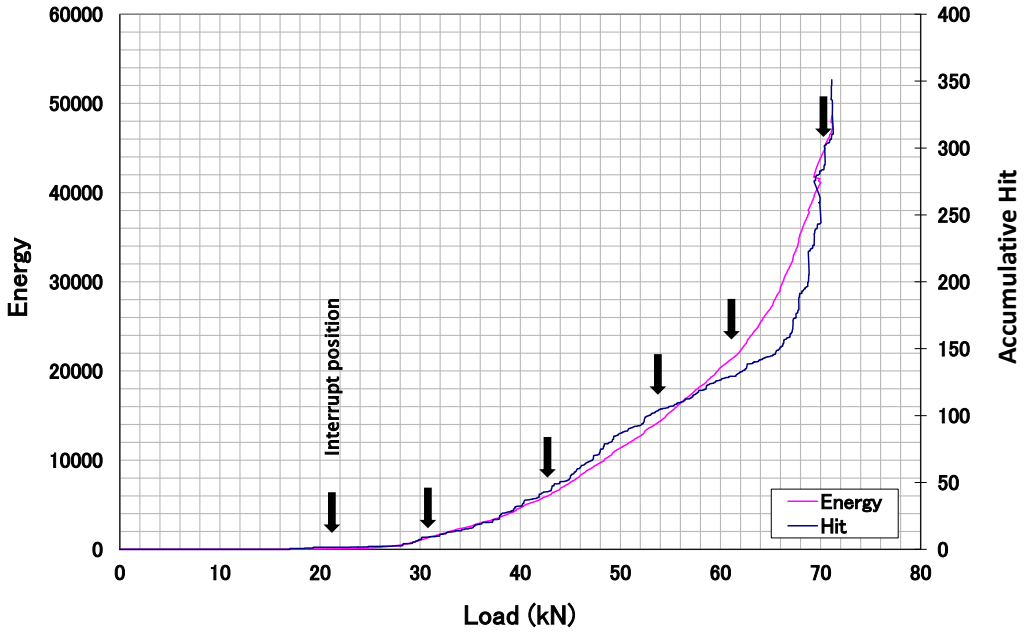

Figure 104 : Comparison result between energy and accumulative hit under AE test.

3.6.1.3. Ultrasonic C-scan result.

Figures 105-107 show ultrasonic C-scan inspection results before loading which it as original condition from the manufacturer. Two projection view provided in the right and bottom side from surface/main view to reflect the damage condition inside the stitched laminate specimen in detail. Theoretically, no damage occurred in original specimen, but here clearly seen the damage appeared started as long the location of FBG sensor placement as shown in red-color in the C-scan inspection result. One of the reasons is the compatibility of the FBG sensor coating with the resin used. It is important to determine another coating of FBG sensor that suitable with the resin used to avoid the FBG sensor become an impurity in the material system. Therefore, area around the FBG sensor then becomes damaged initiation and develops in the weakest area near there. In the original spectrum within specimen model before loading also can be seen that the spectrum shape is already changed which it show the grading period in FBG sensor is already deformed caused by the manufacturing process.

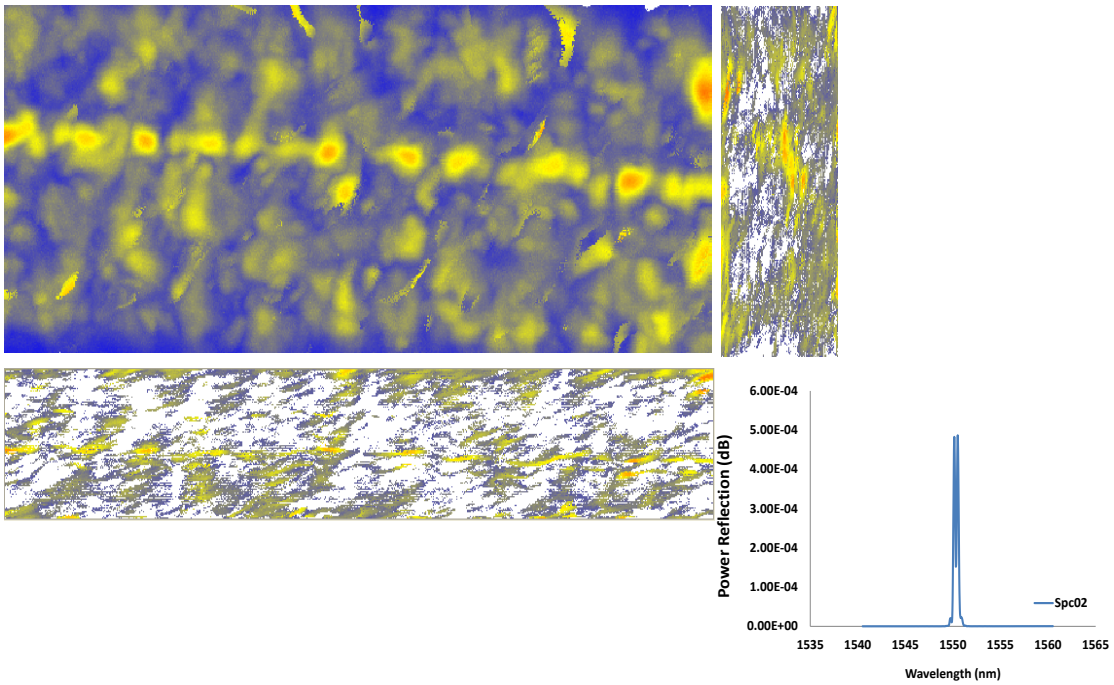

Figure 105 : C-scan result specimen2 compared with own original power spectrum.

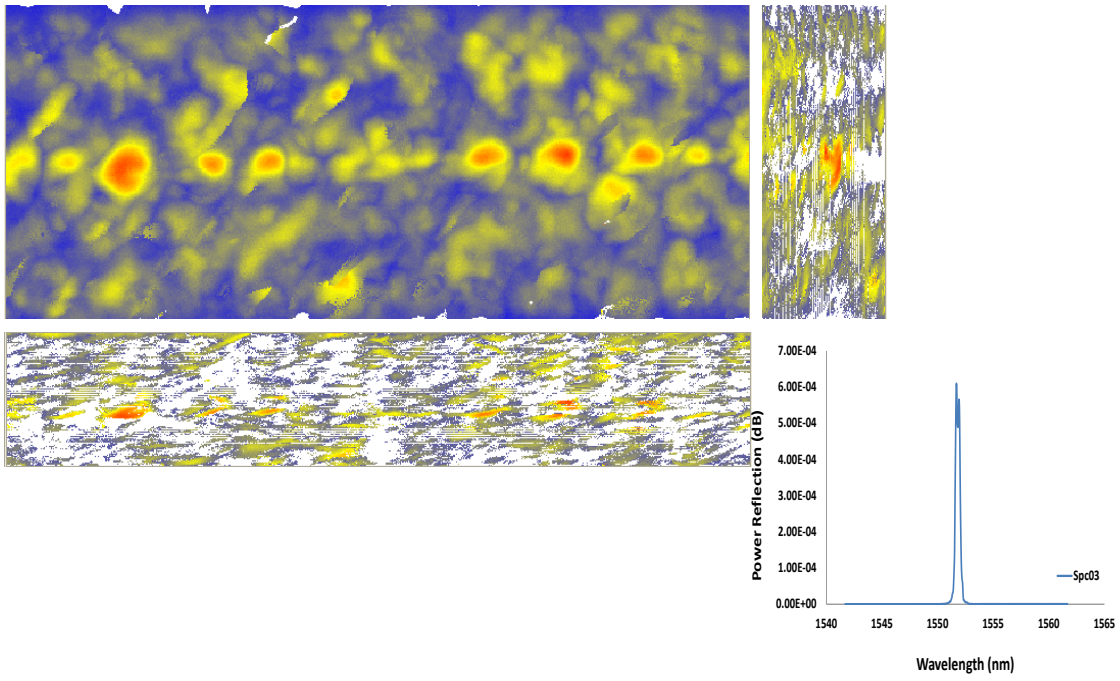

Figure 106 : C-scan result specimen3 compared with own original power spectrum.

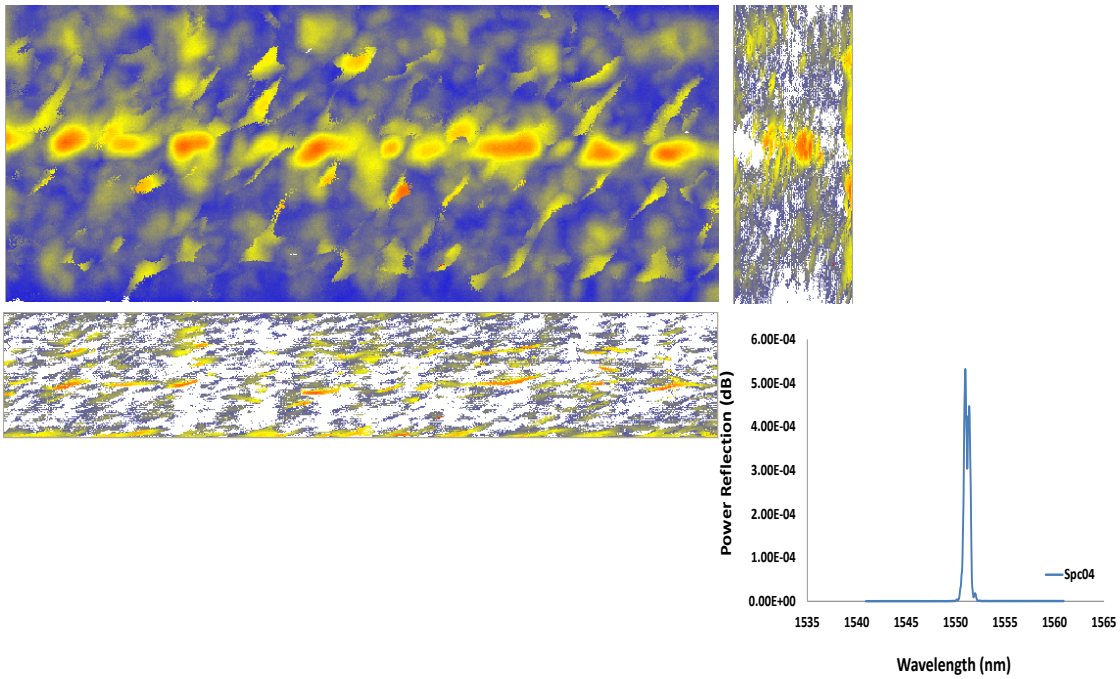

Figure 107 : C-scan result specimen4 compared with own original power spectrum.

3.6.2. The perspective of FBG sensor reading

Figure 108 shows some spectrum evolution which it's important to recognize before discussion power spectrum shape in the following chapter. Start left to right: FBG sensor spectrum in original, spectrum without FBG sensor then the spectrum evolution of FBG sensor when the damage occurred and the last is spectrum evolution with almost all grating periods within the FBG sensor broken which the spectrum pattern goes to pattern without FBG sensor.

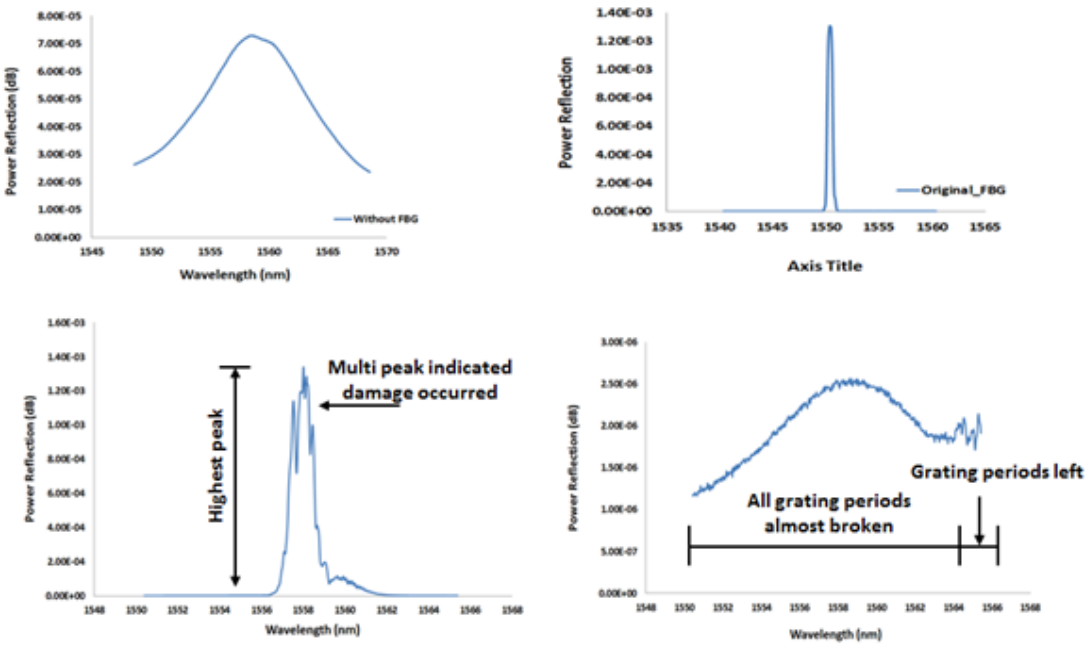

Figure 108 : Spectrum shape evolution under FBG sensor reading in stitched laminate.

3.6.2.1. Power spectrum characteristic under tension loading.

Figure 109 shows the spectrum pattern evolution during the loading run in a tensile test up to the specimen broken. The occurrence of multi-peaks that differ from the original indicate the occurrence of damage. The value has a tendency to decrease gradually until the stitched laminate specimen broken. We can take advantage of this pattern and use the highest peak in each spectrum as an indicator to make graphs and then determine the degradation of the strength of the material. We can then compare the result with a mechanical behavior graph.

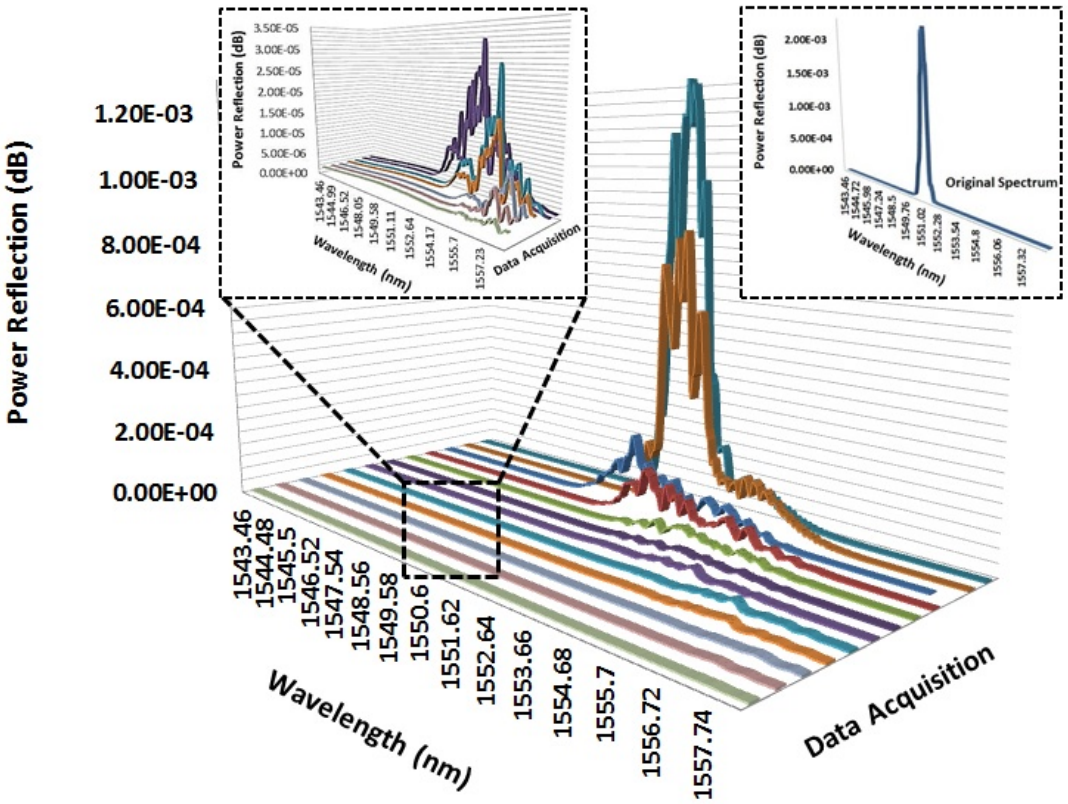

Figure 109 : Spectrum evolution on profiling tensile test.

Figure 110 shows the spectrum evolution during the profiling tensile test in graph form. It then depicts more clearly the decreasing tendency of the power spectrum based on the highest peak value during both the profiling data (until specimen broken) and the interrupt load test (small window in the graph).

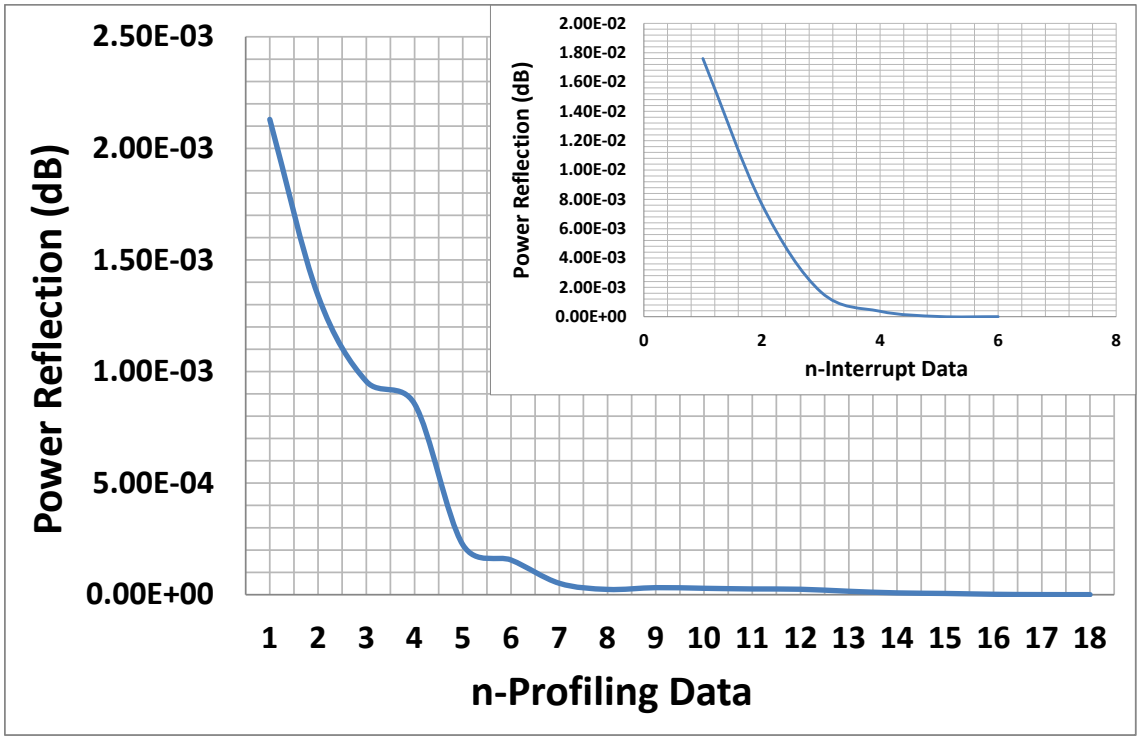

Figure 110 : Highest peak value of the power reflection result in the profiling tensile test compared with the interrupt test.

Figure 111 plots the comparison value between mechanical behavior and the power spectrum. After the strain in the stitch laminate reaches approximately 0.92%, the graph of the spectrum evolution behavior has a gently sloping line, indicating that the grating period of the FBG sensor is almost broken due to severe damage inside the stitched laminate. On the other hand, the mechanical graph does not display the damage existence and growth, indicated by a straight line up until the specimen fails completely.

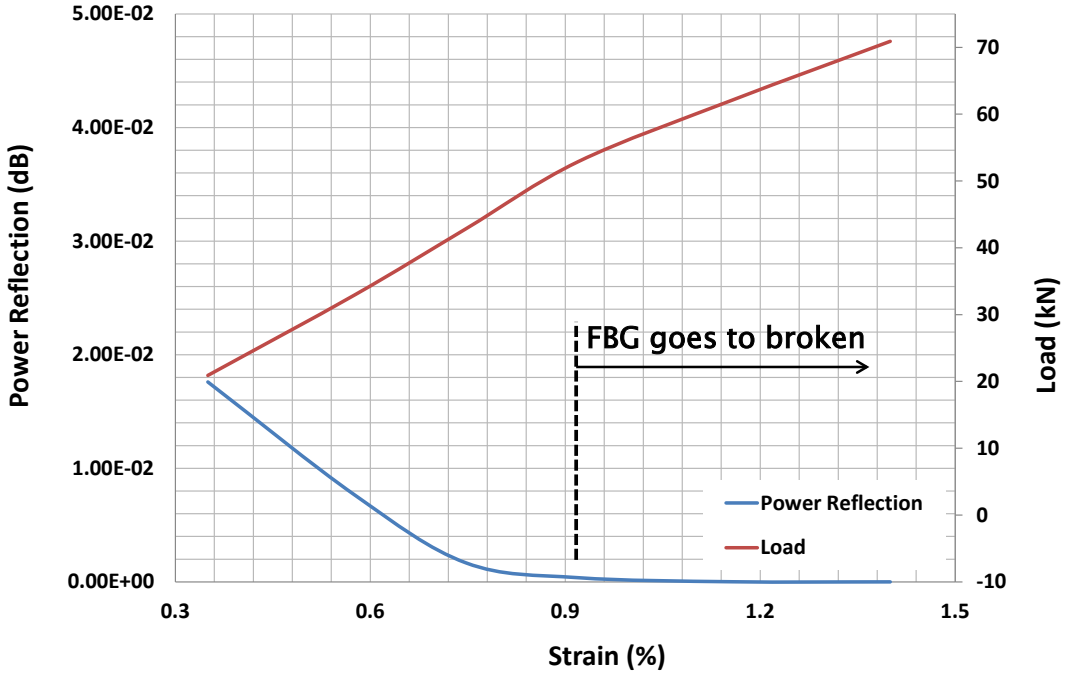

Figure 111 : Power reflection of the FBG sensor reading compared with the mechanical behavior.

Figures 112-113 show the comparative behavior between the FBG sensor reading and the acoustic emission reading. Both graphs feature lines with significant slopes, which is caused by fast damage growth. However, based on the spectrum observed during the test, the spectrum of the FBG sensor was easier to use as damage indicator because only one spectrum was needed to interpret the damage initiation and the growth. In the acoustic emission reading, there were so many spectrums occurred caused by transient energy waves generated by the occurring damage growth.

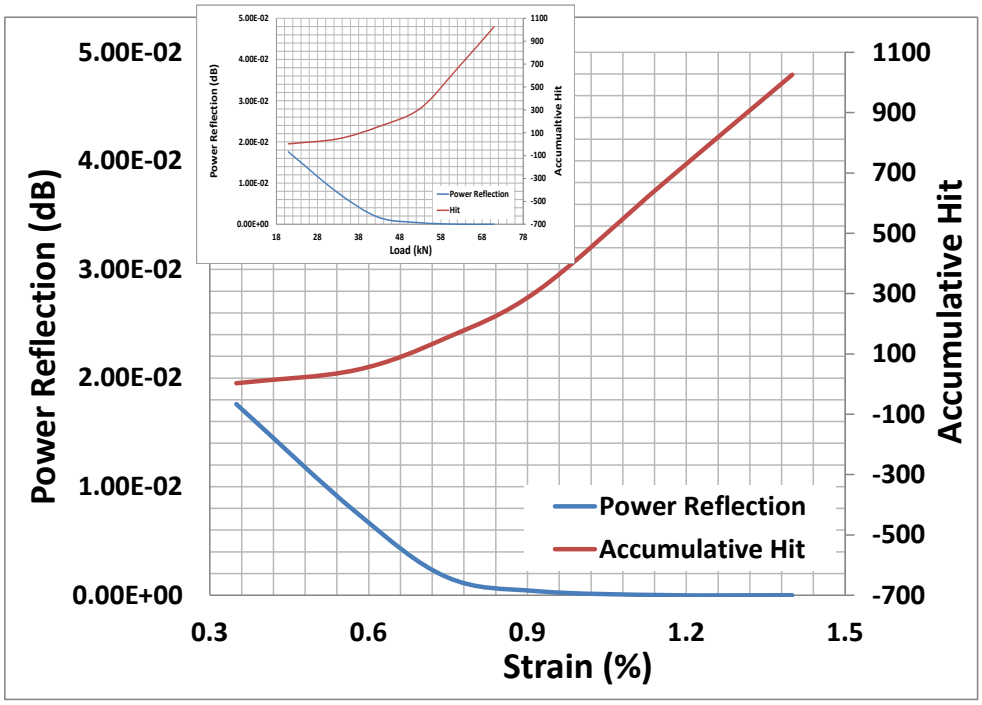

Figure 112 : Power reflection of the FBG sensor reading compared with AE test: accumulative hit characteristic and mechanical behavior.

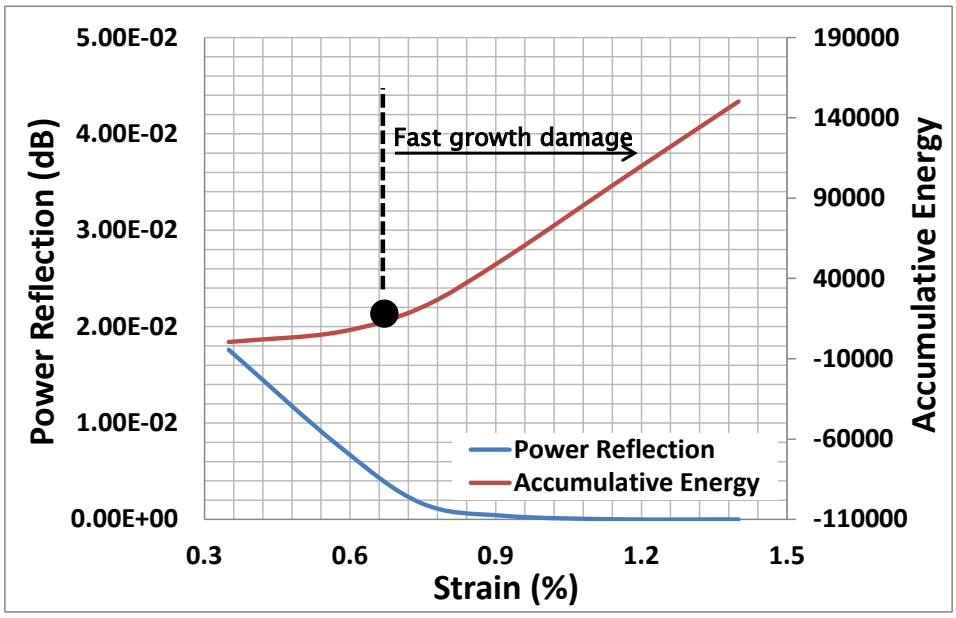

Figure 113 : Power reflection of the FBG sensor reading compared with AE: energy characteristic and mechanical behavior.

3.6.2.2. Power spectrum characteristic under loading-unloading test

Figure 114 shows the spectrum reflection under interrupted load which it indicated consistent pattern with spectrum reflection on profiling test. While Fig.115 shows the spectrum reflection pattern on un-loading condition after interrupted load done. An example of interesting behavior is that the FBG sensor broke at almost the same time as the stitched laminate specimen in unloading spectrum shape6. In that pattern, the spectrum has the same shape as the spectrum without the FBG sensor inside the fiber optic, indicating that the entire grating period was already broken.

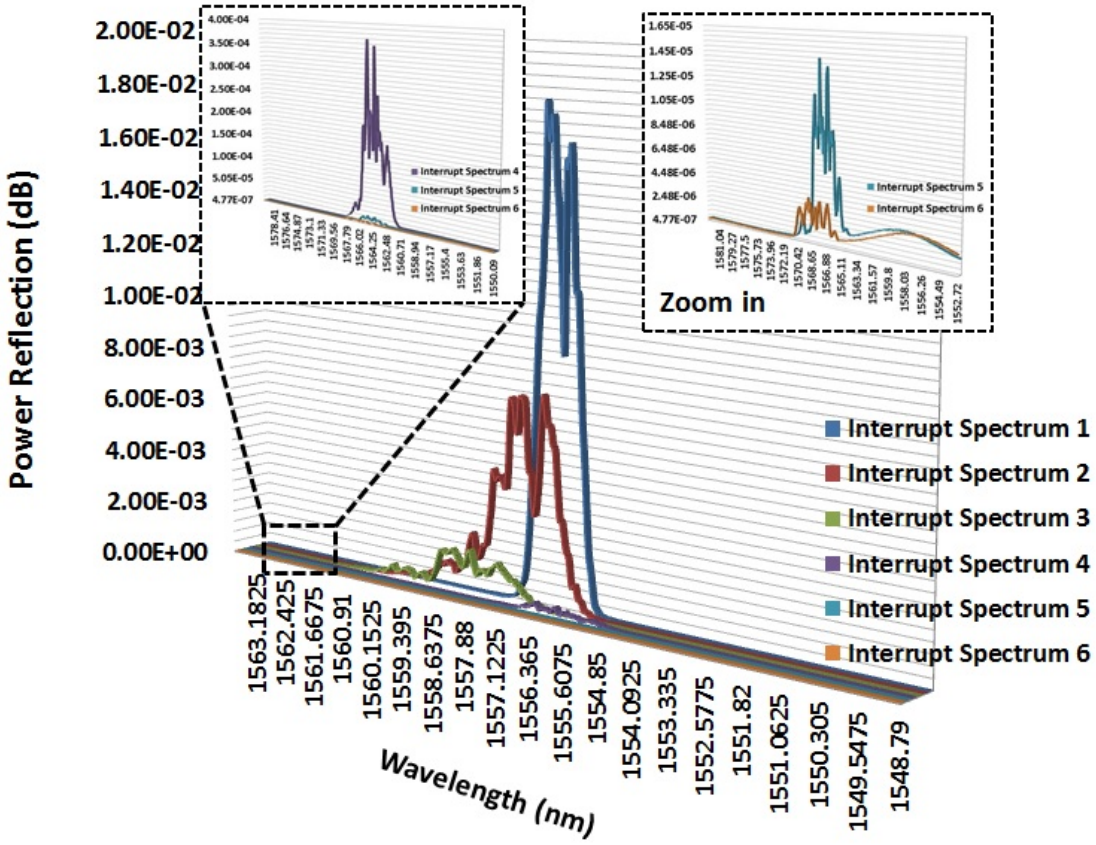

Figure 114 : Spectrum evolution in the interrupt load test.

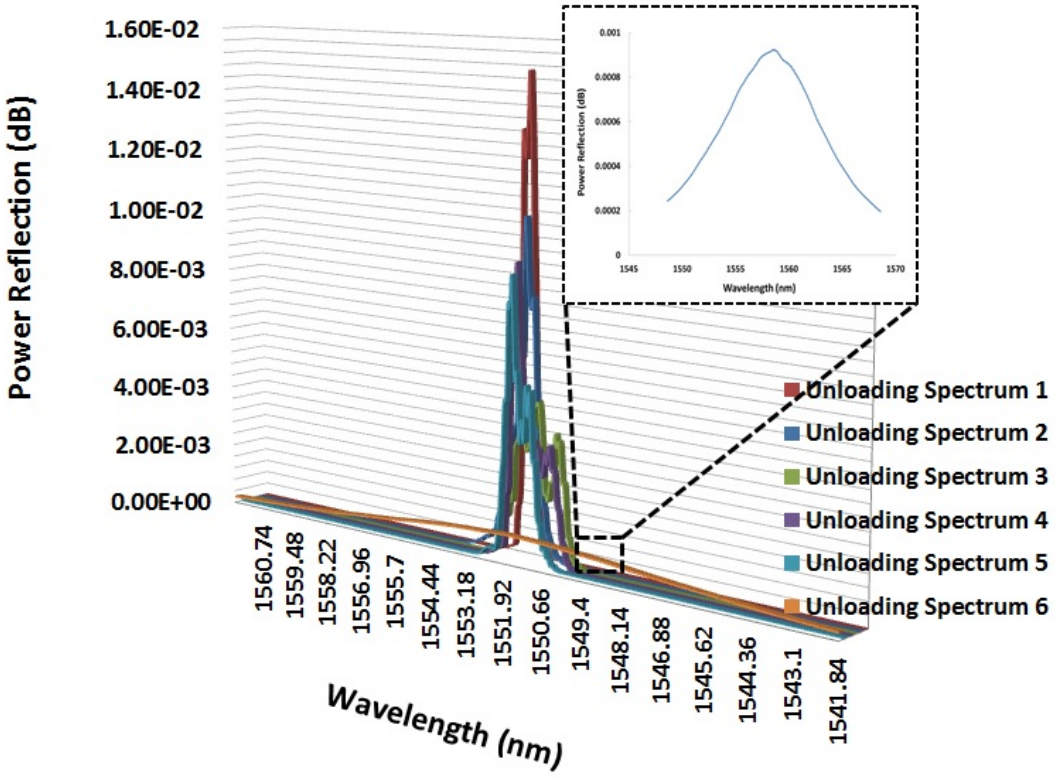

Figure 115 : Spectrum evolution in the unloading data.

3.6.3. Damage quantification.

FBG sensors provide two data readouts in the spectrum analyzer; power reflection and wavelength. The wavelength equation has a linear relationship with the mechanical strain, as indicated by Equations 1 and 2. If the material or structure in which the FBG sensor is embedded suffers damage that causes a non-linear mechanical strain response, Equations 1 and 2 cannot be used. However, if the response through the length of the FBG sensor grating period is still uniform, the linear equations can still be used. The power reflection is used to measure whether the materials or structures have

been damaged enough to cause the FBG sensor grating length to become non-uniform. This measurement is marked by a multi-peak occurrence of the power reflection.

Figures 116 (a) – (f) show the ultrasonic C-scan results from the interrupt load test. Two projection views are provided in the right and at the bottom to reflect the damage condition inside the stitched laminate specimen in detail. Theoretically, the damage will start with ply no. 2 or 90^0 group plies, near the surface, but in this case, the damage clearly initiates at the location of the FBG sensor. One of the reasons this occurs is that the FBG sensor coating was not compatible with the resin used. Thus, it is important to determine another coating of FBG sensor that is suitable with the resin used to prevent the FBG sensor from creating an impurity in the material system. Therefore, the damage that starts in the area near the FBG sensor placement will then develop in the weakest area near that location and start to grow in the area near the surface.

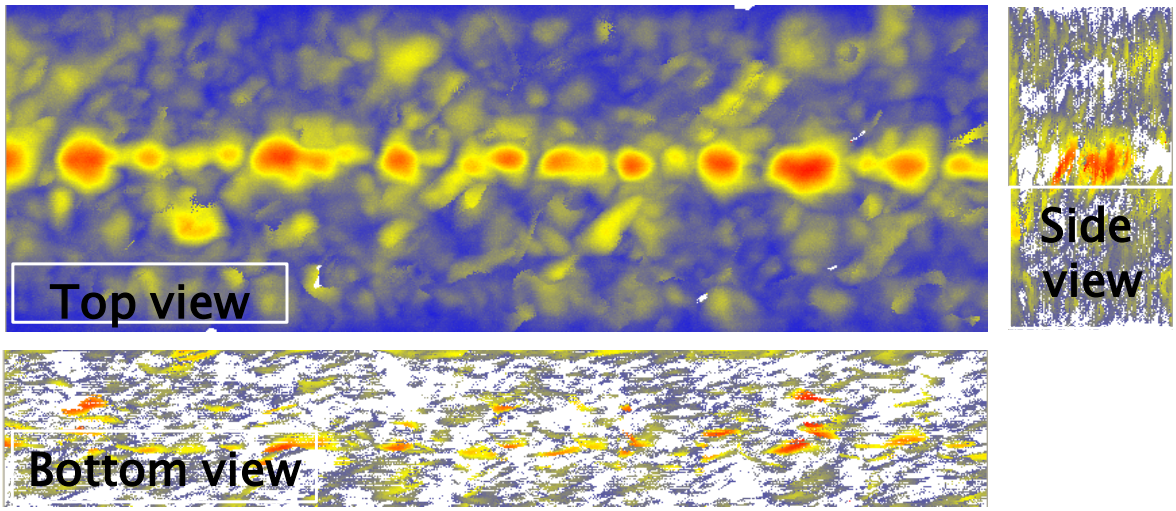

Figure 116 : (a) Interrupt test1, 20kN

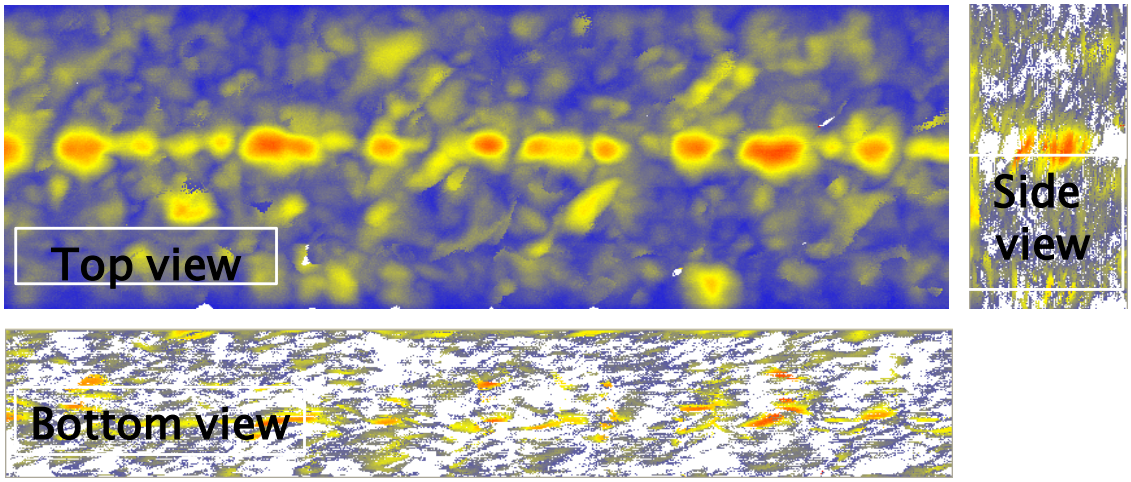

(b) Interrupt test2, 32kN

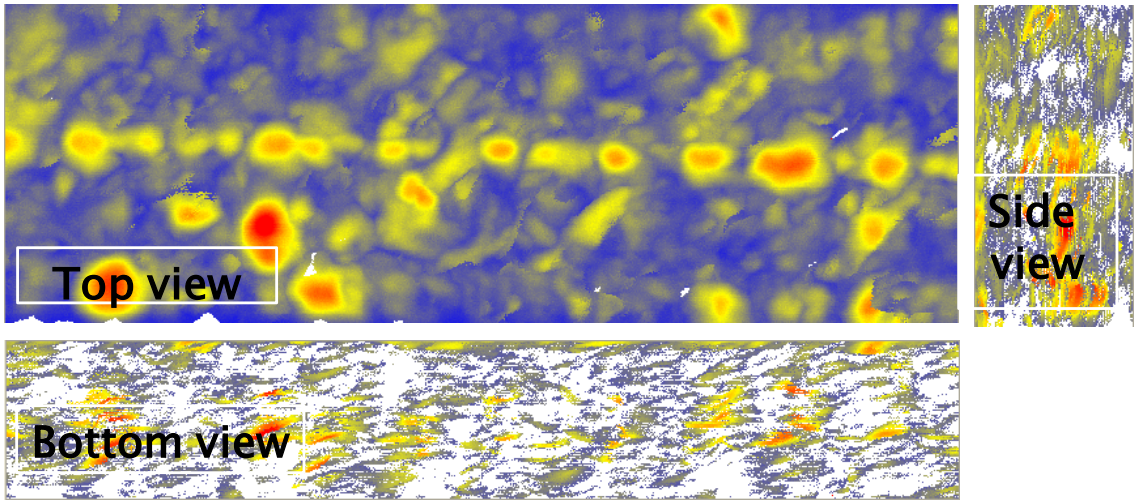

(c) Interrupt test3, 42kN.

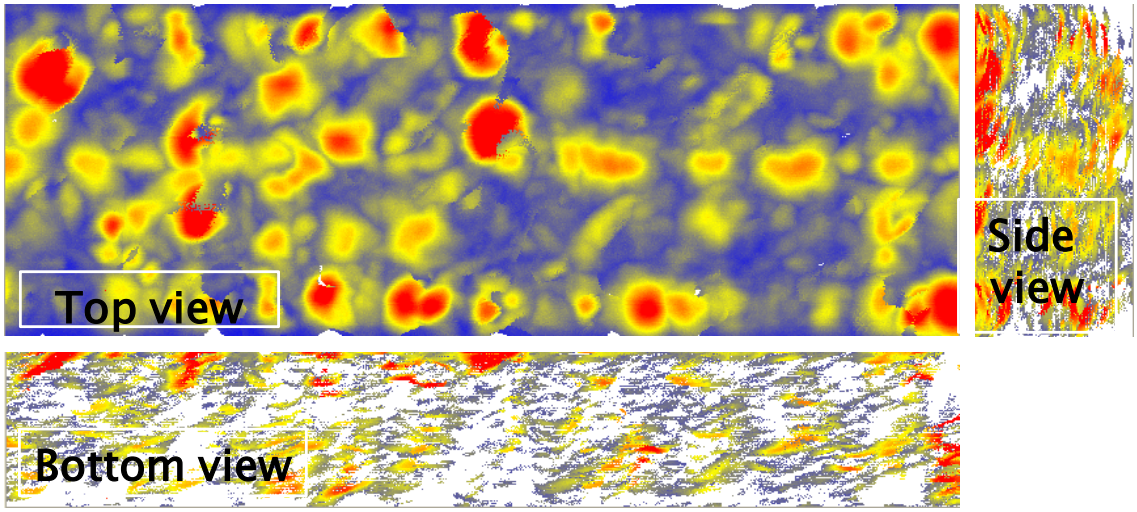

(d) Interrupt test4, 52kN.

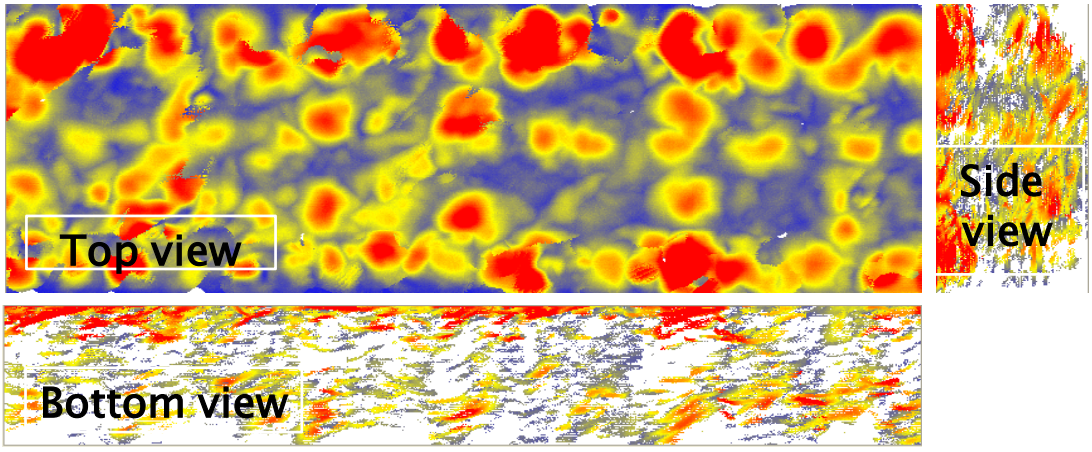

(e) Interrupt test5, 62kN.

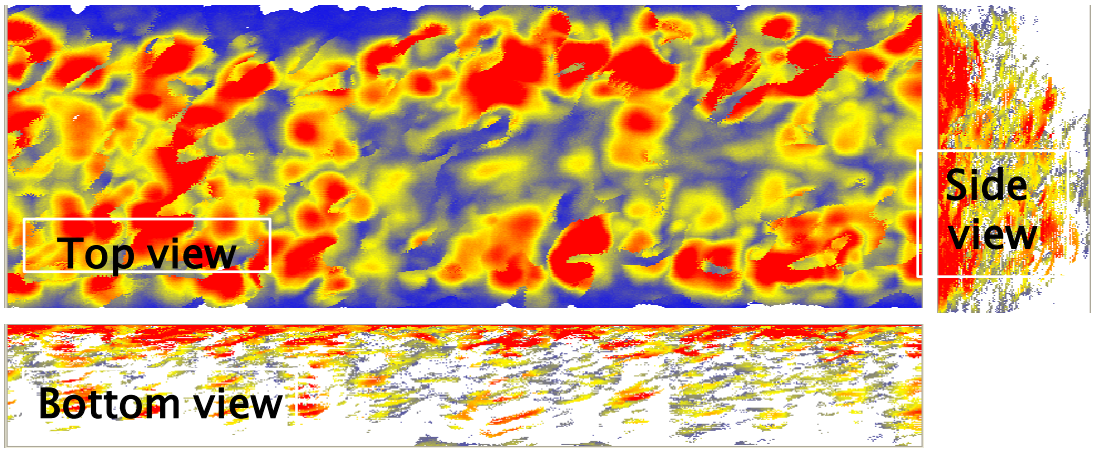

(f) Interrupt test6, 71kN.

Figure 117 shows the damage quantification from the power reflection, the load versus the percentage of damaged area. The graph demonstrates how the multi-peak power reflection occurrence quantifies the damage growth in the specimen under tensile loading. By noting the highest peak after the occurrence of the multi-peak power reflection, we can see a correlation between the multi-peak spectrum and damage growth. Conversely, a steep line on the graph indicated many damage sources in stitched laminate with producing many rich resin area around threads which creates a crack initiation as shown in Fig. 117(b).

Figure 118 shows the power reflection under FBG sensor reading and the accumulative hit under the AE reading versus the percentage of the damaged area. In principal, both techniques can be used to detect and quantify damage, but the FBG sensor technique is superior because only requires a single spectrum to characterize the

damage, while AE depends on the test setting to determine the many spectrums that reach the threshold set during the damage growth. Thus, different test settings may produce different results.

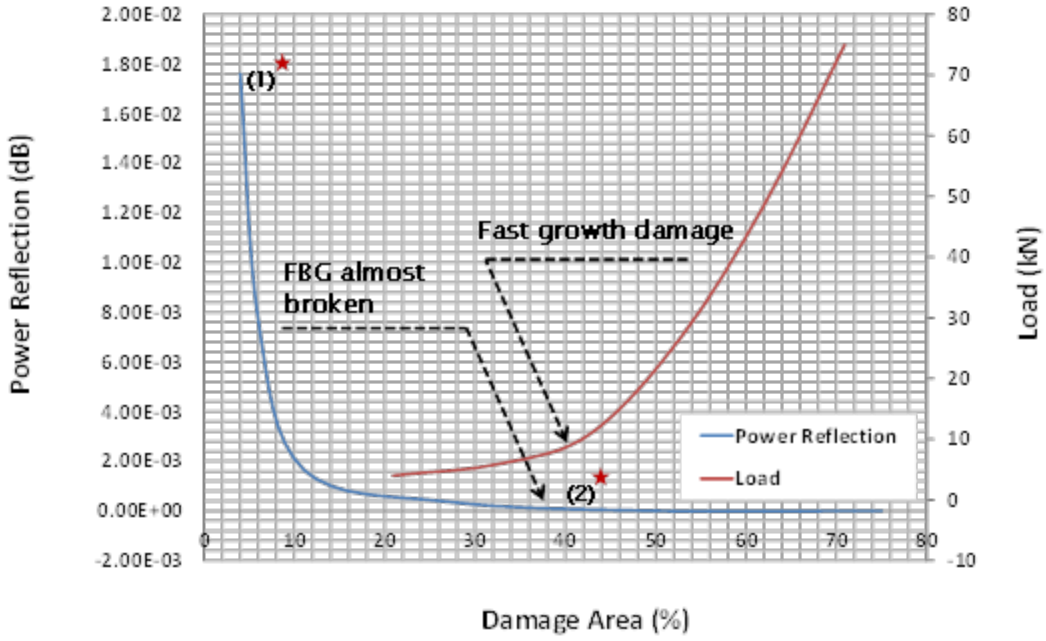

(a)

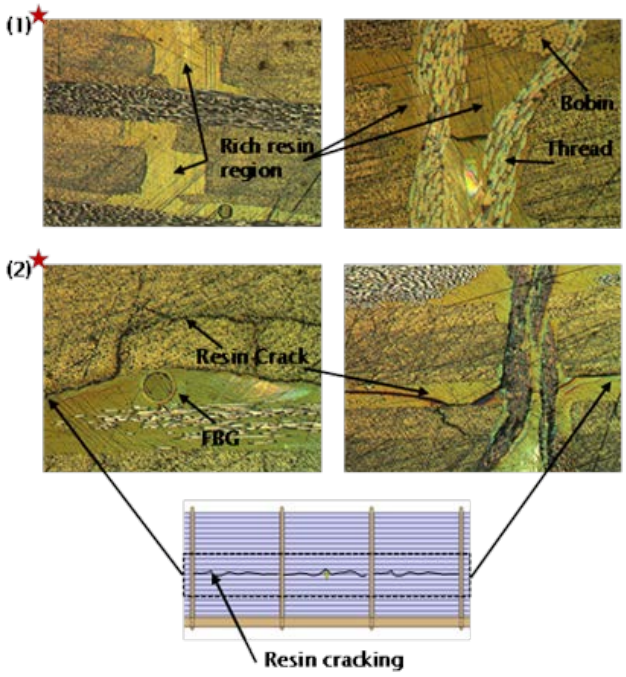

(b)

Figure 117 : (a) and (b) Damage quantification based on the FBG sensor reading and mechanical behavior.

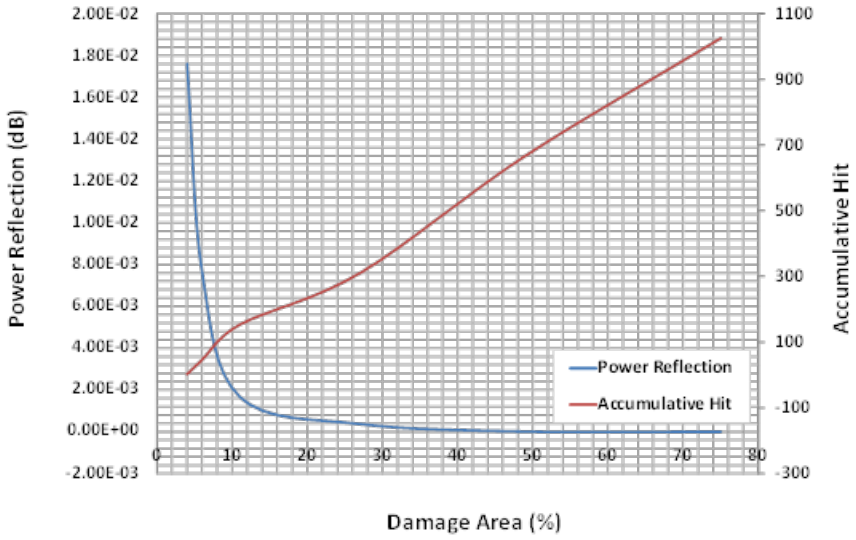

Figure 118 : Damage quantification based on the FBG sensor reading and AE characteristic.

3.7. Conclusions

The behavior of a stitched laminate material has been demonstrated by numerical and empirical approaches, using FBG sensors and enhancing with acoustic emission readings. The continuous monitoring of damage using FBG sensor has also demonstrated. Numerical and empirical approaches have become crucial to determine the proper placement of the FBG sensor. As a result, the behavior of the specimen and its tendency to create damage must be understood before the fabrication of the specimen in order to avoid misreadings.

We conclude that the FBG sensor can detect initial damage and its subsequent growth properly, as proven by empirical data. The occurrence of damage to the specimen can be characterized by the FBG sensor reading by the existence of multiple peaks in the power reflection. The damage growth can be successfully quantified by FBG sensor readings by knowing the decreasing trend of the highest peak during the occurrence of the multi-peak spectrum. It is also important to determine the coating material of the FBG sensor to avoid incompatibility with the resin used in the stitched laminate during fabrication. Additionally, acoustic emission readings can be used to detect and quantify the damage, but FBG sensor has the advantage in that its data involves only a single spectrum and is therefore simpler.

CHAPTER 4: CONCLUSIONS.

4.1. Conclusions

This research presented an analytical and an experimental study of FBG sensor for in-situ damage detection techniques as a basis for SHM. The main focus was placed on the spectrum behavior response of FBG sensor during loading induced to specimen which have evolved shape of the spectrum if damage happen. For the method, a thorough literature review was presented, followed by an analytical study to predict the mechanical behavior of the specimen to predict the potential damage onset, location and behavior. These studies were supported by finite element solutions for identical models using cohesive zone model and classical laminate theory with first ply failure for comparison. Finally, each specimen was tested experimentally using two types of loading, tensile and three-point bending. The strengths, weakness, and limitations of each loading case were explained and compared, and suggestions for implementation of these methods into a composite structural health monitoring system was given.

Using the spectrum evolution response methods as result FBG sensor reading, a results. The multi-peak occurring and wavelength broader significantly appear to be appropriate for detecting damage onset and growth in the specimen model. Spectrum evolution response has a potentially useful role in a SHM system, by guiding multi-peak occurring and wavelength broader as a result FBG sensor reading for a damage

indication and monitoring the global decay of structural stiffness degradation. Combined with C-scan inspection, the damage onset and growth can be quantified during conducted the test. The method and procedure used in this research were also validated successfully to demonstrate the feasibility of damage detecting and representative composite materials and structures. Combined joint in the case of a thin composite structure indicated spectrum evolution changes with multi-peak occurs rapidly if it compared with the bonded joint only under tensile loading. It proves bonded joint has damage resistant better than the combined join as shown graph spectrum in Fig.73 (a)(b). In contrast to the imposition of a three-point loading as shown in Fig.77(a)(b), looks combined joint has a damage resistant better than the bonded joint only. In addition to the bonded joint only under three-point loading did not occur multi-peak spectrum as an indication of damage happen. This showed in three-point loading, it just produces linear strains and the spectrum followed the Fresnel equation, while the only wavelength become broader during loading run. The interesting one, that FBG sensor's spectrum is unique in every case load. This is shown in all the spectrum results under FBG sensor reading in both cases; in a thin composite structure under tensile and three-point loading and in the stitched laminate under tensile loading. So it needed different techniques to interpret the spectrum occurs. Exploration of various

loading scenarios at various damage modes to be important in order to have a thorough understanding of the field of SHM using FBG sensor.

Using FBG sensor as damage detecting tools in the composite material have the widely potential to change the concept designs and maintenance of the aircraft because the FBG sensor provides structure integrity profile in real time during the operation of the structure and this method can provide more detail information since this technology can embed into a composite materials and structures and make a response of structural integrity. This potential increase after FBG sensor can prove its capability to detect global stiffness degradation as shown in stitched laminate damage detection result, then not required precise design planning before FBG sensor installation as the previous assumption that the effectiveness of FBG sensor to detect damage limited in the near of grating length.

Furthermore, this research describes each component integral to a SHM system. This includes the FBG sensor location analysis, data communication systems, spectrum shape interpretation, non-destruction inspection that binds them all together. A recommendation was provided for a feasible architecture for current implementation, and a prediction for the future of SHM systems is given. Structural health monitoring systems are likely to be an important component in future designs of composite air and spacecraft

to increase the feasibility of their missions and reduce their life-cycle costs, and in-situ non-destructive inspection will likely play a role in these systems.

4.2. Recommendations

Much work still remains before current SHM systems can be relied upon to replace standard inspection and maintenance cycles. More experiments should be performed on built-up and larger structures to confirm the initial results. An experiment study paralleling the performed tests but varying the sire of the damaged regions would also be useful in determining this method's sensitivity. For implementing FBG sensor technology to stitched laminate material, it is important to do more in stitches density to enrich the data, also possibility to use stitching technique for damage retardation, especially in near hole area. While for a thin structure with a mismatch stiffened due to loading case, important in further work to create combined loading case to represent the real condition in aircraft structures. It would also be interesting to perform more experiments using high density of FBG sensors to perform several types of tests, which should also be implemented on representative structures in future testing. Another possibility would be to test these methods on composite materials and structures in use such as in-situ repair, since the present work only included newly manufactured

specimens, and did not account for the complexities inherent to retrofitting a system to an aging structure.

There are also other useful methods that should be explored using similar procedures. This includes acoustic emission measurement, and several other electrical and magnetic impedance measurement methods. Another avenue of research could be pursuing all of the previously mentioned methods using new types of sensors, designed to be lightweight and conformable specifically for SHM applications. After good sensors and sensing systems have been developed, much work still remains on each of the other components of SHM systems. Testing the integration of these components will be an important part of a successful program. Most directly, remotely controlling and accessing data from sensors via wireless connection and power still needs much attention. There are many components that have yet to be suitably developed for SHM applications, however the aerospace community has a present understanding of the need for SHM systems, and they will be a reality in the near future.

REFERENCES

1. Chantal Fuades. 'Composite @Airbus Damage Tolerance Methodology'. FAA Workshop for Composite Damage Tolerance and maintenance, 2006.
2. Michael Mohaghegh. 'Validation and Certification of Aircraft Structure'. 46th AIAA/ASME/ASME/AHS/ASC Structures, Structural Dynamics and Material Conference, Texas, 2005.
3. DOT/FAA/AR-95/109. 'Comparative Evaluation of Failure Analysis Methods for Composite Laminates, 1996.
4. Hall S.R. and TJ. Conquest. 'The Total Data Integrity Initiative Structural Health Monitoring, The Next Generation'. Proceedings of the 2nd USAFASIP, 1999.
5. http://www.airweb.faa.gov/Regulatory.
6. MIL-HDBK-17. 'Composite Materials Handbook'. 2002
7. Khan MAU. 'Non-Destructive Testing Applications in Commercial Aircraft Maintenance'. Proceeding of 7th European Conference on NDE, 1999.
8. Schmidt H.J., Schmidt-Bradecker B. and G. Tober. 'Design of Modem Aircraft Structure and the Role of NDI'. Proceeding of the European Conference on Non-Destructive Testing, 1999.

9. Manfred Kreuzer. ‘Strain measurement with fiber Bragg grating sensor’. HBH, Damstadt, Germany.

10. Bhat. N. ‘Delamination Growth in Graphite/Epoxy Composite Laminates Under Tensile Load’. Massachusetts Institute of Technology, Cambridge, USA, 1993.

11. Arief Yudhanto, Naoyuki Watanabe, Yutaka Iwahori, Hikaru Hoshi. ‘Compression properties and damage mechanisms of stitched carbon/epoxy composites’. Journal of Composites Science and Technology, (86) 52-60, 2013.

12. Arief Yudhanto, Yutaka Iwahori, Naoyuki Watanabe, Hikaru Hoshi. ‘Open hole fatigue characteristics and damage growth of stitched plain weave carbon/epoxy laminates’. International Journal of Fatigue, (43) 12-22, 2012.

13. K.T.Tan, N.Watanabe, M.Sano,Y.Iwahori, H.Hoshi. ‘Interlaminar fracture toughness of Vectran-stitched composite-experimental and computational analysis’. Journal of Composite Material, doi:10.1177, 2010.

14. K.T.Tan, N.Watanabe, Y.Iwahori. ‘Effect of stitch density and stitch thread thickness on low-velocity impact damage of stitched composites’. Journal of Composite: Part A. doi:10.1016, 2010.

15. A. Yoshimura, S. Yashiro, T. Okabe, and N. Takeda. Characterization of tensile damage progress stitched CFRP laminates. Advanced Composite Material, 16(3):233-244, 2007.

16. A.P. Mouritz, K.H. Leong, I. Herszberg. 'A review of the effect of stitching on the in-plane mechanical properties of fibre-reinforced polymer composites'. Composites Part A: Applied Science and Manufacturing, Volume 28, Issue 12, Pages 979-991, 1997.

17. H.G.S.J. Thuis and E. Eton. 'The effect of stitching density and laminate lay-up on the mechanical properties of stitched carbon fabrics'. Technical Report CR96126L, Nationaal Lucht-en Ruimtevaartlaboratorium (NLR), The Netherlands, 1996.

18. Todd M.D., Johnson G.A., Althouse B.A. and ST. Vohra. 'Flexural Beam-Based Fiber Bragg Grating Accelerometers'. IEEE Photonics Technology, Volume 10, 1605-1607, 1998.

19. Chi-Young Ryu, Jung-Ryul Lee, Chun-Gon Kim, Chang-Sun Hong. 'Buckling behavior monitoring of a composite wing box using multiplexed and multi-channeled built-in fiber Bragg grating strain sensors'. Journal of NDT, Volume 41, Issue 7, Pages 534-54, 2008.

20. R Jones, S Galea. ‘Health monitoring of composite repairs and joints using optical fibres’. Journal of Composite Structures, Volume 58, Issue 3, Pages 397-403, 2002.

21. Chiu W.K., Galea S.C., Loss L.L. and N. Rajic. ‘Damage Detection in Bonded Repair using Piezoceramics’. Journal of Smart Materials and Structures, Volume 9, 466-475, 2000.

22. Gere JM, Timoshenko SP. ‘Mechanics of Materials’. Third SI Edition, Chapman & Hall, London, 1991.

23. Schijve J. ‘Secondary Bending Moment’. NLR 72036U, 1972.

24. A.A.Baker. ‘Bonded Repair of Aircraft Structures’. Martinus Nijhoff Publishers, 1988.

25. Hang-yin Ling, Kin-tak Lau, Li Cheng, Zhongqing Su. ‘Mode II Fracture Behaviour Monitoring for Composite Laminates Using Embedded Fibre Bragg Grating Sensor’. Journal of Composite Structures, 76: 88-93. 2006.

26. S.Takeda, Y.Aoki, T.Ishikawa, N.Takeda, H.Kikukawa. ‘Structural Health Monitoring of Composite Wing Structure During Durability Test’. Journal of Composite Structures, 79:133-139, 2007.

27. S.Yashiro, T.Okabe, N.Takeda.'Damage Identification in a Hole CFRP Laminate using a Chirped Fiber Bragg Grating Sensor'. Journal of Composite Materials, 67:286-295, 2007.

28. Jin-Hwe Kweon, Jae-Woo Jung, Tae-Hwan Kim, Jhi-Ho Choi, Dong-Hyuti Kim. 'Failure of carbon composite-to-aluminum joints combined mechanical fastening and adhesive bonding'. Journal of Composite Structures, 75:192-198, 2006.

29. Jeff W.H. Yap, Murray L. Scott, Rodney S. Thomson, Dieter Hachenberg. 'The analysis of skin-to-stiffener debonding in composite aerospace structures'. Journal of Composite Structures, 57: 425-435, 2002.

30. Camanho PP, Davila CG, de Moura MF. 'Numerical Simulation of Mixed-Mode Progressive Delamination Composite Materials'. Journal of Composite Materials, 16:1415-38, 2003.

31. Turon A, Camanho PP, Costa J, Davila CG. 'A Damage Model for the Simulation of Delamination in Advanced Composites under Variable-Mode Loading'. Journal of Mechanics of Materials, 38:1072-89, 2006.

32. A.G.Magalhaes, M.F.S.F.de Moura, J.P.M. Goncalves. 'Evaluation of stress concentration effects single-lap bonded joint of laminate composite materials'. Journal of Adhesion and Adhesive, 25:313-319, 2005.

33. Kollar L. and RJ. Steenkiste. ‘Calculation of the Stresses and Strains in Embedded Fiber Optic Sensors’. Journal of Composite Materials, 32:1647-1679, 1998.

34. Bocherens E, Bourasseau S., Dewynter-Marty V., Py S., Dupont M., Ferdinand P. and H. Berenger. ‘Damage Detection in a Radome Sandwich Material with Embedded Fiber Optic Sensors’. Journal of Smart Materials and Structures, Volume 9, 310-315, 2000.

35. Green AK., Zaidman M., Shafir E, and S. Gall. ‘Infrastructure Development for Incorporation Fibre-Optic Sensors in Composite Materials’. Journal of Smart Materials and Structures, Volume 9, 316- 321, 2000.

36. Steenkiste RJ., and L. Kollar. ‘Effect of Coating on the Stresses and Strains in an Embedded Fiber Optic Sensor’. Journal of Composite Materials, Volume 32, 1680-1711,1998.

37. Todoroki A,Tanaka Y, Y. Shimamura. ‘Response Surface for Delamination Monitoring of Gr/Ep Composites Using Electric Resistance Change’. Proceeding of the International Workshop on Structural Health Monitoring, 308-316, 1999.

38. Takeda S, Okabe Y, Yamamoto T, Takeda N. ‘Detection of Edge Delamination in CFRP Laminates under Cyclic Loading using Small-Diameter FBG Sensors’. Journal of Composite Science and Technology Journal, Volume 6,1885-94, 2003.

39. Yang Q, Cox BN. 'Cohesive Models for Damage Evolution in Laminated Composites. Journal of Fracture Mechanic, Volume 133, 107-137, 2005.

40. Reedy ED, Mello FJ, Guess TR. 'Modeling the Initiation and Growth of Delaminations in Composite Structures'. Journal of Composite Materials, Volume 31,812-31, 1997.

41. A.P. Mounts, K.H. Leong, and I. Herszberg. 'A review of the effect of stitching on the in-plane mechanical properties of fibre-reinforced polymer composites'. Journal of Composite Part A, 28A(12), 979-991, 1997.

42. Thomas Hahn, Jenn Min Yang, Sung Suh, Tan Yi and Guocai Wu. 'Damage Tolerance and Durability of Selectively Stitched Stiffened Panels'. DOT/FAA/AR-03/46, 2003.

43. Marantidis C, Van Way CB. and XK Kudva. 'Acoustic-Emission Sensing in an On-Board Smart Structural Health Monitoring System for Military Aircraft'. Proceeding of SPIE Conference on Smart Structures and Integrated Systems. 258-264,1994.

44. Wang H, Ogin SL, Thorne AM, Reed GT. 'Interaction Between Optical Fibre Sensors and Matrix Cracks in Cross-Ply GFRP Laminates. Part 2: Crack Detection'. Journal of Composite Science and Technology, Volume 66, 2367-78, 2006.

45. Meschke.G, Helnwein.P. 'Large-Strain 3D-Analysis of Fibre-Reinforced Composite using Rebar Elements: Hyperelastic Formulation for Cords'. Journal of Computational Mechanics, Volume 13, 241-254, 1994

46. Sprenger.W, Wagner.W. 'On the Formulation of Geometrically Nonlinear 3D-Rebar-Elements using the Enhanced Assumed Strain Method'. Journal of Engineering Structures, Volume 21:209-218, 1999.

47. Yashiro S, Takeda N, Okabe T, Sekine H. 'A New Approach to Predicting Multiple Damage States in Composite Laminates with FBG Sensors'. Journal of Composite Science and Technology, Volume 65, 659-667, 2005.

48. Botsis J, Humbert L, Colpo F, Giaccari P. 'Embedded Fiber Bragg Grating Sensor for Internal Strain Measurements in Polymeric Materials'. Journal of Optic and Lasers in Engineering, Volume 43, 491-510, 2005.

PUBLICATION LIST

Papers for International Journal Publisher;

1. Trilaksono A, Watanabe N, Hoshi H, Kondo A, Takeda S, Iwahori Y. Damage Monitoring in Composite Stiffened Skin using Fiber Bragg Grating under Tensile and Three-Point Loading; Mechanics Engineering & Automation Journal, Vol.3, No.4, 2013.
2. Trilaksono A, Watanabe N, Hoshi H, Kondo A, Takeda S, Iwahori Y. Continuous Damage Monitoring of A Thin Composite Structural with Mismatched Stiffener in a Combined Joint using Fiber Bragg Grating Under Tension and Three-Point Loading; Open Journal of Composite Materials, Vol.3, No.3, 2013
3. Trilaksono A, Watanabe N, Hoshi H, Kondo A, Takeda S, Iwahori Y. Investigation of the Mechanical Behavior of a Thin Composite Stiffened Skin with a Combined Joint; Mechanics Engineering & Automation Journal, Vol. 3, No. 7, 2013.
4. Trilaksono A, Watanabe N, Kondo A, Iwahori Y. Automatic Damage Detection and Monitoring of a Stitch Laminate System Using a Fiber Bragg Grating Strain Sensor. Accepted in Open International Journal of Composite Material.

Papers for International Conference;

1. Trilaksono A, Watanabe N, Hoshi H, Kondo A, Takeda S, Iwahori Y. Monitoring Secondary Bending Failure Under Tension Load Using Fiber Bragg Grating. CJJCC10 Conference, China, 2012
2. Trilaksono A, Watanabe N, Hoshi H, Kondo A, Takeda S, Iwahori Y. Damage Monitoring in Composite Stiffened Skin using Fiber Bragg Grating under Tensile Loading. JCCM-4 Conference,Tokyo 2013.